Physical evolution of the cement paste interface at fresh state and very early age

Typhanie Craipeau

THESE DE DOCTORAT

L'UNIVERSITE BRETAGNE SUD
COMUE UNIVERSITE BRETAGNE LOIRE

ECOLE DOCTORALE N° 602
Sciences pour l'Ingénieur
Spécialité : Génie civil

Par
Typhanie Craipeau

Evolution physique de l'interface de pâte cimentaire à l'état frais et au très jeune âge

Physical evolution of the cement paste interface in the fresh state and very early age

Thèse présentée et soutenue à Lorient le 13 février 2020
Unité de recherche : Institut de Recherche Dupuy de Lôme UMR CNRS 6027
Thèse N° : 554

Rapporteurs avant soutenance :

Nicolas Roussel — Directeur de Recherche - IFSTTAR
Juliette Cayer-Barrioz — Directrice de recherche - CNRS/LTDS

Composition du Jury :

Examinateurs :
Martin Cyr — Professeur des universités - Université de Toulouse/LMDC/INSA Toulouse
Kjell Tore Fossä — Researcher - University of Stavanger/Kvaerne

Dir. de thèse : Arnaud Perrot — Maître de conférence - Université Bretagne Sud
Co-dir. de thèse : Thibaut Lecompte — Maître de conférence - Université Bretagne Sud

Invité(s)
Fabrice Toussaint — Ingénieur de Recherche - LafargeHolcim Innovation center

Titre : **Evolution physique de l'interface pâte cimentaire à l'état frais et au très jeune âge**

Mots clés : matériaux à base cimentaire, interface, adhésion, friction, rhéologie, coffrages glissants

Résumé : Le béton est un matériau dont la microstructure évolue rapidement, dans les heures suivant sa fabrication. De même les propriétés physiques et chimiques à l'interface avec un support évoluent avec des conséquences très importantes, en particulier si cette interface est sollicitée. Par exemple, dans le procédé industriel des coffrages glissants, l'interface béton/coffrage remonte graduellement à l'aide de vérins au fur et à mesure de l'hydratation du béton. Les hydrates, en se formant modifient la microstructure de la matrice cimentaire. L'eau induit une dépression à partir de l'instant de percolation solide, et par réaction un effet de succion. Selon le principe de Terzaghi valable pour ce milieu saturé, des contraintes granulaires sont alors transmises à la paroi. En considérant le principe des voutes de Janssen, et en prenant en compte la contrainte seuil du béton à l'interface, puis un coefficient de friction, il devient possible d'évaluer la force globale transmise à une plaque.

Des dispositifs expérimentaux, accompagnés d'une démarche de modélisation, ont été mis au point et utilisés avec une approche partant de la chimie, passant par la physique, et allant vers la mécanique. L'hydratation du système a été explorée. Ses conséquences sur les variations volumiques et la dépression qui s'ensuit au cœur du matériau et à l'interface ont également été calculées et mesurées. Enfin, au travers d'une approche combinant la compressibilité du matériau et de son système environnant, les conséquences de la dépression sur la contrainte à l'interface ont été évaluées par la mise au point d'un essai spécifique. Un dispositif expérimental global consistant en une plaque mobile durant toute la phase d'évolution du béton plus représentatif du procédé industriel a été conçu, puis fabriqué. Des mesures ont été réalisées sur un mortier représentatif du béton, en faisant varier les paramètres matériau clé, telle que la quantité d'air, la fraction volumique solide, l'empilement granulaire ou encore la tension de surface du liquide interstitiel. Les travaux de thèse ont permis d'améliorer la compréhension des phénomènes à l'interface.

Title: Physical evolution of the cement paste interface in the fresh state and very early age

Keywords : cement-based material, interface, adhesion, friction, rheology, slipforming

Abstract: Concrete is a material which microstructure evolves fast after its mixing. Also, physical and chemical properties at the interface with a support evolve with important consequences, in particular if this interface is solicited. For example, in the industrial process of slipforming, the interface concrete/formwork is lifted gradually with jacks during concrete hydration. Microstructure of hydrates changes during their formation in the cement matrix. Water induces a negative pressure after solid percolation, and thus suction effect. According to Terzaghi's principle -applicable for saturated materials- granular stresses are transferred to the surface. Considering Janssen vaults and taking into account yield stress of the concrete at the interface and then friction coefficient, it is possible to evaluate the global strength applied to a wall.

Experimental devices, with a modeling approach, was developed and used with an approach from chemistry, through physics to mechanics. Hydration of the material was explored. Its consequences on volume variations and negative pressure in the bulk material and at the interface were calculated and mesured.

In the end, through an approach including material compressibility and its surrounding system, consequences of the negative pressure at the interface was evaluated by developping a specific device. The global experimental device is composed of a mobile plate studied during the representive phase of the industrial process. Measurements were carried out on a representative mortar of the concrete by varying influent key parameters as air quantity, solid volume fraction, granular packing and interfacial liquid surface tension.

This PhD research work allows to improve the understanding of the phenomena at the interface.

Avant propos

Les travaux de recherche de ce manuscrit n'auraient pu exister sans le soutien de vous tous. Au travers de ces mots, je vous exprime toute ma reconnaissance.

En premier lieu, je tiens à remercier mes trois encadrants qui ont été exceptionnels et complémentaires. Je suis persuadée que l'encadrement d'une thèse est le plus important. Un grand merci à Fabrice qui, après m'avoir fait découvrir les matériaux cimentaires, a su m'encourager tout le long de ces 3 années de thèse. J'ai appris à évaluer les concepts de manière globale (les ordres de grandeur !!) et je suis admirative de sa méthodologie (« repartir d'une feuille blanche, « mettre tout à plat pour avoir les idée claires »). Arnaud, je te suis très reconnaissante pour ton encouragement perpétuel, pour ta disponibilité de tout instant (y compris le 24 décembre !). Merci Thibaut pour tes réflexions de physique de fond, les idées dispositifs (on n'oublie pas Tonton Thibaut pour les croquis). Merci à tous les trois pour votre bienveillance et votre humour, qui sont essentiels. Malgré la distance, nous avons réussi à réunir notre petit groupe de recherche que nous formions tous les trois mois en présentiel. A chaque fois ces réunions ont été un réel plaisir et source de motivation pour la prochaine. Par exemple, c'est lors de nos séances brainstorming que sont nés la boite magique et le capteur de friction (nous ne l'avons pas acheté 50 000€ mais construit). Vu l'étendue du sujet, j'ai donc appris à prioriser. C'est grâce à vos qualités humaines que vous avez su me transmettre votre passion pour la recherche.
J'insiste sur le travail remarquable de Yohan sans lequel il n'aurait pas été possible de faire parler cette boite magique ! C'est grâce à sa rigueur et à sa grande capacité de travail que nous avons pu obtenir les résultats du chapitre 3.
Merci à Bruno pour la collaboration pour le modèle Thermodynamique. Ces échanges ont beaucoup apporté à notre réflexion sur la modélisation de la pression interstitielle.
Une thèse c'est aussi des collaborations externes. Je remercie le Professeur Peter McDonald et Agata Gagewicz avec qui j'ai effectué les mesures de relaxometrie RMN dans leur laboratoire à l'Université de Surrey. Les mesures de compressibilité à l'INSA Rennes avec Damien Rangeard et Yohan Jacquet ont été très formatrices. Je remercie Sandra Boivin pour son regard sur l'orientation de la thèse, ses venues au laboratoire ; ainsi que de m'avoir permis d'assister à une semaine de formation sur la microstructuration avec des professeurs de haute renommée. Merci également à Arnaud De Laplace pour les discussions d'équilibre des forces dans le système. J'ai apprécié présenter lors de congrès internationaux (même si avoir l'autorisation d'y aller n'a pas toujours été facile), ce sont des lieux d'échanges qui sont source de motivation.
J'ai beaucoup apprécié donner des cours au sein de l'école Polytech, ça a été un réel plaisir de faire découvrir la magie des matériaux cimentaires. Merci à Thibaut de m'y avoir poussée.
Tous mes remerciements à l'ensemble des personnes du Centre d'Innovation LafargeHolcim pour leur grande sympathie ainsi que leur disponibilité permanente. Un merci particulier à Vincent qui était toujours là avec de bons conseils, toujours motivé pour que les résultats arrivent plus vite. Je repense aussi à nos interrogations devant le dispositif de cisaillement vertical (le fameux DCV ;)) et surtout pour la mesure de la pression interstitielle à l'interface. Benoit, tu es un exemple en terme d'optimisation du rapport efficacité / temps ainsi que sur excel. Merci Jean-Nicolas de m'avoir intégrée au projet des coffrages glissants et pour nos nombreuses discussions sur le DCV. Je remercie également Cédric Juge pour son aide, particulièrement pour le montage des capteurs.
Merci à Alexandre Menguy pour sa maitrise de Solid Works. Ce sont des interactions de tous les jours qui m'ont marquée et ont rendu les journées de labo parfois longues plus agréables : je pense aux apparitions de Manu Bonnet dans le labo, nos discussions et questionnements. Je pense aussi aux échanges « bricolage » avec Adrien qui m'a toujours accueillie avec le sourire pour des conseils ou du prêt de matériel, l'idée du presse étoupe pour le capteur de pression et tant d'autres ! Je repense également aux réflexions sur le choix des capteurs et de l'enregistrement avec Hervé Noyallé et les débats sur l'hydratation avec Serge et Alain. Merci aussi à Cédric Jaillet pour son aide efficace pour des manip en plein mois d'août ! Un grand merci à Sylvain qui m'a toujours « dépatouillée », pour les bons souvenirs du démontage de l'Air Void Analyser (même si nous n'avons pas réussi à le

réparer…). Merci à David pour les conseils de présentation. Merci à Gérard pour son œil design pour les Power Point et pour Jupiter. Merci également à Aziz, avec qui nous avons continué d'interagir même si nous n'étions plus sur le même projet. Merci aussi à Alex pour ses relectures et conseils en anglais. Je n'oublie pas Denis, avec qui il a été très agréable de partager le bureau et nos sessions tests de chocolats ainsi que les nombreux débogages sur python.
Une pensée sympathique pour la team-midi : Serge, Corinne, Florent, David, Fabrice, Le Chien pour tous ces midis à la super cantine de LCR (devrais-je dire LHIC…).
Et du coté Lorient, je remercie les différents doctorants Mathilde, Théo, Florent avec qui nous avons partagé les Doctoriales ainsi que le congrès de Strasbourg ; François Porthanguen, pour l'usinage du DCV ; Hervé, le génie à 1000 à l'heure sur 1000 projets et Alix pour les footings sur la plage et l'Avifit avec Antoine.
Cette thèse Cifre m'a permis d'appréhender le monde académique et industriel avec chacun ses avantages et inconvénients. J'ai également pu faire la visite de chantier et d'usine de ciment, ce que j'ai trouvé très intéressant.
Un mot pour « les sportifs pro ;) », pour les footings du midi et les allers-retours en vélo : « 7h grange blanche » avec JN et David ; et une dédicace à notre trajet d'un matin sous une presque tempête David !
Un petit paragraphe spécial pour les amis qui assurent un équilibre pendant une thèse, je pense à mes amis rameurs d'enfance et tous mes amis de CPE lyonnais et non lyonnais ;). Je remercie mon coloc Flo, pour ses gâteaux le matin, les repas, la construction de lampes et les trajets en vélo…vive le triathlon !
Mes derniers remerciements vont à mes parents et mes deux frères Christopher et Gauthier pour leur soutien dans mes projets et également Brigitte, Jean-Paul, Fanny et Camille pour tous ces bons moments partagés. Yoann, je ne te remercierai jamais assez pour ton soutien continu, ta patience et ton partage de motivation pour les sciences.
Pour moi la thèse a été comme un château de cartes, où chaque carte est importante, j'ai pu bétonner cet édifice et l'assembler grâce à vous.

Table of content

Nomenclature

Abbreviations

AS	Autogenous shrinkage
ASTM	American society of testing and material
AVA	Air void analyzer
CH, $Ca(OH)^2$	Portandite
CaO	Lime
CS	Chemical shrinkage
C-S-H	Calcium silicate hydrate
C_3S	Alite
C_2S	Belite
CEM I	Portland cement
DSC	Differential scanning calorimetry
DTA	Differential thermal analysis
EXP	Experimental method
HS	Hindered shrinkage
MRI	Magnetic resonance imaging
MIP	Mercury intrusion porosimetry
NMR	Nuclear magnetic resonance
PCE	Polycarboxylate polymers
PSD	Pore size distribution
RGB	Red green blue model
SEM	Scanning electron microscope
T_0	Instant when the cement is in contact with water.
THERM	Thermodynamic method
TGA	Thermogravimetric analysis
W/C	Water over cement mass ratio

Physical quantities

D10, D50, D90	Pore size distribution diameter: 10%, 50% and 90% of the cumulative mass
E	Young modulus
e	Void coefficient
F	Strength
F_{uw}	Pore water strength
F_N	Normal strength
$F_{\sigma'}$	Effective strength
F_{mt}	strength of material at the top
F_{mb}	strength of material at the bottom
F_{jt}	strength of the joints at the top
F_{jb}	strength of the joints at the bottom
G	Conductance
K_s	Solubility coefficient
M_i	torque
P_g	Gas pressure
P_l	Liquid pressure
Ra	Roughness index
S	Saturation
s	Suction (difference between water pressure and air pressure)
u_w	Pore water pressure
w	Membrane bending displacement

α	Degree of hydration
γ	Surface tension
$\dot{\gamma}$	Shear rate
ΔrH	Enthalpy of reaction
μ	Friction coefficient
μ_p	Plastic viscosity
ξ	Participation rate
η	viscosity
θ	angle
σ	Total normal stress
σ'	Effective stress
σ_c	Conductivity of the solution
τ	Yield stress
τ_0	Bulk yield stress
τ_{w0}	Interfacial yield stress
υ	Poisson coefficient

Introduction

Concrete is like a “liquid stone” which can be shaped as desired. Depending of its rheological properties, it can be shaped using dedicated and adapted processes. Some concretes flow under their own weight, whereas others need a lot of energy in order to be deformed using compaction. When considering vertical structures and fluid concrete, it is necessary to place the concrete in a formwork and to wait until it is hardened before demolding. This is the most traditional way of shaping concrete.

Nevertheless, some other possibilities can be noticed. Depending on the configuration, shotcrete can be an alternative for example. The concrete is shot under pressure and is compacted by its kinetic energy, ensuring a good adhesion to the surface. However, the thickness is limited to several centimeters with this technique and a support is necessary. Extrusion (or semi-extrusion) is another technique which can be used to shape concrete. It is often used for small height and rather long distance geometries like for borders or edges, or for precast beam elements. When considering high elevation structures, new alternatives as additive manufacturing methods named also 3D printing techniques are very promising because they provide an unprecedented liberty of shapes and make it possible to dispense with the formworks. On the mid-term, this new technology seems to be limited to rather small structures made in precast factory, excluding onsite building largescale structures. Several applications are presented in *Figure 1*.

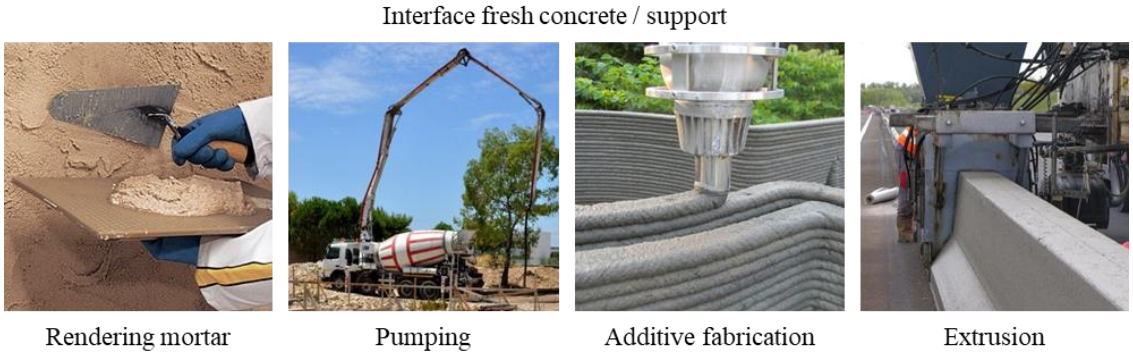

Figure 1. Illustration of different processes where fresh concrete interface plays an important role: rendering mortar, pumping, additive fabrication, extrusion.

Since some decades, another technique is used and can be considered as “2D printing”. This technique, called slipforming consists in using a transitory mold which is quasi-continuously moving vertically. Concrete is poured at the top of a low elevation mold which moves with hydraulic jacks. A few hours after entering the mold, the concrete begins to set and leaves the bottom of the mold, recovering the contact of the air. Very large infrastructure pieces are built with this technique. Recently, a 3D slipform technique was designed by using a flexible formwork: “Smart Dynamic Casting” [1] which is a 3D digital evolution of the slipforming process (see *Figure 2)*.

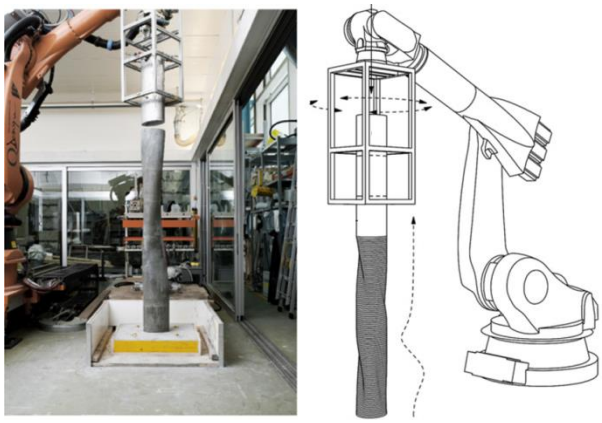

Figure 2. Illustration of Smart Dynamic Casting: 3D digital evolution of the slipforming process (adapted from [1]).

In all the above-mentioned processes, interface of concrete with a support has to be considered. When using a formwork, demolding oil is usually used in order to remove the formwork, so that hydrates do not stick to the surface. For shotcrete applications, at the contrary, adhesion must be sufficient in order to avoid any concrete drop. Rendering mortars requires also similar sticking properties. Masons appreciate a product because it does not stick to the tool they are using, but sticks to the support surface. During pumping or extrusion, the shear stress at the wall must be decreased in order to reduce the pressure necessary to process the material. A lubrication layer is naturally formed since the concrete is well designed. It allows to limit the pressure in the pipe. Mechanisms occurring during pumping are well described and the pressure can be well estimated with the tribology and rheology measurements [2] [3]. The question of adhesion can be also considered between different layers of concrete. In the 3D printing process, the adhesion between layers may be an issue as cold joints should weaken the final structure during its service life.

The most complex interfacial system is probably the one occurring during the slipform process as the concrete evolves continuously during the process. Slipforming process remains less described because it involves concrete in heterogeneous states: i.e. different maturation ages on the height of the moving formwork. Concrete behavior changes drastically from liquid to quasi-solid state. This technique, see Figure 2, is a widely used construction methodology for high rise linear structures such as skyscrapers, pylons, silos or marine foundations that benefit from its high construction speed and the absence of cold joint that may affect the durability of the structure. Usually, the formwork is about 1.2 meters high and the concrete has to be set when the bottom of the formwork releases the material. The average speed is around 15 to 25 centimeters per hour. The concrete is directly in contact with the formwork from its fresh state to a set state without any demolding oil. During sliding, possible micro-cracks/lumps formation can happen on the wall surface (*Figure 4*). These defects are most probably related to the concrete adhesion on the formwork [4]. These issues should be reduced and prevented to avoid a reduction of the durability of the structures that could turn into strong damages if not properly treated.

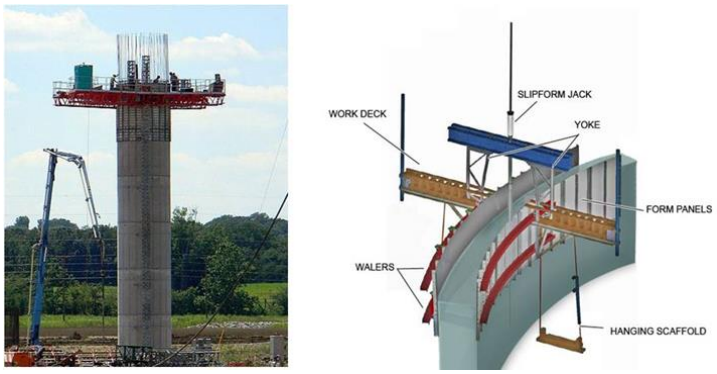

Figure 3. On the left picture of a construction of a pillar with the slipforming process. On the right, scheme of the slipforming equipment.

The understanding of the physic-chemical properties at the interface fresh concrete/moving formwork is thus crucial. Concerning friction, at the top of the formwork, a lubrication sheared layer forms (as observed during concrete pumping) while Coulumb friction occurs at the bottom of the formwork (*Figure 4*). Fosså [4] showed that the hardening concrete induces the highest friction stress in the intermediate layers at the middle of the formwork (*Figure 4*). This can be explained by the friction change along the formwork because of cement hydration. Concrete microstructure evolves after contact between cement and water and before setting time [5]. This physico-chemistry evolution induces heat release, mechanical stiffening of the material with small volume reduction (autogenous shrinkage) [6] [7].

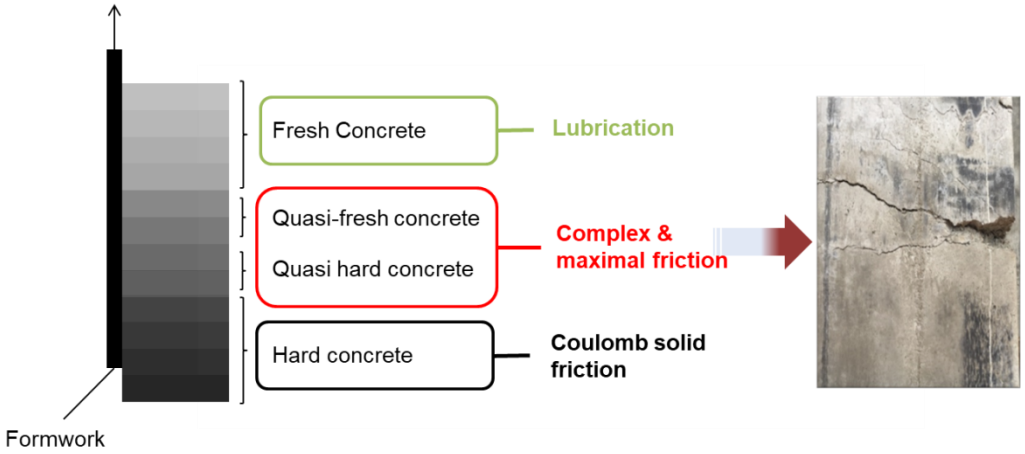

Figure 4. On the left, illustration of the different states of concrete in contact with a moving formwork. On the right: picture of surface damage due to concrete adhesion during the intermediate stage.

Hydrate formation induces microstructure variation and continuous water consumption. This creates major changes on the mechanical behavior of the interface (adherence, suction, shear stress/ friction) and thus on concrete placing and formwork slippage. It has been shown that shear stress of the concrete on the formwork increases with time after pouring. This increase of shear stress at the wall decreases the apparent weight of the concrete at the bottom of the form, and the lateral pressure exerted by self-compacting concrete on the formwork as well [8], [9], [10].

Evolution of this stress has been related to shear yield stress evolution mostly due to nucleation of cement grains during the dormant period (before setting time, thus in the 3 or 4 first hours after wetting time) [5], [11].

The increase of friction, especially in the zone where the concrete setting occurs, is also related to a suction phenomenon which is induced by volume change and water consumption that creates negative pore pressure. This suction can increase the normal granular stress acting on the formwork [12] [13] [14] and can explain surface damages on the concrete. Later, when the degree of hydration becomes higher (which corresponds to the layers at the bottom which are older), there will be a continuity of the air network, thus inducing a release of the suction.

Concerning the slipforming process, part of the surface damages is attributed to the process itself (time between lifting, net speed of lifting, and displacement distance of the formwork or average speed) and on the other side, the material composition. In this PhD thesis, the study focuses on the interface evolution at the material scale. It means that a special care is given to mix-design parameters and involved physical phenomena.

The aim of this study is to improve our knowledge of the physical phenomena which govern friction and adhesion between fresh concrete and a metallic formwork. Moreover, hydrates formation is expected to create a physical bond to the surface. In order to appreciate the overall behavior, when it is possible, the contribution of each phenomenon is evaluated separately. The objective of this research work is to link microstructure of the concrete (and mix-design) with overall mechanical stress and deformation at the interface between cementitious materials and steel interface. This would allow improving the mix-design of concrete dedicated to slipforming process or the interface design itself.
This industrial PhD is a collaboration between the Université de Bretagne Sud, Institut de Recherche Dupuy de Lôme in Lorient and LafargeHolcim Innovation Center in Lyon.

The manuscript is composed of a first section which focuses on hydrates formation during cement hydration using different characterization methods. This step is crucial as the origin of all observed phenomena are linked to cement chemical activity, i.e. hydrates formation, structural build-up and water consumption. The consequences of hydrates bounding to the surface are here studied. Chapter 2 consists of the description and modeling of the suction based on the measurement of hindered shrinkage that is at the origin of negative pore water pressure. In the third chapter, pore water pressure is controlled and its effect on bulk and interfacial shear stress is assessed on an inert and dense mineral suspension in order to isolate the suction effect on rheological and tribological behavior. In the end, the mechanical effect of all phenomena is observed on a specific new device developed to study the interface of fresh concrete with a moving formwork in order to identify the key mix-design parameters to reduce friction. The main points which affect the stress in the moving formwork are considered and a modeling approach of this system is carried out. Figure 4 sums up the content of this manuscript.

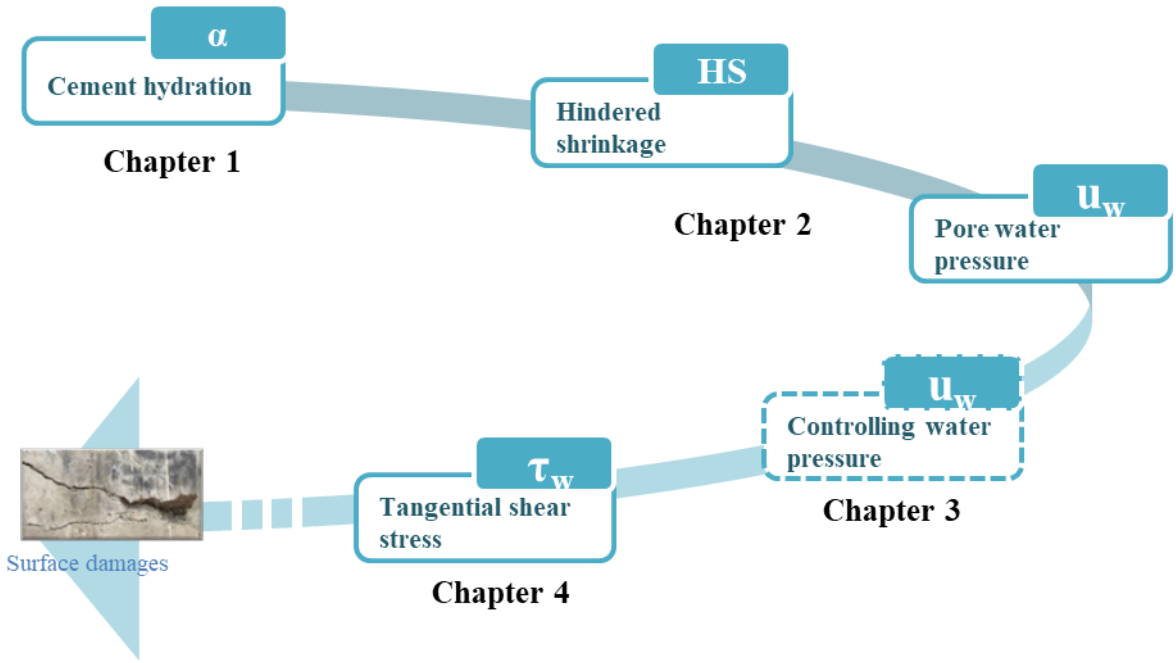

Figure 5. Organisation of the PhD thesis manuscript from chapter 1 to chapter 4.

Chapter 1: Hydrates identification (type and formation time) and adhesion consequences of the reference mix-design

1. Introduction

The following chapter focuses on cement hydration in order to characterize and identify the kinetics of hydrates formation that could bound to the formwork surface and thus could increase the concrete adhesion. Water consumption and volume balance leading to concrete structural build-up and water suction will be discussed in the other chapters.

Thereby, results of multiple approaches are presented in order to characterize the hydration of the chosen cement. It is important to keep in mind that all the analyses are not exactly performed in the same conditions: environment, sample size and nature (mortar or paste), with measurements performed on running or stopped reaction -depending on the device used for the analysis.

This chapter is composed of a first part dealing with the theory of hydration, then the description of the methods to identify hydrates formation is provided. In the following, results of the tests are presented and the reference mix-design hydration is described in details. In the last part, the mechanical consequences of hydration are presented and hydrates physical bounding to the surface is characterized using different steel supports.

2. Theory of hydration

2.1 Cement grain composition and process

Clinker is obtained by heating calcite ($CaCO_3$, around 80%) and clay (SiO_2, AlO_3, Fe_20_3, around 20%) in a precalcinator and a kiln. The different phases obtained during this process can be seen in *Figure 6*. Gypsum is added to the clinker to obtain the ordinary Portland cement. Cement is a complex material; it is not possible to obtain exactly two same cements with different batches. In cement plants, the cement producers have to adjust the quantity of phases in order to guarantee expected mechanical performances of the standardized cement.

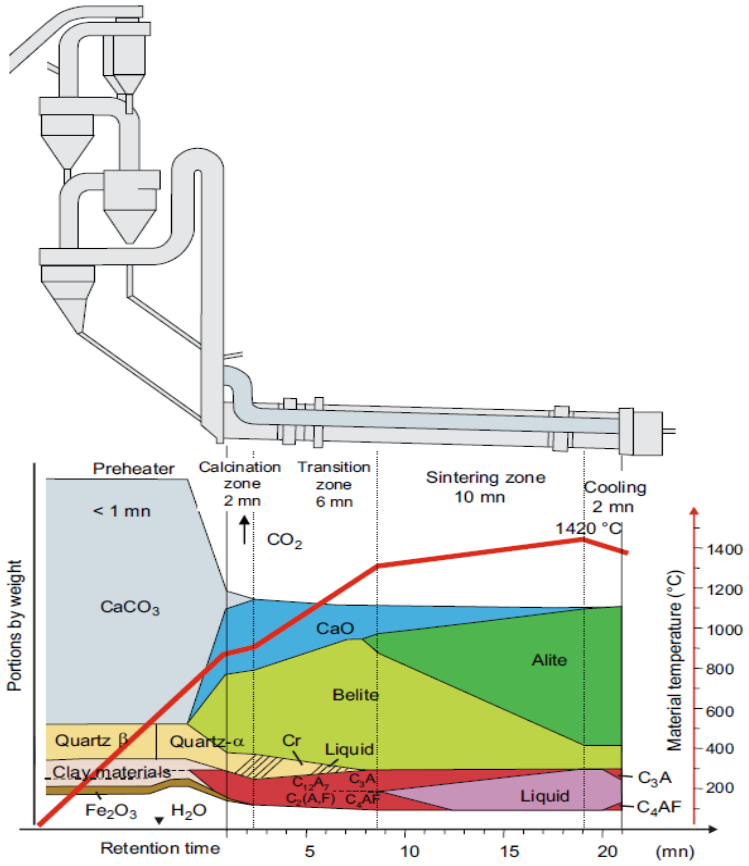

Figure 6. Formation of clinker in a short kiln equipped with a precalcinator. Evolution weight portions of the anhydre phases as a function of the retention time in the kiln [15].

The first step of this process - occurring at 950°C - is the decarbonation of the calcite $CaCO_3$, giving lime CaO and carbon dioxide CO_2, this represents 60% of the carbon emission of the process. One ton of raw extracted material created 580 tons of CO_2 in order to obtain clinker. Overall, the cement production represents 6% of the total $C0_2$ anthrogenic emissions in the world.

The heterogeneity of cement grain is represented in *Figure 7*, it is crucial to keep in mind that one grain of cement is composed of different phases which are not independent, this creates the complexity of cement. To illustrate this concept, the hydration of synthetized phases and "recreated" cement will not give the same hydration products than the natural cement. This is the magic of the cement specific chemical behavior!

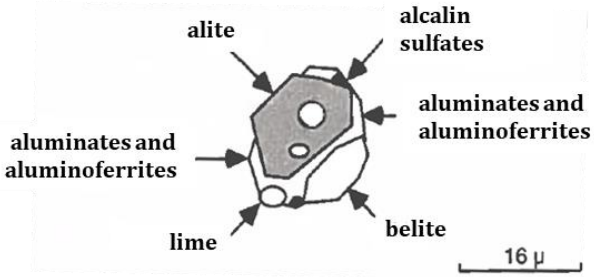

Figure 7. Scheme of cement grain highlighting the different anhydrous phases [16].

2.2 Hydration reaction

Hydration reactions from the most reactive hydrate to the less one are presented below:

$3CaO.Al_2O_3$ (C_3A)+ $3CaSO_4.2H_2O + H_2O \rightarrow C_3A.3CaSO_4.32H_2O$ (ettringite)

$3CaO.SiO_2$ (C_3S alite) +5.3 $H_2O \rightarrow C_{1.7}SH_4$ (C-S-H) + 1.3 $Ca(OH)_2$ (Portlandite CH)

$2CaO.SiO_2$ (C_2S belite) + 5.3 $H_2O \rightarrow C_{1.7}SH_4$ (C-S-H) + 0.3 $Ca(OH)_2$(Portlandite CH)

4 $CaO.Al_2O_3$ Fe_2O_3 (C_4AF) reaction (with gypsum $CaSO_4$) is less reactive.

Reminder: for the cement nomenclature

C: CaO ; S: SiO_2 ; F: Fe_2O_3 ; A: Al_2O_3 ; H: H_2O

Figure 8 illustrates the chemical reaction on C_3S phase. This is a simplification because, once again a grain of cement is composed of the different anhydrous phases and consequently different hydrates.

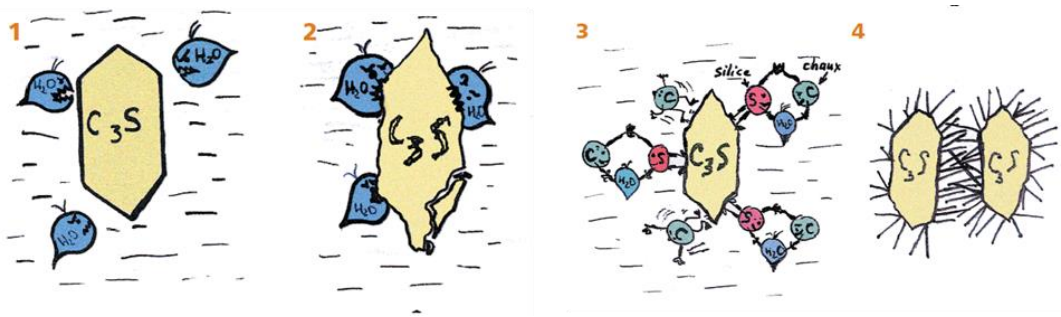

Figure 8. Illustration of hydration reaction between C_3S and water from one anhydrous phase of C_3S to growing hydrates [17].

Moreover, to complete the complexity of hydration, the surface of the anhydrous is hydrated selectively, *Figure 9* illustrates the preferential surfaces that are hydrated depending on the kinetics of hydration. Ettringite forms long needles, Portandite is dense particles and C-S-H is more cotton like structure. Hydration creates a densification of the system that leads to setting point (mechanical setting).

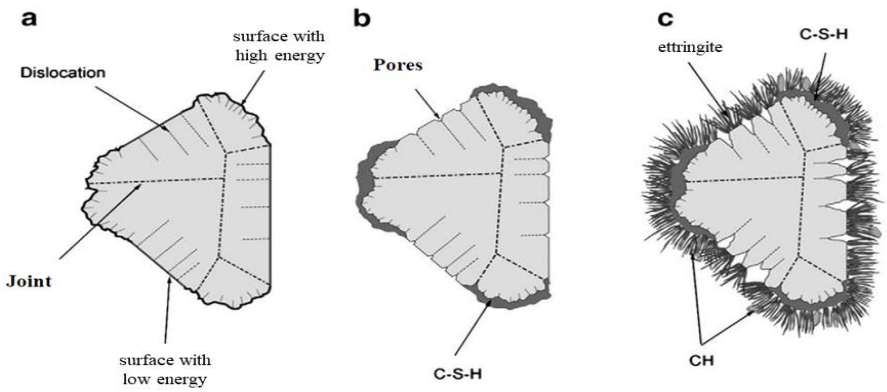

Figure 9. Illustration of the hydrates development around the anhydrous cement grain [adapted from [18]].

Volume variations associated to cement hydration are not discussed here but in *Chapter 2.*

2.3 Hydrates formation mechanisms

The hydration of CEM I cement is based on different mechanisms, which occur quasi simultaneously. The main mechanisms are:

- dissolution of the species,
- formation of a saturated solution,
- hydrates precipitation.

These phenomena are represented on *Figure 10* , adapted from [19].

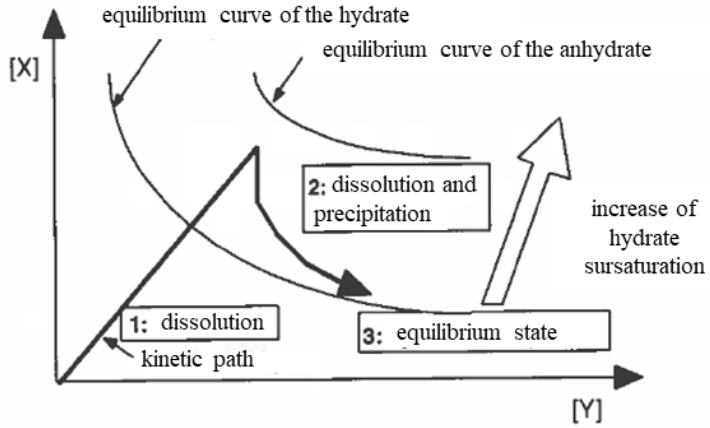

Figure 10. Illustration of dissolution and precipitation phenomenon: evolution of X species concentration as a function of Y species concentration [19].

Cement hydration is exothermic. Hydration reaction is the combination of anhydrous phases dissolution and hydrates formation. Both these reactions are exothermic but dissolution reactions are more exothermic than hydrates formation. The enthalpies of hydrates formation are:
$\Delta_{rC3A}H$= -431KJ.mol^{-1} of C_3A ; $\Delta_{rC3S}H$= -115KJ.mol^{-1} of C_3S; $\Delta_{rC2S}H$= -45KJ.mol^{-1} of C_2S

When the ionic concentrations are high enough so that the solubility coefficient (K_s) of the hydrates is reached, a germination process begins.
The precipitation speed of the hydrates depends on the solubility of those hydrates.
The dissolution of the lime is described below:

$$CaO_{(s)} + H_2O_{(l)} \rightleftarrows Ca^{2+}_{(aq)} + 2OH^-_{(aq)}$$

$$Ca^{2+}_{(aq)} + 2OH^-_{(aq)} \rightleftarrows Ca(OH)_{2(s)} \text{Ks=8.0 } 10^{-6}$$

Thus, :

$$CaO_{(s)} + H_2O_{(l)} \rightleftarrows Ca(OH)_{2(s)}$$

Then, ettringite transforms in monosulfate aluminate of hydrated calcium as:
$C_3A + H_2O \rightarrow C_3A.CaSO_4.14H_2O$ (monosulfoaluminate of calcium hydrate)

Concentration gradients and the first layers of the hydrates around the anhydrous substances play a major role on the reaction kinetics dissolution [20]. It can be illustrated comparing the hydration of different size of anhydrates (see *Figure 11* adapted from Boivin [19]).

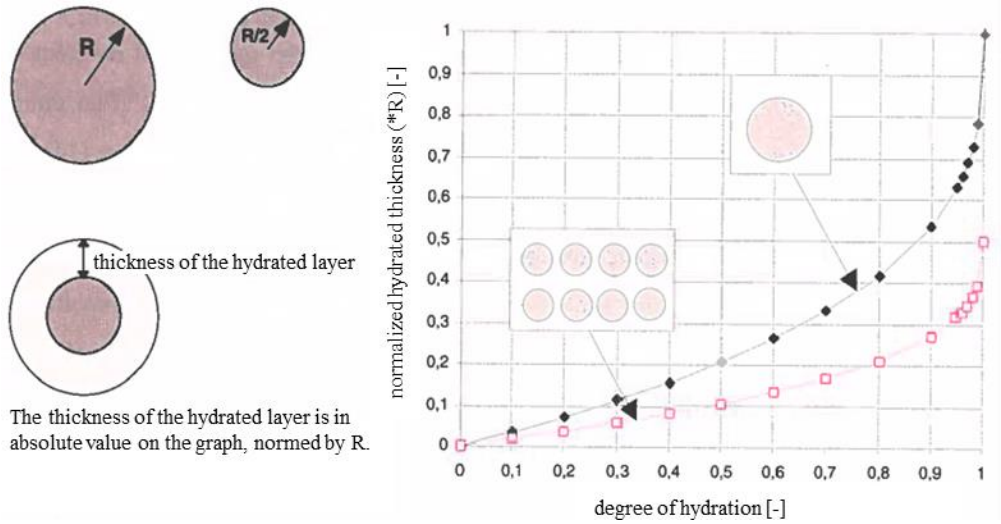

Figure 11. Illustration of the characteristic relation size / hydration: evolution of the normalized thickness of the hydrated layer as a function of degree of hydration for two size particle respectively of R radius and R/2 [19].

2.4 Heat released associated to cement hydration

Hydration reactions are exothermic, *Figure 12* is a summary of the main stages of hydration, it starts with the dissolution peak, then the dormant period where there is no apparent or reversible change in rheology but hydration is continuing. Then, there is an acceleration of kinetics, followed by a deceleration (stages 4 and 5). The durations of these different stages depend on the cement and mix-design of the cementitious material. The different stages with the chosen cement for this work are detailed, analysing the conductivity curve in *section 4.1* of the present chapter.

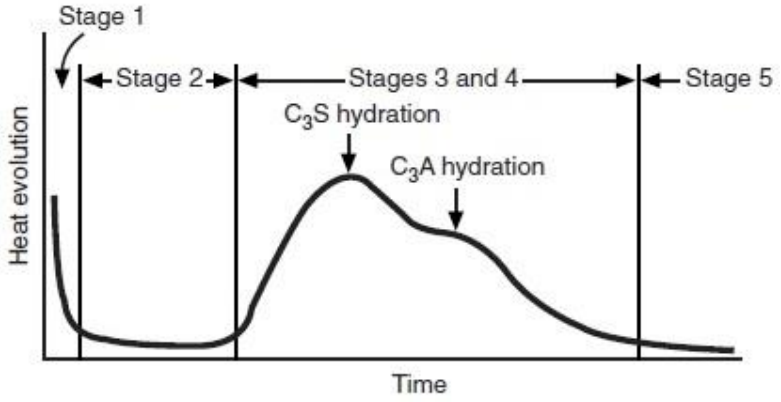

Figure 12. Heat evolution as a function of time. Stage 1 is the wetting heat. Stage 2 is the dormant period. Stage 3 is an acceleration of the hydration reactions. In stage 4 there is a deceleration of hydration and stage 5 is the slow hydration [20].

3. Materials

Concrete is the reference material but in this work and for practical reasons, the experiments are carried out at the mortar scale in order to find the best compromise between concrete representativeness and lab scale. Some of the characterizations are carried out on the paste as sand

does not play a role in the hydration process; it only improves the mixing process, affects the rheological properties, reduces heat release during hydration and reduces shrinkage.

3.1 Materials and procedures

a) Reference mix-design: mortar

A low Water/Cement ratio of 0.3 along with a common polycarboxylate plasticizer is used (0.15dry weight%/cement) in order to have self-consolidating type of behavior.

The designed mortar is prepared with a Perrier mixer using the same mixing protocol in order to ensure tests reproducibility. The sand is first mixed with part of the water at low speed (140rpm) during 1 minute. Then, after a waiting period of 4 minutes to allow water absorption, cement is introduced and mixed at low speed during 1 minute. Remaining water and admixture are introduced during the following 30 seconds at low speed. Finally, the material is mixed at high speed (280rpm) during 2 minutes.

In the fresh state, the reference mortar is fluid (spreading diameter is 260mm with a minicone - 60mm in height, 70mm in smaller diameter and 100mm in higher diameter). Air content is close to 3%.

b) Paste

For some specific tests, sand is not added to avoid diluting the formed hydrates. The mix-design of the cement paste W/C (0.30) and admixture amount (0.15dry weight%/cement) are remained the same as in the reference mortar.

3.2 Raw materials analysis

Here are described the raw materials analysis which are essential to the interpretation of the hydration process.

a) Cement analysis

The Portland cement chosen (Le Teil) has a low alkaline concentration. The density of cement is 3.15g/cm^3 and its specific surface (Blaine measurement) is 3560cm²/g. The composition of the cement obtained with X-Ray diffraction and X-Ray fluorescence is provided in *Table 1* and *Table 2*.

.

Table 1. X-ray diffraction analysis of the cement CEM I – Le Teil used in all the experiment carried out during the research work.

Alite mono C_3S $(3CaO.SiO_2)$%	Belite C2S $(2CaO.SiO_2)$ %	Ferrite C_4AF $(Al_2O_3FeO_3$-4CaO) %	Cubic aluminate $(3CaO.Al_2O_3)$ %	Ortho aluminate $(Na_2O.Al_2O_3)$ %	Lime CaO %	Portlandite $Ca(OH)_2$ %	Periclase MgO %
68.30	18.30	7.10	1.20	0.00	0.40	0.00	0.20

Arcanite K_2SO_4 %	Quartz SiO_2 %	Calcite $CaCo_3$ %	Gypsum $CaSO_4.2H_2O$ %	Hemihydrate $CaSO_4.1/2H_2O$ %	Anhydrite $CaSO_4$ %	Dolomite $CaMg(CO_3)_2$ %	Phase X %
not calc	0.30	2.10	0.40	0.60	1.10	not calc	not calc

Table 2. X-ray fluorescence analysis of the cement CEM I – Le Teil used in all the experiment carried out during the research work.

SiO_2 %	Al_2O_3 %	Fe_2O_3 %	CaO %	MgO %	K_2O %	Na_2O %	SO_3 %	TiO_2 %	Mn_2O_3 %	P_2O_5 %	Cr_2O_3 %	ZrO_2 %	SrO %	Water loss %	Total %
22.56	2.89	2.23	67.10	0.85	0.17	0.13	2.17	0.14	0.03	0.09	Low	0.02	0.15	1.34	99.89

The particles size distribution of the cement characterized by its D10 is 2.46 µm; D50 is 13.68 µm and D90 is 37.56 µm.

b) Sand analysis: PE2LS Fulchiron

The specific density of sand is 2.65g/cm^3 and its absorption coefficient is 0.21%. The particle size distribution of the sand is characterized by its D10 is 171µm; D50 is 245µm and D90 is 350µm. The composition of this siliceous sand is described below:
SiO_2: >98%, Al_2O_3: <0.90%, Fe_2O_3: 0.05%, CaO: <0.05%, K_2O: <0.70%, TiO_2: <0.06%.

c) Particles size distribution of cement and sand

The cumulated particle size distributions of sand and cement are plotted in *Figure 13*.

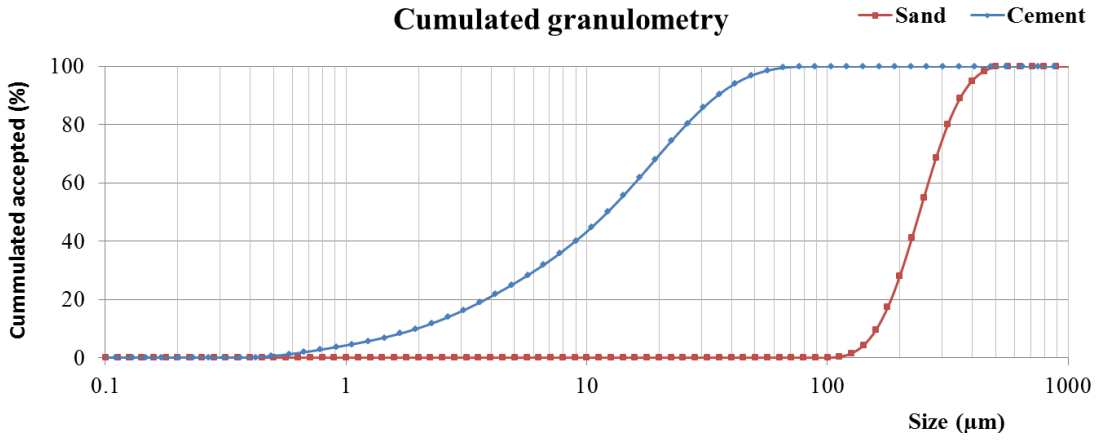

Figure 13. Cumulated particles size distributions of the sand and cement used in the reference mix-design.

d) Glenium 27 analysis

Glenium 27 is a common PCP (PolyCarboxylate Polyoxide) admixture from BASF which is a comb-shaped polymer as shown in *Figure 14*. In its commercial liquid form, the density of the Glenium 27 is 1.042g/cm^3 with a dry content of 20.6%. Its pH is 5.78.

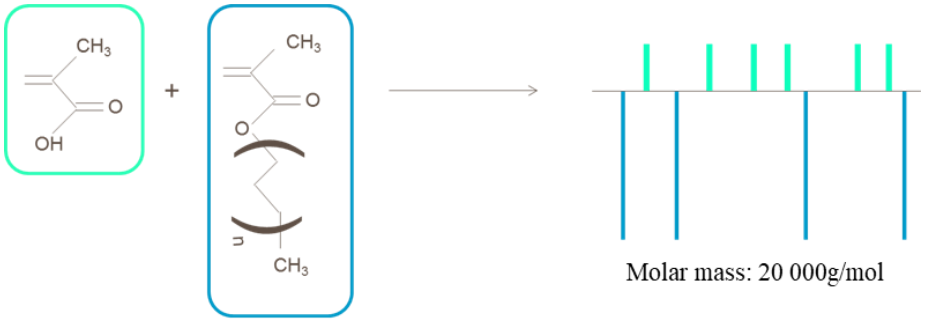

Figure 14. Illustration of Glenium 27 polymerization.

3.3 Strength of hardened mortar

The mortar mix-design is composed of a significant part of paste, this induces a compressive strength at 28 days of 120MPa (1 day: 43MPa, 7 days: 99MPa). The flexural strength at 28 days is 17MPa (1 day: 8MPa, 7 days: 16MPa).

3.4 Hydration stoppage principle

Hydration stoppage is one of the ways to stop the cement hydration. The resultant sample is a powder. Among the other techniques there is also, the freeze-drying process or heating the sample in an oven (105° in order to evaporate water). Whatever the stoppage process, the hydrates microstructure can be altered. Solvent exchange is used in this study because the microstructure alteration is limited, chemically bound of water in the hydrated phase are preserved. It is important to note that the best way to characterize the microstructure is a continuous and nondestructive characterization, but some techniques of analysis require stopped samples in order to provide an instantaneous picture of the ongoing process.

Solvent exchange is performed on fresh mortar or paste with two washes with acetone (boiling point: 56°C) and one with ether (boiling point: 35°C) on a regular Buchner filtration system. The solvent removes water because of the better affinity of the solvent in the pores compared to water thus hydration is stopped because there is no more water available for the cement. Then the solvent is evaporated before the analyses.

In the following, different techniques are used in order to characterize cement hydration and especially hydrates formation.

4. Hydrates identification

Different chemical analyses are required for the hydrates identification. All methods are complementary. *Table 3* summarizes the different purposes of each method.

Table 3. Summary of the different techniques used in this chapter and their expected results.

Method		**Expected result**
Conductimetry		Kinetics of hydration, hydrates dissolution.
X-ray diffraction		Quantification but amorphous (C-S-H are not observable).
Thermal analysis	**TGA**	Hydrates identification without C-S-H, ettringite differentiation.
	DTA	TGA complementary with C-S-H, ettringite differentiation.
NMR		Proton H environment thus free water evolution.

4.1 Conductimetry

a) Theoretical part

Conductimetry allows following the evolution of the ion species concentration and then evaluating the hydration kinetics. During cement hydration there is a competition between dissolution and precipitation reactions. Many researches have shown that there is a link between the electric conductance of a cement-based material and its hydration degree.

Therefore, it is interesting to follow the evolution of cement paste conductance with time in order to follow the ion species concentration. The *Table 4* gives an example of the common conductivity of ions found in pore solutions of cement-based materials.

Table 4. Example of ions conductivity equivalent at 25°C.

Ions	H^+	OH^-	Na^+	Cl^-	K^+	Ca^{2+}	SO_4^{2-}
Equivalent conductivity (10^{-4} $S.m^2.mol^{-1}$)	350	192	50.9	75.5	74.5	120	158

For conductivity measurement, σ_c [21] two electrodes are used. L is the distance between the two electrodes. S is the area of the electrode [m²].

The conductance of an ionic solution (in Siemens) is defined as the opposite of the resistance: $G = 1/R$. It is also defined as Eq.(1).

$$G = \sigma_c . \frac{S}{L} = \frac{\sigma_c}{K} \quad (1)$$

K is a cell constant defined as the ratio of the distance between the electrodes over the area of the electrodes L/S [in cm^{-1}]. It is determined using a standard sample with a known conductivity for a specific temperature in order to correct the effect of the circular electrode. σ_c is the conductivity of the solution.

Thus, the goal is to measure the conductivity defined as Eq.(2).

$$\sigma_c = \frac{K}{R} = K . G \quad (2)$$

In order to obtain the conductivity value of a sample only 1/R or G have to be determined. Tension *U* between the two electrodes is imposed. The intensity *I* is measured and conductivity is defined as Eq.(3).

$$\sigma_c = \frac{I}{U} . K \quad (3)$$

Thus, the conductivity evolution can be captured by continuously measuring the intensity between the plates. When the conductivity decreases, this means that precipitation is faster than dissolution.

Figure 15. Photo of the conductivity cell to monitor cement hydration.

Experimentally, the device is calibrated with buffer solutions (*Figure 15*). One of the risks of the technique is mortar shrinkage: if there is no contact between the material and the electrode, the device cannot proceed to the measurement. This is why for mortars and pastes the surface of the electrodes is larger than for suspensions.

The container for the measurement is opened at the top. It is placed in the laboratory; there is no compensation of the temperature increase in the cell. The electrodes for the measurement are placed on the inner surface of the cell. The limit of detection is from 2mS.cm^{-1} to 60mS.cm^{-1}. The measuring cell is 117mm in diameter and 106mm high, the sample volume is 47mm in diameter and 85mm high.

b) Results

Conductivity of the solution is plotted over time between T0 and 24 hours (*Figure 16*). The overall tendency is a decrease of conductivity.

More precisely, during the first hour, there is a short increase caused by the dissolution of the anhydrous substances related to an increase of the ions quantity. C_3A (around 1% in Le Teil cement) species is the first one to dissolve. There is also the release in the solution of calcium ions, hydroxides, silicates, aluminates, sulfates… The conductivity increase at the beginning is mainly due to C_3S because it represents 68% of the species inside the cement Le Teil. Moreover, regarding *Table 4* the variation of conductivity is impacted by calcium dissolution. The tricalcite silicate dissolution increases the concentration of calcium and silicate ions:

$Ca_3SiO_5 + 3H_2O \rightarrow 3\ Ca^{2+} + 4\ OH^- + H_2SiO_4^{2-}$

When the solution is sursaturated regarding the C-S-H (K_s reached), there is C-S-H precipitation with the following equation:

$x\ Ca^{2+} + 2(x-1)\ OH^- + H_2SiO_4^{2-} \rightarrow (CaO)_x\text{-}(SiO_2)\text{-}(H_2O)_y$

with 0,6 < x < 2 (most of the time x=1.7).

Then, the ions sursaturation induces the precipitation of Portlandite because the solubility coefficient is reached. Between 2 and 7 hours the conductivity decreases because of Portlandite precipitation. Around 7-8 hours after the cement is in contact with water, the kinetic accelerates. At

that point of hydration, there is a slope change: the C_3S hydration accelerates. This acceleration is from germs formation, when the surface of the anhydrous is completely covered, the hydration kinetics changes.

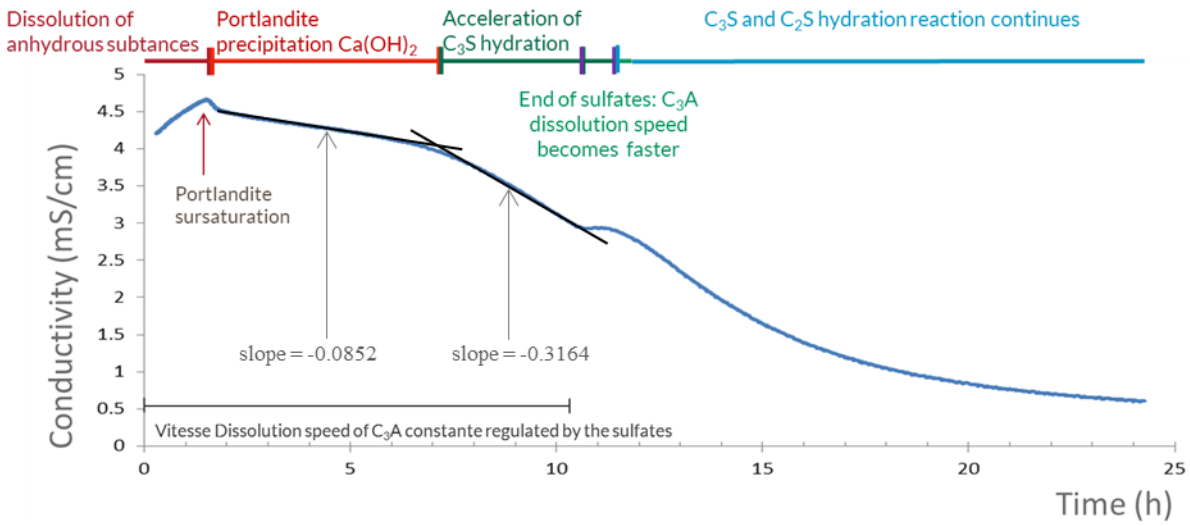

Figure 16. Mortar conductivity evolution over time highlighting the different observable stages cement hydration.

Around 10 hours, there are no more sulfates (gypsum is consumed). Then, ettringite transforms in monosulfate aluminate of hydrated calcium [21].

With gypsum: (C_3A)+ $3CaSO_4.2H_2O$ + H_2O → $C_3A.3CaSO_4.32H_2O$ (ettringite)

After gypsum consumption: C_3A + H_2O → $C_3A.CaSO_4.14H_2O$

As a result, the dissolution speed of the C_3A decreases. It results in a diminution of conductivity, which means there is more precipitation than dissolution. After this short period, C_3S and C_2S hydrations continue as conductivity decreases. It is possible that the admixture increases the Portlandite precipitation phase because an admixture delays hydration time.

It is important to be careful with this analysis: **conductivity does not directly represent hydration kinetics**, because each ion has a different signal, this will influence the measurement. This analysis gives us the indication that there is an **acceleration of hydration kinetics around 7 hours**. This is the reason why X-ray diffraction is performed.

4.2 Cristallography with X-ray diffraction

a) Protocol

This analysis is carried out at paste scale. The aim of this analysis is to identify the crystalline phases (C-S-H is non crystalline, difficult to see with this technique). Samples are stopped every hour from 4 to 11 hours after mixing, and at 24 hours. It is a classical way to characterize materials. It allows quantifying crystalline part of a material. The order of magnitude of the electromagnetic radiations is relative to the Angström. A crystal is formed by atoms, ions or molecule with a pattern which appears periodically in the structure. The interatomic distances are of the order of magnitude of the wave length of the X-ray [22]. The first structure to be determined was a structure of NaCl by William Lawrence Bragg and his father Sir William Henri Bragg in 1913. The technique is based on

observing an X-ray beam hitting a sample (by varying scattered angle, polarization wavelength or energy).

b) Production of X-ray

Electrons of a heated tungsten filament are accelerated with an electric field and are projected on an anode (or anticathode) and X-ray are produced (*Figure 17*).

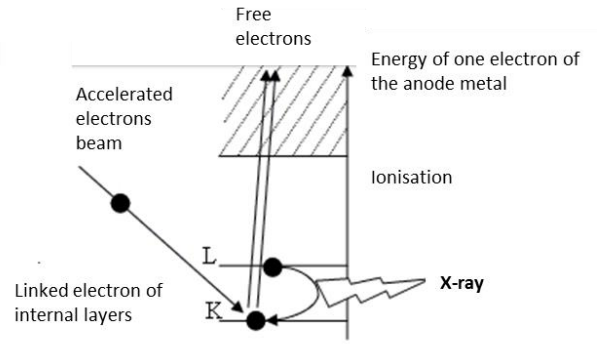

Figure 17. X-ray production illustration needed for crystallography.

Another source of X-ray is the synchrotron which creates intense ray which permits to characterize small crystals. This phenomenon is known as elastic scattering. The technique is based on Bragg law (*Figure 18*).

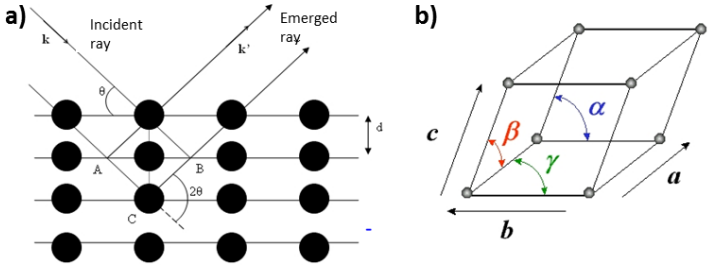

Figure 18. Scheme of a) Bragg law for the refraction of a incident ray ; b) Elementary pattern of a crystal.

The *Figure 18* represents the cross-section of reticular plans. The optic difference in courses distance between two rays is monitored. The analysis can be done on a powder (when the sample is not monocristalline).

c) Phase identification

When the diagram is obtained, the intensity is compared to the PDF (Powder Diffraction File) data. *Figure 19* is an example of a X-ray diffraction profile.

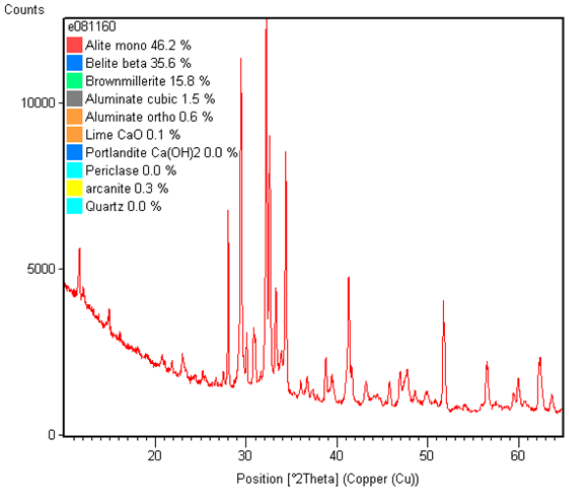

Figure 19. Example of X-ray diffraction curve.

d) Rietveld method

The method has been developed by Hugo Rietveld in 1969 and was used to quantify different crystalline phases. This method allows identifying each hydrate thanks to a huge amount of graphs inside the software; it compares the obtained graph and the calibrated scan and permits to identify the hydrates by this comparison. By calibration of known material it is possible to compare the quantity of each species. It is important to note that **C-S-H are not crystalline** phases whereas the majority of anhydrous phase are crystalline as well as Portlandite and ettringite.

The diffractometer X-ray used is the Philips PANalytical X'Pert pro. The stopped samples are introduced as a powder inside the X-ray cell (see *Figure 20*).

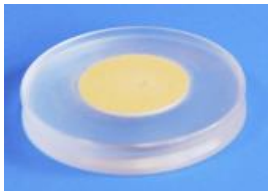

Figure 20. Picture of X-ray diffraction cell: the sample is powder like at the center of the cell.

e) Results

Each phase quantity is represented (*Figure 21*) as a function of the time on stopped paste samples. Only the principal phases are represented.

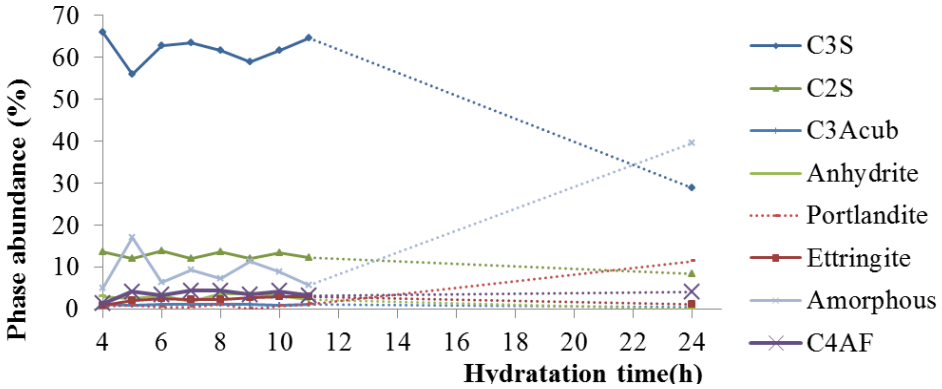

Figure 21. X-Ray diffraction composition as a function of hydration time for paste stopped samples of the reference mix-design.

Overall, there is not any remarkable variation between 4 and 11 hours. The variations during this period might be because of the preparation of the sample (differences in particle size distributions).

At 24 hours, C_3S quantity decreases because it has reacted. The amorphous quantity increases because C-S-H have been created and they are non-crystalline. C_2S quantity decreases a little and it is possible to see Portlandite formation. The ettringite quantity is low because C_3A quantity was low.

It is important to highlight that the amorphous quantity is determined as the sum of all non-crystalline species but as well the non-identified crystalline phases, so this fraction can be overestimated (as the sum of all phases has to be 100%). It also could explain the variations between 4 hours and 11 hours. The main conclusion is the confirmation that the formed hydrates come from the hydration of C_3S.

To complete this analysis, differential thermal analysis is done in order to determine and confirm hydrates formation.

4.3 TGA: Thermogravimetric analysis

a) Theoretical Part

A sample undergoes temperature variations. Thermogravimetric analysis permits to monitor the mass of the sample over time as the temperature increases. The technique gives information about the sample transformations for example phase transition, absorption or desorption. For concrete, the analysis can be carried out on paste or mortar. It allows characterizing and identifying hydrates formation; for instance, to study the kinetics phases formation during cement hydration. It has been chosen to analyze a paste sample to maximize the hydrates detection. DTA derivative curve of thermogravimetric analysis is used.

b) Thermogravimetric analyzer

The analyzer consists on a precision balance with a sample pan (in alumina) located inside a furnace with a programmable controlled temperature. Usually the temperature increases at a constant rate. The thermogravimetric analyzer is a TGA/DSC 3^+. The reference is an empty alumina crucible. The thermocouple is placed underneath the sample.

c) Experimental part

For the analysis, the sample is powdered. The sample is placed inside an alumina crucible. The air atmosphere is replaced by nitrogen (10 minutes at 30°C). Then, the temperature is risen 10°C/min up to 1000°C. At the end, the sample is left for 15 minutes at 1000°C. The sample weight is around 1 gram. The analyzed samples were obtained from the stopped paste mix-design to increase the intensity.

d) Results and discussion

TGA is done on samples stopped every hour between 4 and 11 hours and at 24 hours. The evolution is the derivate of the TGA results. Every curve is shifted on the vertical axis in order to differentiate the picks as plotted in *Figure 22*.

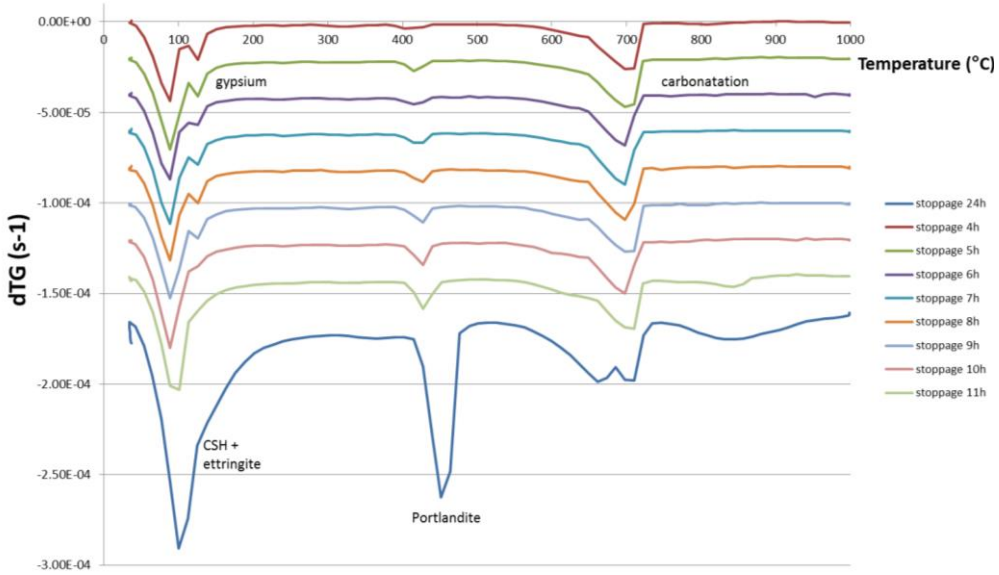

Figure 22. Hydrates formation over time analyzed with TGA for the reference mix-design stopped every hour from 4 to 11 hours and at 24 hours. The curves are shifted to the bottom for visibility.

The same phenomena than in TDA are observable but the temperatures are different. Around 80°C, the observable picks are from ettringite and C-S-H, it is not possible to differentiate them with this technique. Gypsum is observable around 120°C, it is not present after 9 hours, it is the time where massive hydration occurs as one can see, and hydrates picks increase a lot. Portlandite is present from the first hours of hydration, which was not observed on the other techniques, the analysis is conveyed on paste and not mortar, so the signal is higher. It appears that the sample is less diluted, which can increase some phenomena. Moreover, **the admixture is less absorbed** in a paste than in a mortar thus there can be a difference of hydration times.

4.4 DTA: Differential thermal analysis

a) Theoretical part

The DTA technique permits to characterize the chemical composition by observing the thermal degradation of the sample when heated. It is based on the energy transfers due to chemical reactions (such as absorption and emission). The analysis is performed on stopped samples of mortar.

The temperature of a sample is compared to the one of the reference inert material while temperature is increasing. The reference sample is a material close to the cementitious material in terms of calorific properties and density but is not supposed to have any thermal variation due to chemical reactions. The sample is placed in a specified atmosphere in a furnace. The evolution of the temperature is defined inside the program. A differential thermocouple measures the difference between the reference temperature and the sample temperature; the two samples are placed symmetrically inside the furnace (*Figure 23*).

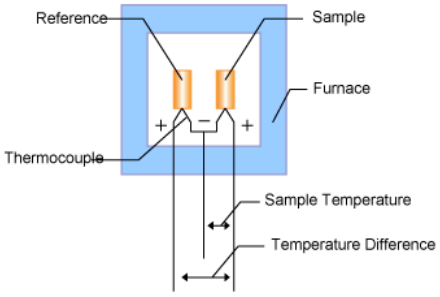

Figure 23. Scheme of DTA principle, the sample is placed inside a furnace chamber, equipped with thermocouple [23].

The thermocouple measures the furnace, the reference and the sample temperatures. For each material, maximum of temperature differences are recorded (*Figure 24*). Those differences are characteristic of pure compound, and comparing the recorded results to a reference materials database which make possible to identify the sample composition. Usually α-alumina is used as reference.

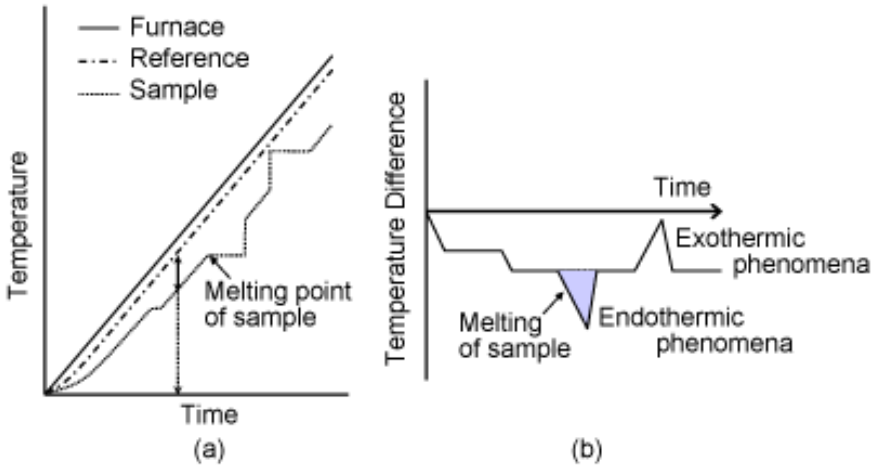

Figure 24. Principe of DTA measurement: evolution of the temperature of the different element on the left which allow to plot the temperature difference on the right.

b) Analyser

The analyzer has been made by ERALY especially for LafargeHolcim Research Center, its particularity consists in having the thermocouple inside the sample (compared to TGA where the thermocouple is outside of the sample). The sample weight is 1g (powder), the temperature ramp is 20°C/min. The sample was heated between 30°C and 600°C.

The sample is placed inside a small tube in quartz. The reference material is alumina. The two small tubes are open at the top and placed inside an air environment and the temperature is risen from

30°C to 600°C at an increase rate of 20°C/min. Exothermic reactions are represented in the same direction as the vertical axis (upper side of the graph).

c) Results

Hydrates have endothermic picks that allow characterizing their degradation. Usually, C-S-H degradation occurs below 100°C, ettringite around 150°C and Portlandite above 550°C. Here, as the experiments were performed without removing the sand, quartz phase is visible around 575°C. An illustration of those picks is presented on *Figure 25*.

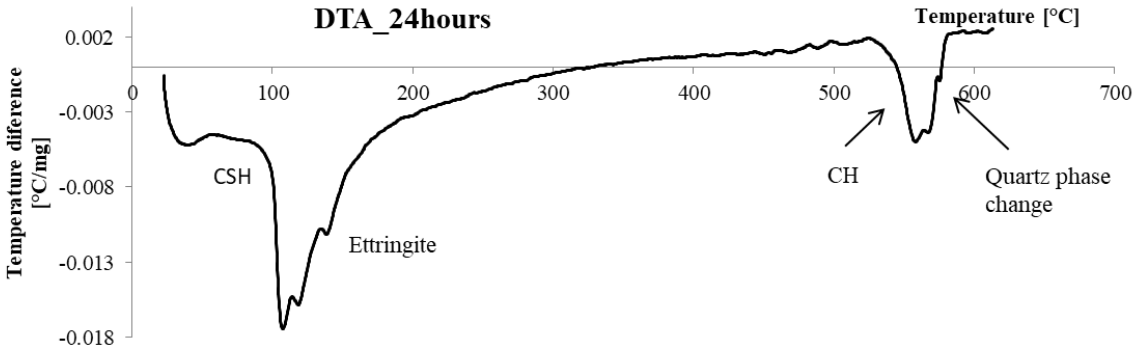

Figure 25. Explanation for the interpretation of DTA curve: evolution of the temperature difference between the sample and the reference as a function of temperature of the furnace, with the identification of C-S-H, ettringite, CH and the Quartz phase change.

DTA analysis is obtained for samples stopped at different ages ranging from 4 to 24 hours after the cement and water mixing. All curves are plotted on the same graph with a vertical offset to allow seeing the evolutions of the thermal changes (*Figure 26*).

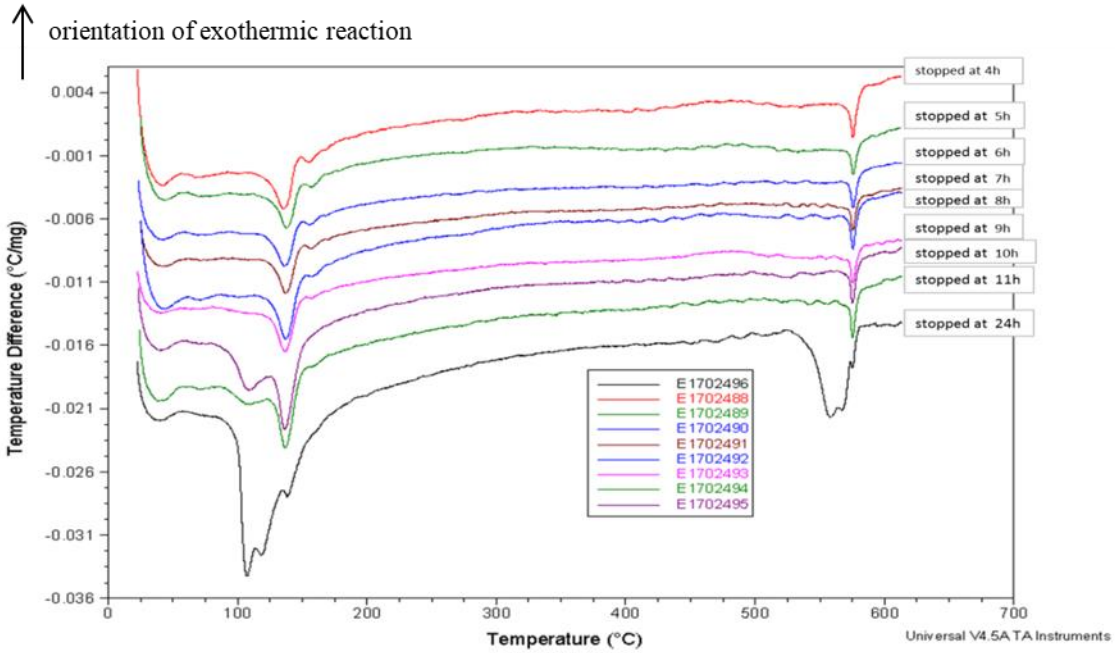

Figure 26. Hydrates formation over time analyzed with DTA. The curves are shifted to the bottom to better visibility, thus the y axis origin is not correct for every curves.

Ettringite pick is visible from the first hours, which means that it is formed from the beginning when cement and water get in contact. After around 9 hours, C-S-H pick begins to change: its formation is observable. Gypsum pick is next to the right of ettringite pick. There is no more gypsum after 9 hours because the gypsum pick is not observable anymore after this time. This means that after 9 hours, calcium monosulfoaluminate is formed. At 11 hours, Portlandite does not seem to be created, but at 24 hours a large pick around 550°C is observable: Portlandite is formed.

Those results (time of apparition of the hydrates) will be compared with the other analyses.

4.5 NMR Relaxometry: Nuclear Magnetic Resonance

NMR is used for different applications, such as MRI, chemistry compound characterization... It is an interesting technique because it is non-destructive and non-invasive. NMR permits to observe the variations of the magnetization of a substance core, after an electromagnetic perturbation [24]. Hydrogen is sensitive to magnetic field applied in NMR because of its spin (1/2). A specific type of NMR analysis is called relaxometry which is used for cement hydration monitoring especially for water consumption [25] [26] [27] [28].

a) Protocol

NMR Relaxometry

Relaxometry is a very interesting method to characterize porous media. The goal of this study is to determine the water quantity evolution over time consumed by the cement hydration. In relaxometry technique, the parameter studied is the difference of relaxation times. NMR relaxometry is used to characterize different parameters such as porosity distribution, surface properties, wetting properties… Microstructure of cement-based materials is studied over the last decades. The early NMR studies following the hydration of Portland cement and tricalcium silicate pastes were conducted by Blinc et al. in the late 1970s [27]. Since then, a lot of papers can be found about cementitious materials studied with this technique.

Those experiments were performed in the laboratory of the University of Surrey with Agata Gajewicz and Peter Mc Donald.

Water evolution monitoring

RMN relaxometry is used in order to follow the evolution of water (the confinement of the hydrogen of H_2O). It has been shown that it is possible to follow water quantity continuously in a porous media, as one can see on *Figure 27*.

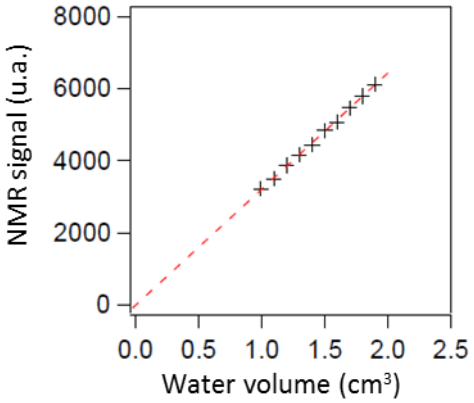

Figure 27. NMR signal proportionality with water quantity.

The hydrogen spins mobility depends on the characteristics of the environment they are enclosed in [27]. Depending on the state of water and more precisely on the dynamic influenced by the interactions at the surface, liquid water or solid water (in the hydrate) do not have the same relaxation time (after a magnetic pulse) because of the environment of the protons. Different states of water can be divided as evaporated water and non-evaporated water. The evaporable water is divided into gel water, the one inside the pores of C-S-H and capillary water as illustrated in *Figure 28*.

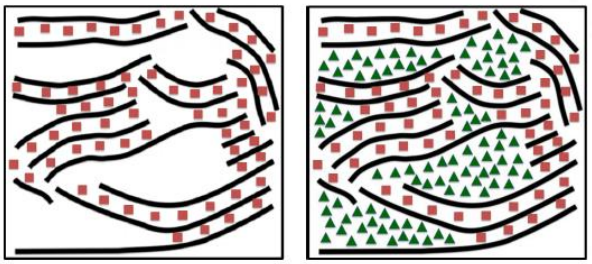

Figure 28. C-S-H representation: in red interlayer water and in green gel pore water [29].

It differs from solid water because of the environment of the hydrogen. The relaxation time is shorter for solid water than it is for liquid water because it depends on the side of the pore as one can see on *Figure 29* [30].

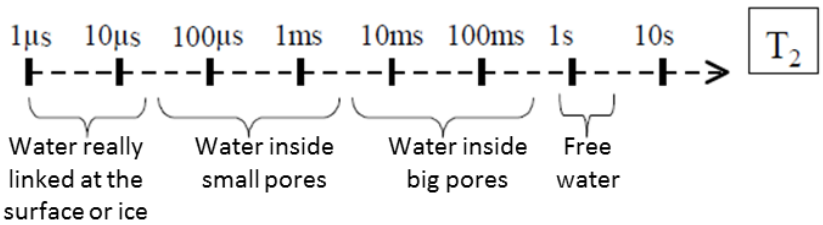

Figure 29. Relaxation time T2 scale highlighting water environments.

T1: spin-lattice relaxation time measurement

T1 time depends on hydrogen atoms mobility. T1 is shorter when hydrogen is linked to large molecules. The average of ultra-pure water (without O_2) is around 3 seconds. Tap water (25°C) is around 1 to 2 seconds, water inside the pores varies from couple milliseconds to couple hundreds milliseconds.

Two non-correlated times can be defined:

- **T1 is the spin-lattice relaxation time or longitudinal relaxation time,**
- **T2 is the spin-spin relaxation time or transverse relaxation time.**

T1 and T2 can range from couple milliseconds to couple seconds.

In Appendices, the description of the magnetic impulsion deviation, the Hahn sequence, CPMG (Carr Purcell and Melboom Gill Pulse Sequence) are described.

b) Sample preparation

In order to prepare the sample a different mixer than usual was used as it is shown on *Figure 30*.

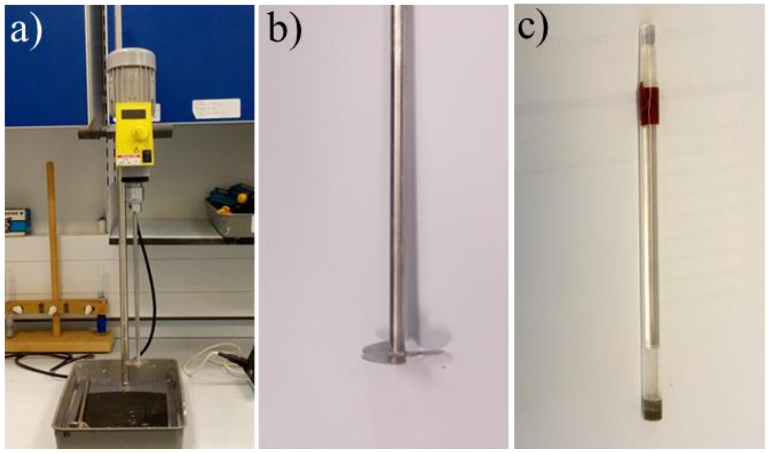

Figure 30. a) and b) Photo of the mixing design c) Photo of the sample inside the tube for NMR measurement in continue on the mortar reference sample.

Then, a small amount of the sample (around 1.5g) is placed inside a tube which is sealed (*Figure 30. b*). The interpretation and data analysis is carried out by Agata Gajewicz using the same method of data treatment as in her PhD thesis [29].

c) Results

Hydrogen relaxation (hydrogen environment) is monitored. As seen before, capillary water which is the free water available for hydration is dissociated from the other types of water based on their environment. The solid part of water means water transformed in **ettringite** and **Portlandite**. During the experiments, there was a small amount of bleeding at the surface; it is what is called **surface water**. Finally, hydrogen is not visible inside the C-S-H hydrates but around. As described above, there are two forms of water linked to C-S-H (*Figure 31*): the water enclosed between C-S-H sheets: **interlayer water** and the water inside the cluster of C-S-H called **gel water in C-S-H**, this water is used to create C-S-H and can be transferred to interlayer water.

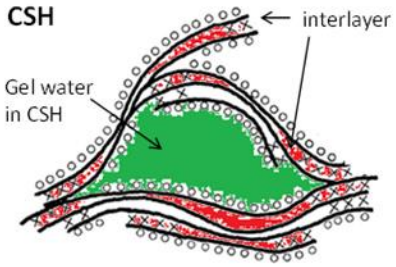

Figure 31. Scheme of water in C-S-H which differentiate the interlayer water and the gel water [31].

As the sample is sealed, the total amount of hydrogen is considered constant during the experiment. The evolution of the amount of each hydrogen environment is monitored over time until 24 hours (*Figure 32*): in green capillary water, free water and available water; in red, the surface water due to bleeding; in purple the gel water; in light blue the interlayer water and in dark blue Portlandite and ettringite.

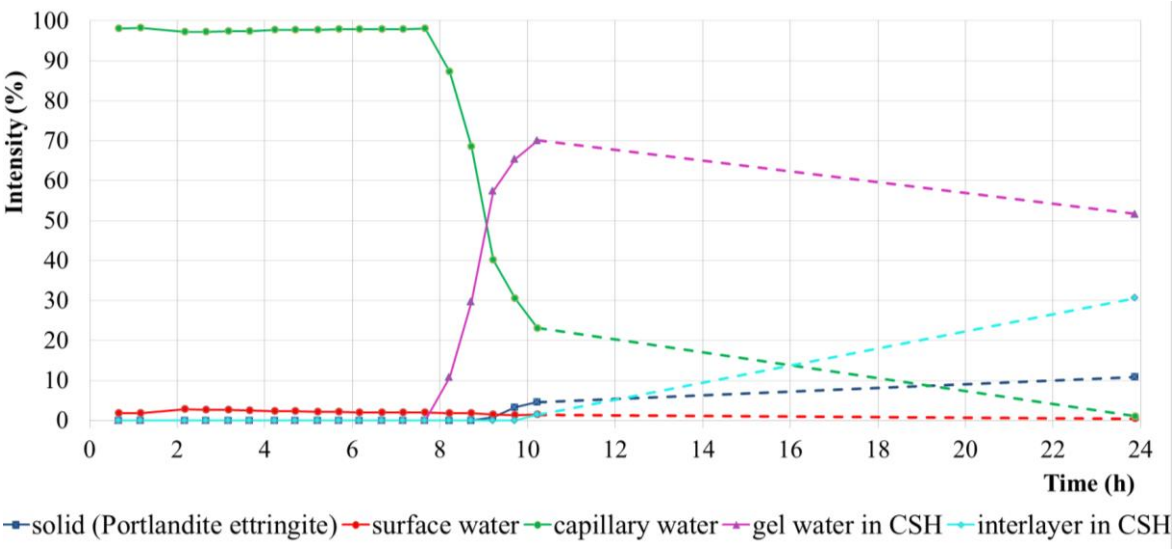

Figure 32. Hydrogen environment monitoring over time with NMR measurement on the reference mortar mix-design: one point every half hour to 11 hours and a point at 24 hours.

The surface water is approximately constant. The capillary water remains constant until 8 hours when the amount of gel water increases drastically. Around 9 hours and half, solid water increases slowly. At 24 hours the amount of gel water decreases (compared to 10 hours and half) because interlayer water amount increases. This analysis permits to confirm that the massive hydration of the system begins around 8 hours, as seen with the others techniques. The analysis is done twice on two different samples, in red the evolution of the capillary water the first day and the repetition with another sample in blue (*Figure 33*). It shows that the measurement was reproducible.

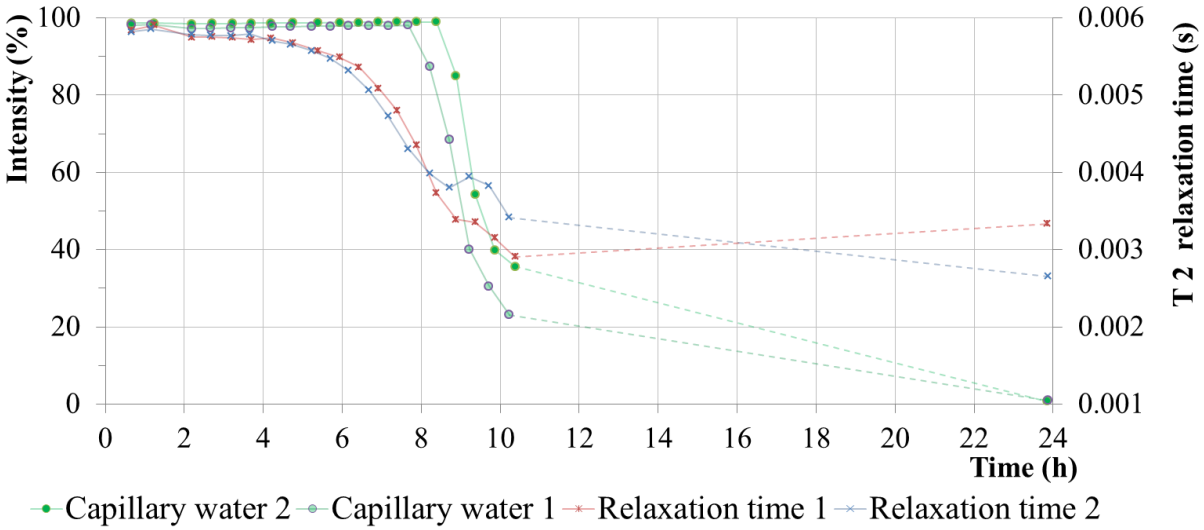

Figure 33. Evolution of the NMR signal intensity and T2 evolution as a function of time. Points: reproducibility of two tests performed using on the same material and the same protocol, Cross: T2 evolution.

The relaxation times (T2) evolutions are also visible on *Figure 33*. It is directly proportional to the size of the pores. In order to determine the proportionality coefficient, other parameters have to be determined; that is not done for this material. Nonetheless, T2 can be related to the average pore size evolution.

On the graph, the green dots are the free water evolution as represented on *Figure 33* with a repetition. T2 is represented with the red and blue crosses. Pore water diameters decrease around 5 hours after T_0 but water quantity stays constant until 8 hours. This means that the pores are smaller but there are more pores between 5 and 8 hours. Then, at 8 hours the water quantity sinks drastically. Around 9 hours, T2 seems to have a small increase, this might be due to an increase of air bubble as it expands with the suction effect.

Thanks to NMR relaxometry free water quantity evolution is obtained. In order to characterize the microstructure of the mortar, pore size distribution is obtained in the following chapter using mercury intrusion porosimetry (MIP). Hydrates time formation were identified. In the following, their effect on mechanical behavior is studied.

5. Mechanical consequences

5.1 Yield stress evolution

Hydrates formation shapes the microstructure of hardening cement paste, mortar and concrete. Structural build up is the direct consequence of hydrates formation. Hardening is the consequence of hydration. Structural build up can be characterized by the increase of yield stress of the cementitious material left at rest. A state of the art about rheological parameters (shear stress, shear rate, viscosity and yield stress) is presented in *Chapter 3. section 3*.

Evolution of the static yield stress of mortar samples left at rest-obtained with vane measurement on undisturbed sample and Vicat setting time measurement-is plotted on *Figure 34*.

Static yield stress is measured using stress growth procedure as defined in [32]. It consists in shearing the material with manual scissometer at a very low shear rate in order to make viscous effect negligible. The vane dimensions are decreasing with the hardening of the material in order to be in the

range of measurement. Penetration depth obtained with Vicat needle (1.1mm in diameter and 36mm in height) is also used to compute the yield stress of the material using the theory presented in [33]. Note that correction of the bottom end effect due to the flat surface of the needle has been made using soil mechanics theory on basements (Eq.(4)).

$$\tau_0 = \frac{4.m_{Vicat}.g}{a.\pi.D^2} + \pi.D.h_{Vicat} \quad (4)$$

with m_{Vicat} the mass of the dropping needle, h_{Vicat} the penetration depth and D the needle diameter. a is the bottom end coefficient taken at 9 for this study. This value is in agreement with Eurocode 7 recommendation (European standard for design of building basement) which provides values of a parameter according to the internal friction angle of the soil (5.14 for a friction angle of 0° and 10.98 for a friction angle of 15°). The a parameter is here chosen in order to provide a good agreement between vane and penetration measurements of yield stress.

Yield stress begins to increase at around 4 hours, then grow faster around 8 hours, which is the time of C-S-H formation. Yield stress measurements will be of interest for estimation of shear strength of the material in *Chapter 3*.

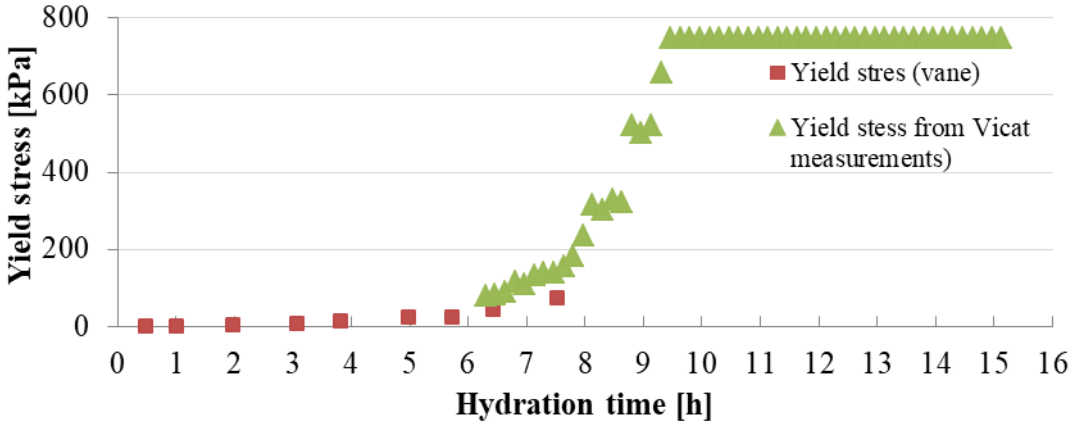

Figure 34. Yield stress evolution over time characterized with vane test and Vicat measurements on the mortar reference mix-design.

5.2 Hydrates adhesion

a) Principle

In this part, hydrates adhesion to a metallic surface is characterized. The test developed to characterize hydrates adhesion, simply consists on measuring hydrates adhesion on a polymer disc covered with a metal sheet placed on the mortar surface and removed at different hydration times. The discs are lifted thanks to a very sensitive traction machine (*Figure 35*).

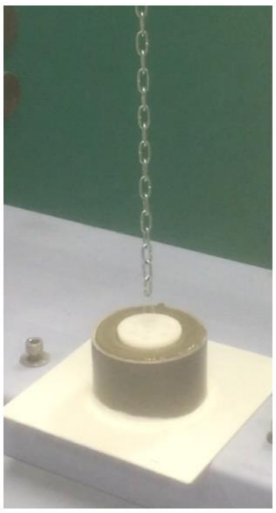

Figure 35. Photography of one disc situated on mortar surface and pulled-off with the traction machine.

Two types of discs are used in order to isolate the different phenomena occurring at the interface and creating adhesion to the surface, mainly the effect of water suction and hydrates adhesion. Every disc is composed of a plastic part, which reduces the mass so it does not sink and stays at the surface of the mortar. The second part is a metal part. For the first type of discs, the metal part is a smooth sheet of steel representative of a real formwork. The other type is composed of sintered and therefore porous metal for the surface in contact with mortar. Then the plastic part differs in order to compare the adhesion with the effect of hydrates bounding and water suction or only hydrates bounding. The principle of the different types of discs is developed in the following.

b) Experimental procedure

Test specifications

Fresh mortar is placed into small boxes (80mm-in-diameter). Each disc is placed at the surface of mortar at the same time (T_0 + 10 minutes). At a defined time, the disc is lifted at a speed of 0.1mm/s with a Shimadzu tensile machine in displacement-controlled mode. The force needed to remove the disc is recorded to calculate the lifting stress.

Smooth discs

This type of disc (*Figure 36)*, consists of a filled plastic part (polyoxymethylene) and a steel sheet (0.1mm thick). The roughness of the surface is representative of a metal formwork, the two effects of adhesion are present: hydrates which bound to the surface and pore water suction effect.

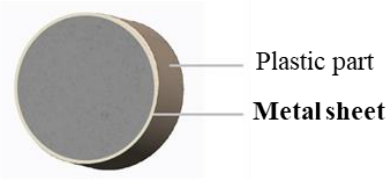

Figure 36. Scheme of the steel sheet disc formed with a metal sheet stuck to a plastic part.

The disc is 40mm-in-diameter and 0.1mm thick. Its mass is 21g.

Sintered discs

The aim of those geometry is to dissociate hydrates bounding and water suction effect. To isolate each effect, two different plastic parts are developed. In *Figure 37.b*: filled plastic making the samples connected to a limited air volume with hydrates bounding and expected suction effect (partly-porous disc) whereas *Figure 37.c)*, the plastic part is drilled so that the disc surface is at atmospheric pressure and only the effect of hydrates bounding is observable. The partly-porous system has been designed to minimize the connection with ambient environment.

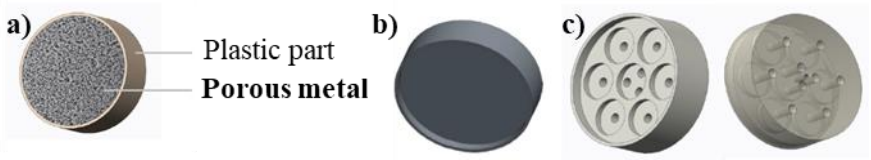

Figure 37. Scheme of sintered disc a) general view b) non-porous plastic part c) porous plastic part.

The discs are 40mm-in-diameter. The thickness is 9mm for the partly-porous disc and 10mm for the porous one. Mass of the two pucks is around 20g.

Sample confinement before tests

Storage of the boxes before pull-off tests has a real impact on the measurements. Different atmospheres are tested: ambient air environment and humid environment.

Scanning Electron Microscopy

SEM was performed to observe hydrates growing on sintered surfaces. It was carried out with a SEM at three magnifications: x 300, x 4 000, x 20 000.

c) Results

Smooth discs

Pull-off stress is measured with smooth surface every hour between 1 to 11 hours after mixing (*Figure 38*). Samples are stored in ambient air regulated at 20°C and 50% of relative humidity.

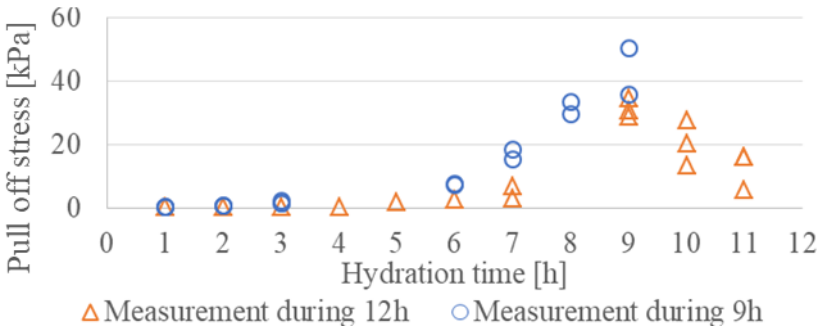

Figure 38. Pull-off stress as a function of hydration time with smooth steel surface.

There is no evolution of the pull-off stress during the first 5 hours of hydration. From 6 to 9 hours, pull-off stress increases but decreases after 9 hours. This decrease can be due to the impact of the "air entry value" of pore water pressure. This value is described in *Chapter 2*. It can be seen that there is almost no difference between the porous and partly-porous configurations. It seems that the partly-porous discs are also connected to ambient atmosphere just as the porous system.

Sintered discs

Pull-off strength is measured with the porous and partly-porous disc every hour between 1 to 7h after mixing time (*Figure 39*).

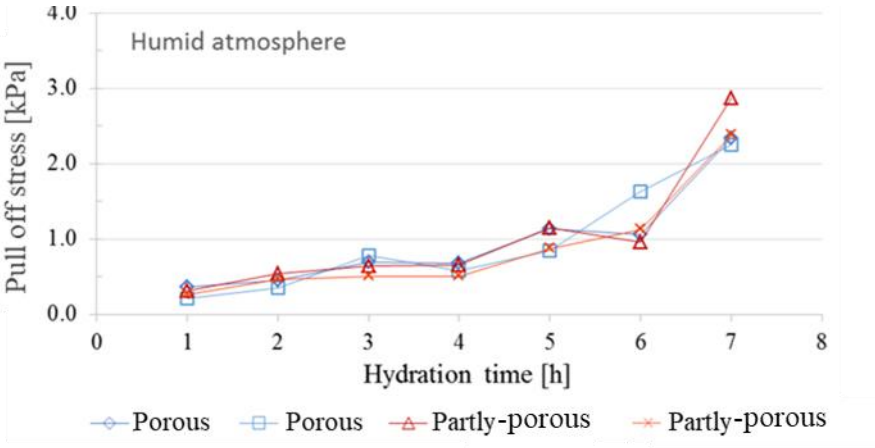

Figure 39. Pull-off stress evolution as a function of hydration time with porous and partly-porous discs stored in humid atmosphere before test.

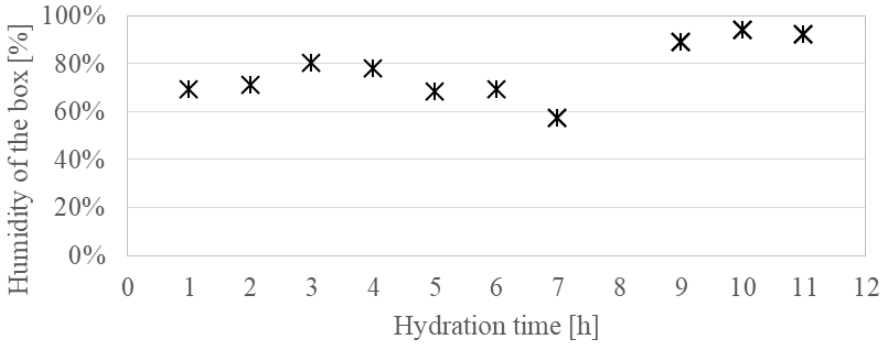

Figure 40. Humidity evolution inside the box as a function of the hydration time during the disc measurements.

From 1 to 5 hours pull-off stress is really low and approximately constant. After 6 hours, pull stress increases but is one order magnitude lower than with a smooth surface. It seems on *Figure 39* that there is no influence of porous or partly-porous characteristics on pull stress during the first 7 hours of hydration. It is important to note that condensation phenomenon appears in the porosity of the sintered disc and that therefore no water suction appears. The high relative humidity inside the curing box is plotted in (*Figure 40*).

However, the comparison of the sintered and smooth surface shows that there is a strong influence of suction effect on the pull-off strength of the disc. The development of suction leads to a magnification of the pull-off strength that can be related to the observation of shear stress increase in slipforming process for hydrating cementitious material [4].

d) SEM observations

SEM observation is carried out to observe the potential developed hydrates.

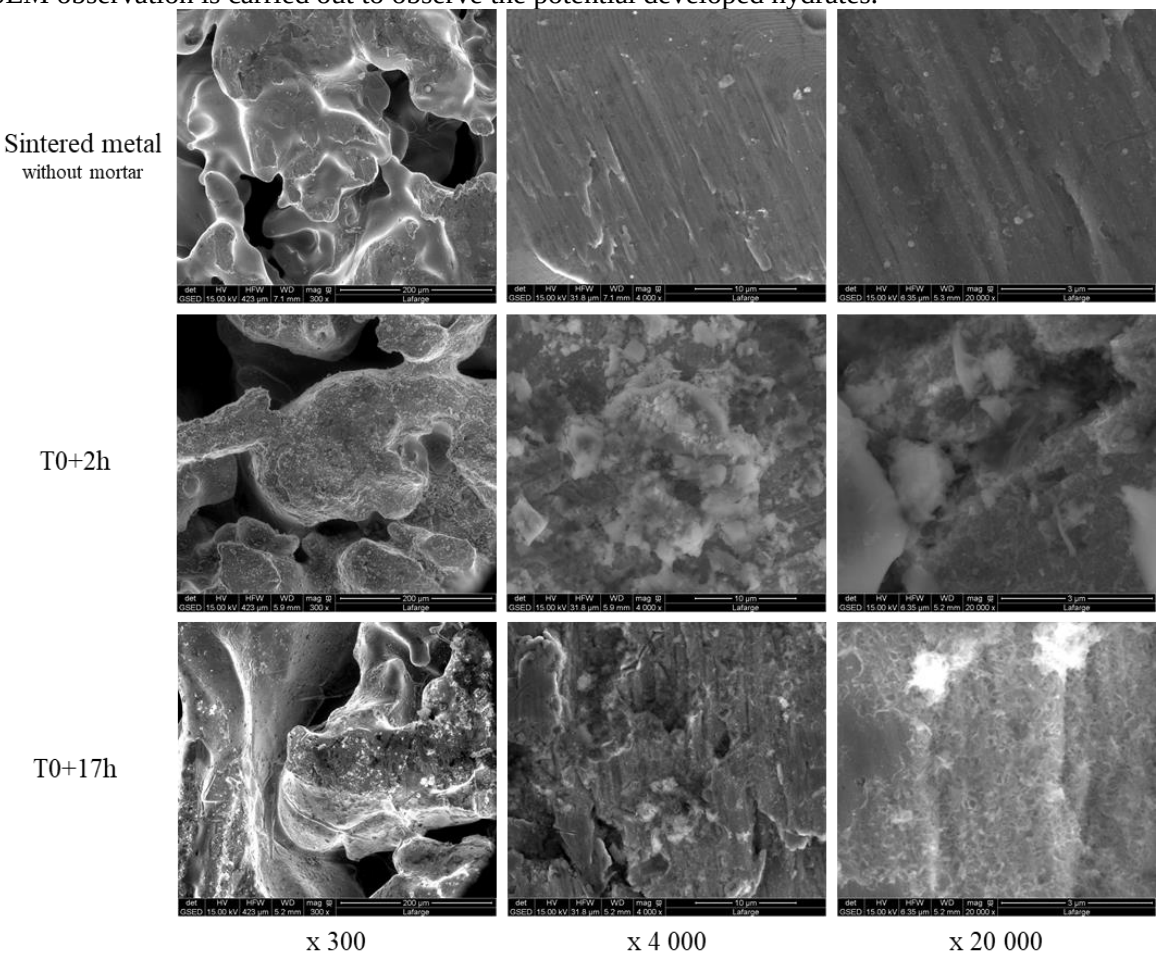

Figure 41. SEM pictures of the sintered metal surface covered with hydrates.

At the top of *Figure 41*, the sintered metal is visible. At 2 hours, the only hydrates expected are a small amount of ettringite. It seems that a water layer is still present and that it is difficult to see a difference between sample at 2 hours and 17 hours. SEM pictures are difficult to analyse because of the non-continuous metallic surface.

Pull-off strength increases (*Figure 38*) at the same time as kinetics of hydration increases described in the first part of the chapter. The pull-off stress resulting of suction phenomena and hydrates adhesion reaches 50kPa. Humidity of the atmosphere before test seems to play a major role. Condensation inside the sintered metal may perturbs the measurement and induces some cement particles washout. To conclude on the effect of adhesion vs suction effect, even if the role of suction has been demonstrated, it would be necessary to change the atmosphere and to developed a new device which could be more adapted to the measurement to avoid these condensation effects.

6. Conclusion of chapter 1

A multi-approaches characterisation of the cement chemical activity is used in this chapter in order to identify the time formation of the hydrates of the reference mix-design (mortar and paste): continuous techniques (conductimetry and NRM relaxometry), and discontinuous techniques with solvent stoppage (crystallography X-ray, DTA and TGA). The conductimetry allows obtaining a general view of the system hydration. Time formation can defer from TGA to DTA for example because of the admixture effect which is different on paste and mortar. The different techniques are complementary.

The main results are:

- the formation of ettringite during the very first stages of hydration;
- there is an increase of the hydration rate around 8 hours which is visible on most techniques;
- then, Portlandite is formed later, after 11 hours of hydration.

The mechanical consequences of cement hydration were studied by monitoring their evolution of adhesion on steel surface and static shear yield stress. It is here shown that the yield stress drop coincides with the peak of hydrates formation and that suction plays a major role in the adhesion mechanisms.

Therefore, it seems important to quantify and predict the development of suction within an hydrating cementitious material in order to predict the interfacial behavior evolution during the cement setting process.

In the following of this research work, other methods are used to characterize volume change due to hydration (autogenous shrinkage and chemical shrinkage), degree of hydration is also determined using calorimetry and pore size evolution is characterized with the mercury intrusion porosimetry. Volumes variations induced by hydration are essential for suction consequences and to estimate the increase of the interfacial friction.

Chapter 2: Origin and modeling of suction

1. Introduction

During concrete and mortar hardening, hydration consumes water and induces several physical phenomena, such as shrinkage or pore water pressure variations. In the slipforming process, the formwork is in contact with concrete at different states of hydration, from the fresh state behavior to the hardened state as described in the global introduction. It is then crucial to quantify solid and fluid volumes variations that will induce internal stress and pressure within the hardening material.

Therefore, the main objective of this chapter is to predict the pore water pressure evolution, responsible for variation in the bulk while concrete is hardening. The influence of air content which may interfere with pressure and volume variation of the mortar is also investigated.

In a first part, the physical background on phase volume variations within early hydrating cement paste is developed: Terzaghi's equation, suction measurements in the literature, contraction due to cement hydration (chemical shrinkage) and measured contraction (autogenous shrinkage). It is important to note that in this study, due to the fact the material is un-exposed (no air desiccation), the drying phenomenon is not considered. The role of entrained air is also discussed as well as the rigidity of the solid network that may hinder chemical contraction. This physical basis helps to define measurements that are required to estimate and understand pore water pressure evolution. Chemical activity measurement (calorimetry), pores and voids distribution, mortar compressibility measurement, chemical and autogenous measurements are therefore presented. In a second part, experimental results obtained on mortars with different air contents are presented before the development of a predictive model linking pore water pressure and volume variation. These models are likely to help describing and understanding the physical phenomena that occur in the bulk and at the interface between a rigid surface (formwork, slipforming, precast) and the hydrating cementitious materials.

2. Physical background

2.1 Terzaghi equation

Terzaghi's theory (Eq.*(5)*) is used to describe the mechanical behavior of the saturated mortar, the effective stress (σ') is the difference between the concrete normal stress (σ) and the water pressure (u_w), Eq.*(5)* and *Figure 42*. The water pressure reduction increases the stress acting between particles because the variation in total pressure is assumed to be negligible compared to the variation of pore water pressure. More details of this equation is developed in *Chapter 4*.

$$\sigma' = \sigma - u_w \tag{5}$$

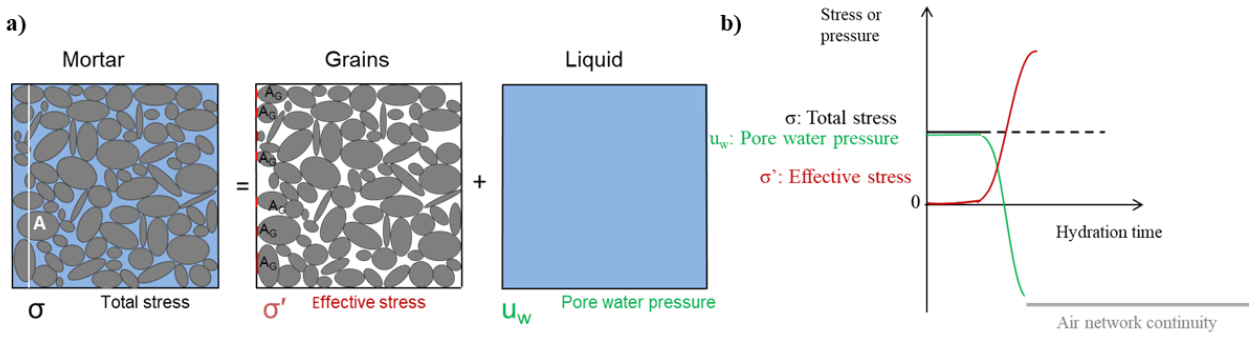

Figure 42. Illustration of Terzaghi's equation. a) Scheme of mortar decomposed with solid and liquid phase. b) Evolution of the stresses of the phases as a function of hydration time.

It has been shown that negative water pressure increases with mortar setting [4]. This evolution induces drastic changes on the mechanical behavior at the interface [34] (adhesiveness, suction, yield stress), and thus the mortar interface properties are modified. Water pressure variations can be considerably larger than the normal stress variations (induced by the weight of the material) recorded during the slipforming operation. Therefore, water pressure variations are mainly responsible for the increase of effective stress and thus the increase of friction [35]. After a while, the percolation of air between the container wall and concrete, due to hydration and concrete solidification, induces the disappearance of suction force. As a result, the friction is drastically reduced [34] [36]. It is important to note that the effective stress transfers shear stress and note the liquid phase.

The following focuses on the pressure of water effect and its origin.

2.2 Negative water pressure effect principle

Before to explain the origin of water suction in concrete, the water pressure phenomenon can be illustrated with *Figure 43* considering a box filled of water. In the first case, removing water without air in an open container induces a reduction of the volume of water. If air content is null, a removal of water can push beyond liquid-vapor equilibrium, forming bubbles: this is cavitation [37]. For the last case, water removal from water with air in a closed container leads to an increase of the air bubbles and a reduction of the global pressure. Similar phenomenon appends during cement hydration, with three phases: solid, air and water. The following chapter deals with those volume changes.

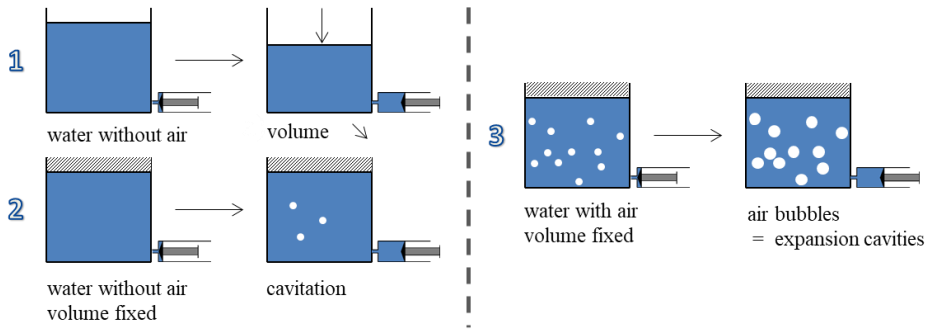

Figure 43. Schematic illustration of volume changes of water with or without air.

2.3 Linking pore pressure to volume and microstructure evolution: objectives of the chapter

At initial time, the three phases of the mortar are solid fraction (cement and sand), water (with in-solution admixtures) and air. Fresh mortar under atmospheric pressure behaves as a dense suspension [38] of inert aggregates and entrained air bubbles which are embedded in a deformable matrix of cement paste [39]. In this fresh state, the behavior of the material is governed by colloidal interactions [40] [41] under a critical sand content as shown by Yammine et al. [42] which is close to 80% the packing fraction. From fresh state to setting time, the total volume reduces because of cement hydration inducing Le Chatelier contraction [43]. Small attractive forces reduce the average distance between particles, and the system becomes flocculated. As the cement hydration continues, the particles are bonded [5] [44] and gradually interlocked (hydrates formation) to finally form a solid structure (a solid skeleton) which can therefore support and transfer high stresses [45] [46]. The air volume remains almost unchanged, until the percolation of the solid contact network (*Figure 44*), corresponding to the "hardened state".

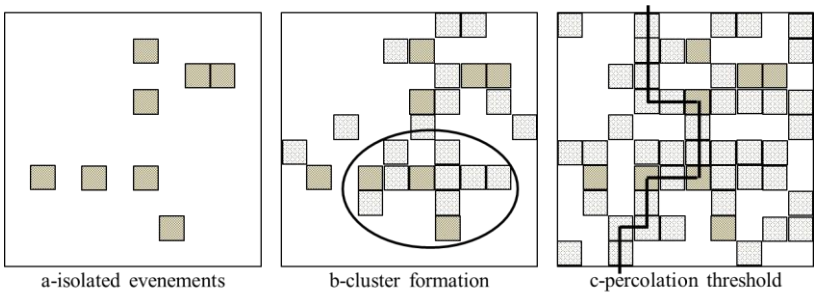

Figure 44. Illustration of the percolation theory adapted from [47]starting from isolated events through cluster formation, ending with percolation threshold

As a result, the apparent volume remains almost constant after this time, although the hydration reaction is not finished [19]. Thereafter, cement still consumes water and creates suction because total deformation is hindered by the solid network rigidity. Hindered volume variations squeeze the particles network and induce negative pore pressure [45] and thermal dilatation or contraction. Therefore, assuming that no exchange occurs with the outside of the sample, air volume (which is not a continuous network at this state) expands to compensate the decrease in volume of the initial components induced by cement hydration. Thus, air is playing the role of expanding cavity, related to self-desiccation [19]. This increase of air volume in a closed system leads to a decrease of its pressure. The difference between air pressure and water pressure in the cement paste porosity, called capillary pressure has also to be taken into account. Considering Laplace-Young equation for capillary pressure [19], the difference between air and water pressure can be calculated regarding the capillary meniscus radius which depends on the pore size (see *section 2.6*). Initially, the radius of curvature of air/liquid interface equals the entrapped air bubbles radius (around 250µm) meaning that the air and liquid pressures are almost equal. However, as water is consumed by cement hydration, the pore initially filled with water becomes partially unsaturated leading to smaller meniscus and increasing the capillary pressure. This means that pore size is also expected to play a major role in pore water pressure evolution and pore size is known to vary with the degree of hydration [48].

In this later stage, continuity of the air network is obtained and therefore the air pressure is equal to the atmospheric pressure and the water pressure is controlled by this meniscus radius.

Looking at the deformation and mechanical behavior of the cement particles network under pressure, consolidation theory from soil mechanics can be applied. The consolidation behavior of fresh

cementitious materials is a key factor that governs water-retaining ability of concrete and therefore its bleeding behavior (homogeneous bleeding as opposed to heterogeneous bleedings as defined in [49] [50]. Moreover, consolidation theory provides a tool able to predict the heterogeneous W/ C profile within formwork. Recent studies have shown that bleeding rate of cement-based materials is controlled by the material permeability and the amount of available free water, which can be computed using concrete compressibility. Both these parameters can be combined to compute the consolidation coefficient, which describes the whole consolidation process [19].

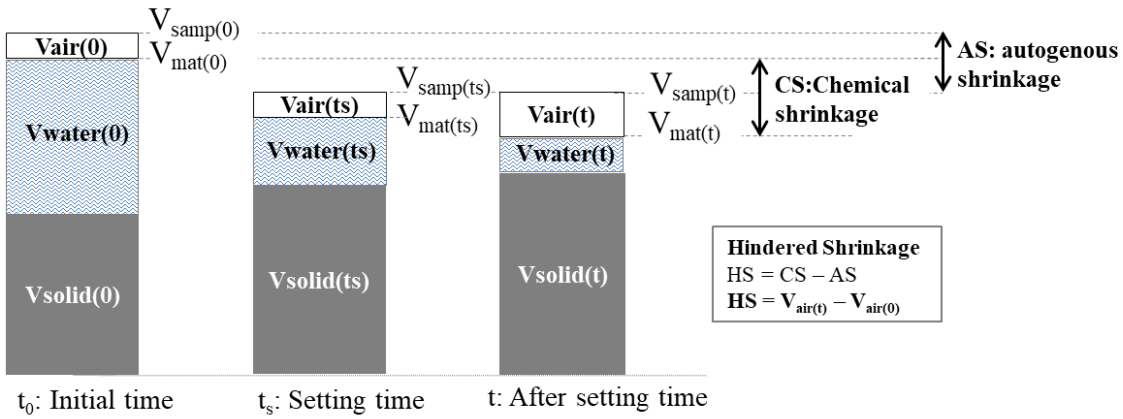

Figure 45. Illustration of volume change highlighting autogenous shrinkage, chemical shrinkage and hindered shrinkage. Sample considered non-air exposed.

To summarize, cement hydration induces a volume reduction of evolving cement-based materials that is usually called shrinkage. Before setting time autogenous shrinkage, which is the total volume deformation of the sample [19], follows the same evolution as chemical shrinkage which represents the loss of volume due to Le Chatelier contraction [43]. After setting, as the rigid network of hydrates is formed, chemical and autogenous shrinkage diverge. This difference -named hindered shrinkage- is compensated by an expansion of the air volume responsible for pore water negative pressure.

Plastic shrinkage and drying shrinkage also occur with cement hydration. Drying shrinkage appears on the surface of hardened concrete in a dry atmosphere whereas plastic shrinkage is the drying of the fresh concrete in dry and windy conditions [15]. In this chapter, they are not considered because the samples are sealed and at early age.

The aim of this chapter is to understand and to model the link between pore water pressure, microstructure evolution and hindered shrinkage at very early age, before air interconnection. As a result, autogenous shrinkage and chemical shrinkage have to be measured separately. This pressure is measured in mix-designs with different air contents which is a key parameter. A prior study consists on calculating the theoretical volume evolution by chemical reaction. This will be compared to the measured contraction.

2.4 Theoretical volume evolution

The theoretical volumes evolution is calculated thanks to the hydration reactions described in *Tables 5 to 7*.

Table 5. Progress table of C_3S formation, volume evolution.

	C_3S	**5.3 H_2O (excess)**	**CSH**	**1.3 CH**
M (g/mol)	228.33	18.02	200.50	74.10
ρ (g/cm^3)	3.12	1.00	2.18	2.24
m (g)	0.6830	0.2317	0.5998	0.2882
n (mol)	0.0030	0.0129	0.0030	0.0039
V (cm^3)	0.2189	0.2317	0.2751	0.1286
Vsum (cm^3)		0.4506		0.4038
Vfinal - V initial (cm^3)				**-0.0469**

Table 6. Progress table of C_2S formation, volume evolution.

	C_2S	**5.3 H_2O (excess)**	**CSH**	**0.3 CH**
M (g/mol)	172.25	18.02	200.50	74.10
ρ (g/cm^3)	3.33	1.00	2.18	2.24
m(g)	0.183	0.0823	0.2130	0.0236
n(mol)	0.0011	0.0046	0.0011	0.0003
V (cm^3)	0.0550	0.0823	0.0977	0.0105
Vsum (cm^3)		0.1373		0.1083
Vfinal - V initial (cm^3)				**-0.0291**

Table 7. Progress table of C_3S formation, volume evolution.

	C_3A	**gypsum limit**	**5.3 H2O (excess)**	**ettringite**
M (g/mol)	172.25	172.18	18.02	1251.00
ρ (g/cm^3)	3.33	2.31	1.00	1.73
m(g)	0.012	0.004	0.0018	0.0291
n(mol)	0.000046	0.00002	0.0001	0.000023
V (cm^3)	0.0036	0.0017	0.0018	0.0168
Vsum (cm^3)			0.0071	0.0168
Vfinal - V initial (cm^3)				**0.0097**

Those calculations are theoretical; chemical reactions are considered separately, without interaction which is not the case in reality. With those considerations, the total volume loss would be of 0.066 cm^3

for an initial volume of cement and stoichiometric water of 0.60cm^3, which means 11% loss of volume. Unfortunately for the mechanical performances, the hydration is never integral and the order of magnitude of the autogenous shrinkage is the percent (at 28 days). It will be showed that this shrinkage is hindered by the mechanical setting. Available water is considered stoichiometric but the W/C ratio of this formulation is 0.30 while 0.32 is needed for the stoichiometry of this specify mix-design. In the literature, composition and density of C-S-H varies, the used equation for C-S-H is here: $C_{1.7}SH_4$.

2.5 Negative pore water pressure measurement

At the very beginning of hydration, a small amount of water is consumed, which induces a contraction of the cement paste (Le Chatelier contraction). A global volume reduction is observed (autogenous shrinkage) as long as its container allows this deformation and as long as the rigidity of the cement paste is low. When the material becomes rigid, a depression is created by this contraction and is compensated by the air bubble size increase or by air entry at a later stage. If volume reduction is not possible (in a waterproof and rigid container), it is expected that the negative pressure occurs sooner than with a soft container (that allows autogenous shrinkage).

Radocea [14] was the first to measure pore water pressure (*Figure 46* and *Figure 47*) but it integrates the evaporation phenomena. He focused on the maximum capillary pressure (the so-called breakthrough pressure), which usually depends on the method of measurement.

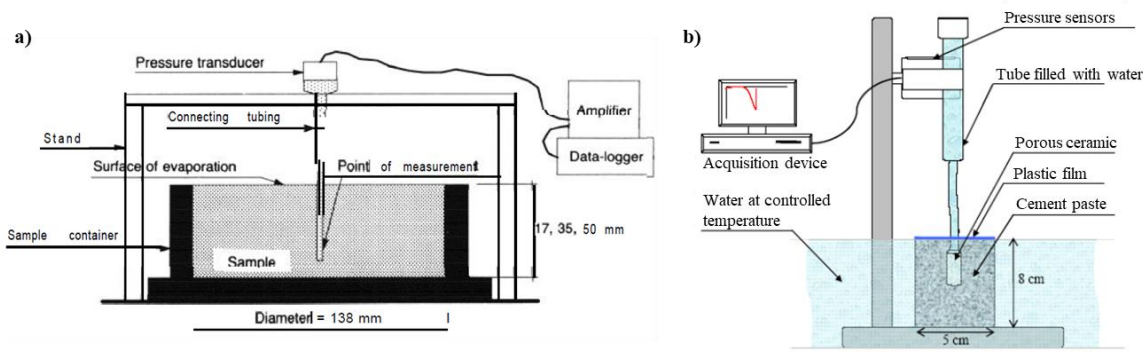

Figure 46. Device for suction measurement a) Radocea[14] b) adapted from [51].

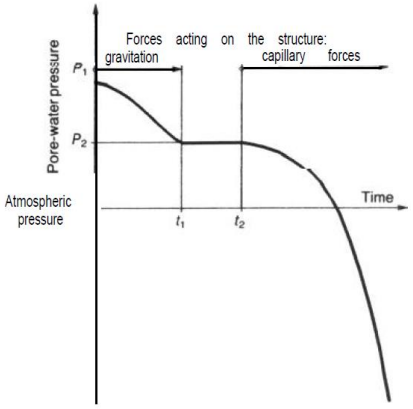

Figure 47. Radocea model of plastic shrinkage: evolution of pore water pressure over time highlighting the gravitation and capillary forces.

Wittmann [45] was able to measure 92mbar negative pressure. Then, the signal was lost at the local sensor. His assumption is that the capillaries of the dispersed system become unstable; the maximum pressure is named “break-through pressure”. Water phase becomes discontinuous. This is a new state for the concrete. Nevertheless, even if the sensor was not able to measure it, the negative pressure still drops. Wittmann [45] showed that plastic shrinkage can be related to the development of pore water pressure. Slowik [52] defined the loss of pore water signal as “air entry value”. Bouasker [51] showed that the beginning of negative pore water pressure corresponds to the end of setting time whereas divergence between chemical shrinkage and autogenous shrinkage appears slightly before. Hammer [34] linked pore water pressure measurements with shrinkage measurements in a sample with drying at the surface (*Figure 48*).

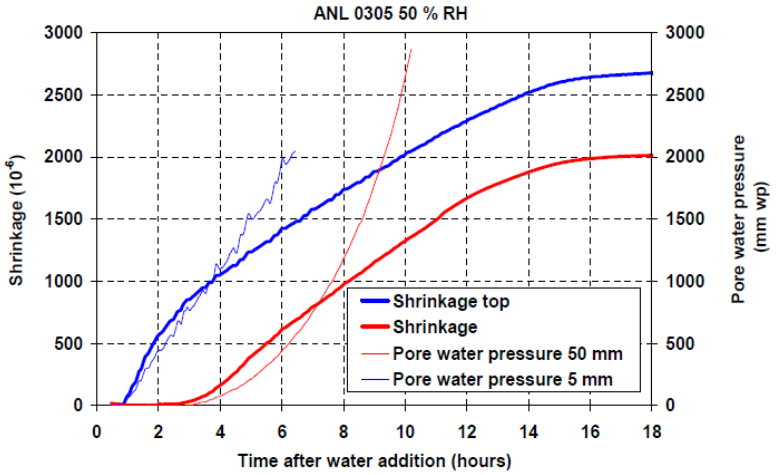

Figure 48. Shrinkage and apparent pore water pressure (1mm water pile corresponds to 0.01 kPa) of concrete with W/B=0.30 and 5%silica fume, at 5mm and 50mm depth, when exposed to air of 20°C and 50% RH [34].

Lourenço et al. [53] used a tensiometer to measure the pore water pressure much longer than “pore entry value” up to close to the cavitation pressure. Toll et al. [54] compared it to direct measurements. They used high suction tensiometers which are fast response time, easy maneuverability. The devices potentially allow direct measurement of suctions up to -2.5MPa.

Suction effect can be modified by different parameters, for example Jensen and Hansen showed that the utilization of superabsorbent polymer can be an internal source of water [55].

2.6 Young-Laplace pressure

The difference of pressure between air and a liquid in a capillary (*Figure 49*) is described with Young-Laplace equation at the interface (Eq.(6)). Thus, depending on the size of the meniscus, this pressure has to be taken into account.

$$P_g - P_l = \frac{4\,\gamma}{D}.\cos\theta \tag{6}$$

with P_g the gas pressure, P_l the liquid pressure, D (=2r), the meniscus diameter and γ the liquid surface tension, θ the contact angle between liquid, air and solid.

And, the hydrostatic pressure above the meniscus is defined in Eq.(7).

$$P_l = P_g - \rho g h \tag{7}$$

This leads to the Jurin law, Eq.(8).

$$h = \frac{4\,\gamma \cos\theta}{D.\rho.g} \tag{8}$$

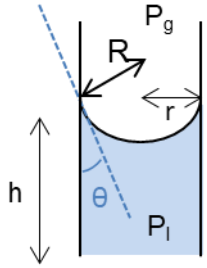

Figure 49. Illustration of a capillary tube, P_g is the gas pressure, P_l is the liquid pressure, h the height of the liquid in the capillary.

The desaturation of pores always begins by the larger pore to the smaller pores as illustrated on *Figure 50*. The desaturation of the pores allows to trace the saturation curve which is represented into format on *Figure 50.a and b* [56].

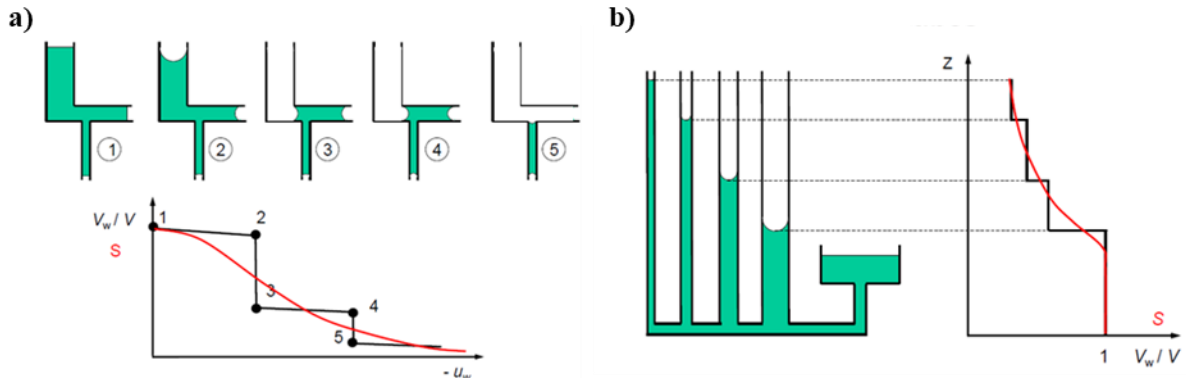

Figure 50. Representation of a) water retention of a system of capillary tubes b) increasing water tension in a system of capillary tubes [56].

Figure 51 shows the different states of the water retention curve [56]. In the saturated state, air is dissolved in water (S=1, u_w < 0). During quasi-saturated state, gas phase is discontinuous and liquid phase is continuous (0.85-0.90<S<1, u_w<0). The partially saturated state corresponds to the continuity of both gas phase and liquid phase (0-0.1<S<0.85-0.90, u_w<0). The residual state is defined when gas phase is continuous and liquid phase is discontinuous (S<0-0.1, u_w<0).

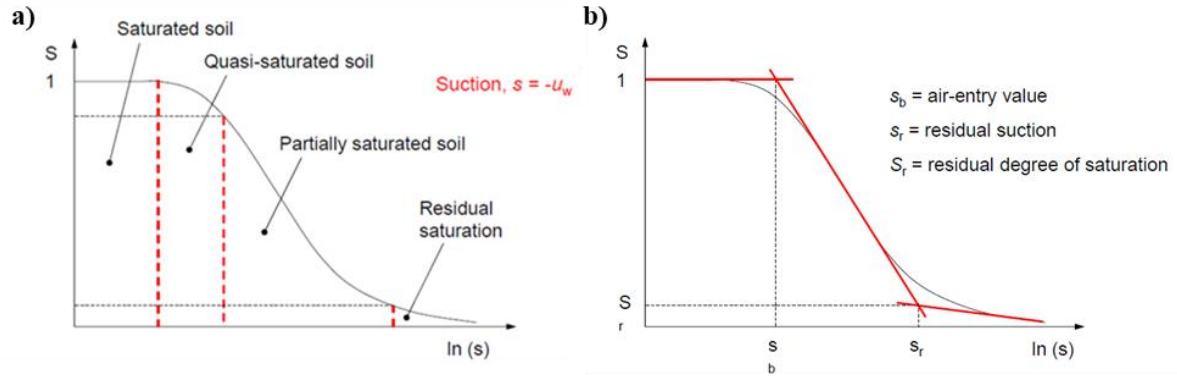

Figure 51. Retention curve a) Different state, air pressure considered null b) Retention curve parameters [56].

Drying has an impact on pore water pressure, this is why it is important to precise the conditions of each measurement. In this research work, the drying is not major because most of samples are sealed or with a small surface compared to the bulk volume. A lot of the volume change occurs before the air entry value as this is the case for soil materials and also for cement-based materials [56].

3. Experimental procedures

3.1 Mixing procedures and materials

The mortar described in *Chapter 1* is used for the study. The hydration enthalpies of the cement are summarized in *Table 8*.

Table 8. Theoretical hydration enthalpy calculation on the reference mortar mix-design.

Phase	Cement phases Percentages	Pure phases hydration enthalpy (J/g)	Theoretical phases hydration enthalpy inside the mix (J/g)
Alite	68.3	517	353
Belite	18.3	262	48
Ferrite	7.1	725	51
Aluminate	1.2	1453	17
		TOTAL	**470 J/gcement**

In the fresh state, the reference mortar is fluid (spreading diameter is 260 mm with a minicone - 60 mm in height, 70mm in smaller diameter and 100mm in higher diameter). The reference mix-design has air content close to 3%. Several air contents are tested: 0%, 10% and 20%. 0%-air-content is obtained using an anti-foaming agent and putting the sample under pressure. 10 and 20%-air-contents are obtained by using air entraining agent.

3.2 Physical parameters

a) Surface tension

Surface tension measurements are conveyed with a Wilhelmy plate. The plate is oriented perpendicularly to the surface. Special care is required during the cleaning of the different surfaces

(first with ethanol and then under a flame). The platinum plate is introduced inside the liquid phase and then removed, the force acting on the plate is measured with the automatic 3S-tensiometer (*Figure 52*).

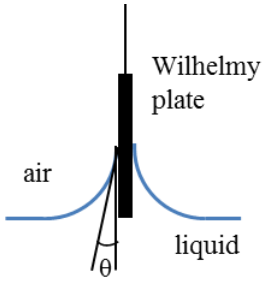

Figure 52. Scheme of the Wilhelmy plate of a tensiometer pulled-off from liquid surface for surface tension measurement.

b) Air content measurement and size distribution

Air content is measured indirectly by density and verified using air meter for concrete on fresh mortar. The bubble size distribution is determined using a Sartorius® Air Void Analyzer (AVA), stirring 200mL of mortar in glycerin phase. Due to its specific viscosity and hydrophilic character, the bubbles released from the mortar keep their original size and neither coalesces nor disintegrates into smaller bubbles. Above the glycerin phase, a column of water allows the air bubble to rise. Larger bubbles rise faster than smaller bubbles and a Stoke's law-based-algorithm allows to compute the bubbles size distribution from the mass evolution of the samples.

c) Porosimetry analysis

Different techniques can be used in order to determine the pore size distribution of materials and precisely cement-based materials. These techniques and their advantages are summarized in *Table 9*.

Table 9. Summary of the major technics used for porosity determination, comparison of the sample size, advantages and disadvantages of the considered technic.

Method	Capacity	Advantages	Disadvantages
MIP	5 nm to 500µm	Large range of measurements	Mercury is carcinogenic, mutagenic, reprotoxic
Isothermal sorption	1 to 100nm	Data variety	Expensive
Thermal porosimetry cryoporosimetry	1 to 100nm	Fast, no drying	Destructive method, big sample
Small angle diffusion	1 nm to 1µm	Hypothesis shapes of the pores	Expensive
2D imaging	1 nm to mm	Exact shape of the pores, connectivity	Resolution limitation
Tomography, 3D imaging	500µm3 volume for 50nm resolution	Exact shape of the pores	Resolution limitation

The different pore classes are defined from pore size; the major classes are summarized in *Figure 53*.

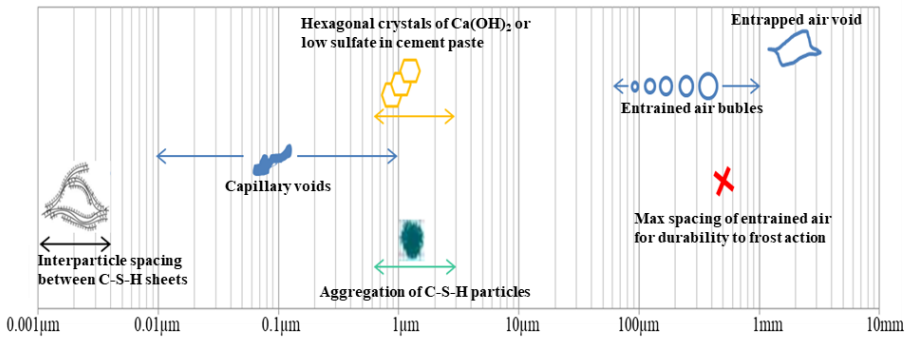

Figure 53. Size pore definitions from Mehta and Monteiro [57] of the elements of hydrated mortar or concrete.

Those definitions of class size are discussed in the literature as shown in *Figure 54*.

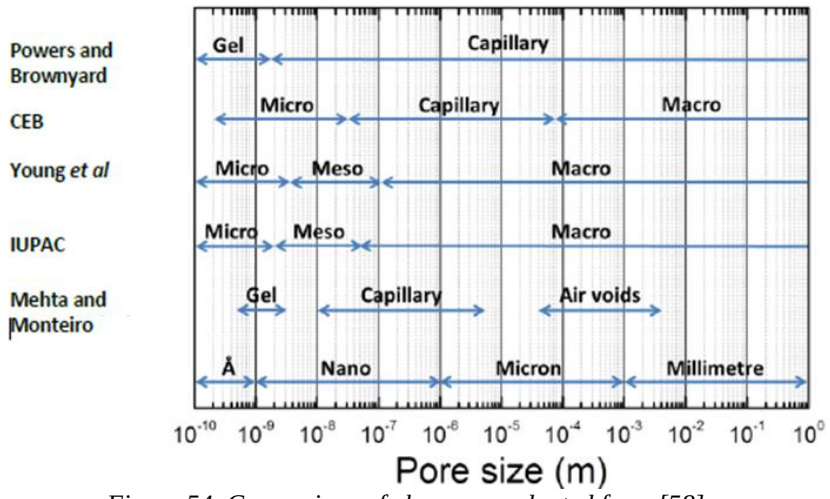

Figure 54. Comparison of class pore adapted from [58].

Powers model describes the evolution of volume fraction for CEM I. In this model, the microstructure is divided in two classes. The bigger pores, as capillaries pores, they are from inter-particular spaces of the paste initially filled of water. The second class corresponds of the pores created with hydration, inside the hydrates as illustrated on *Figure 55*.

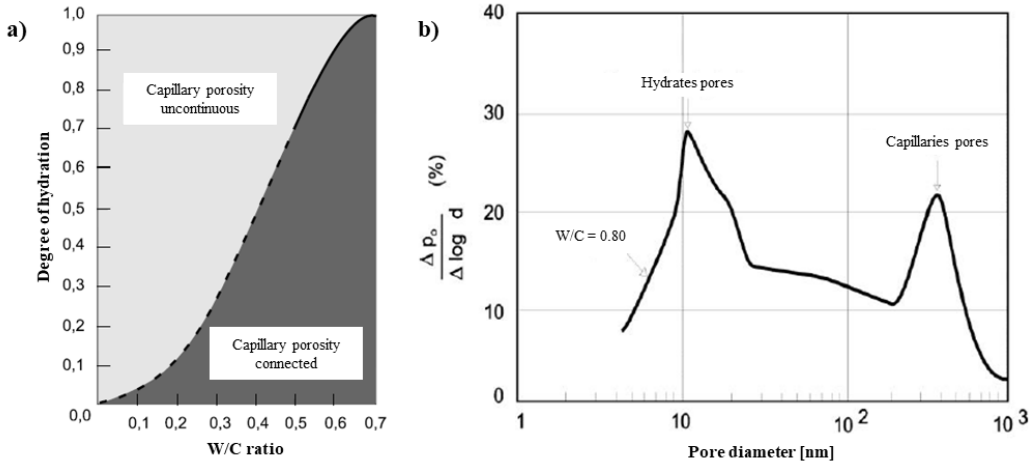

Figure 55. a) Influence of W/C ratio and degree of hydration on the continuity of capillaries adapted from Powers [59]; b)Evidence of the two classes of pores defined by Powers and illustrated by MIP by Verbeck et al. (adapted by [60]).

Powers and Brownyard [61] divided the water within the cement paste into non-evaporable and evaporable water. Non-evaporable water is considered the one that remains in paste at the pressure below 6.7 10^{-3} Pa at 23°C.

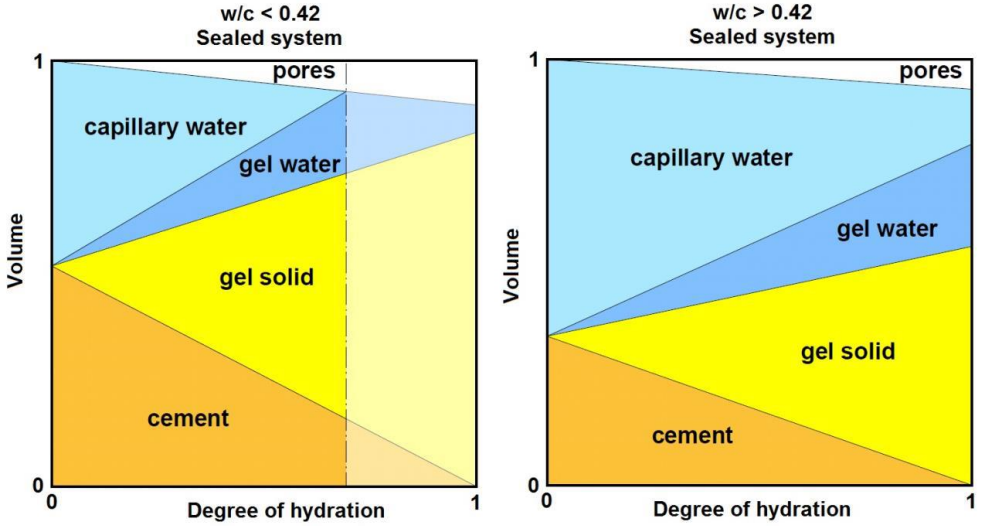

Figure 56. Water distribution evolution with degree of hydration [61], comparing at the left W/C smaller than 0.42 and on the right higher than 0.42.

Mercury Intrusion Porosimetry (MIP) is used to characterize the pore size distribution (PSD) evolution during the early hydration of the mortar samples. It is measured with the device Autopore IV 9520 from Micromeritics.

Mercury Intrusion Porosimetry (MIP) uses mercury properties in order to determine pore size distribution. Mercury is a non-wetting fluid with negative contact angle as illustrated on *Figure 57*.

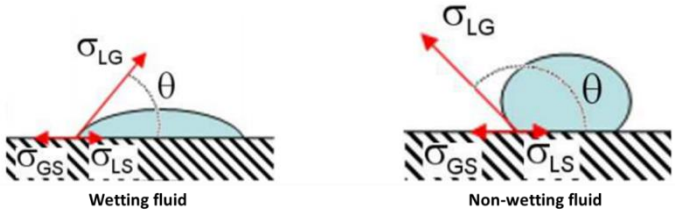

Figure 57. Illustration of contact angle of wetting on a plane surface [62].

Low pressure is used for mercury to get inside macropores; a higher pressure is needed to get inside smaller pores. Pore size distribution can be obtained from 4nm (under 400MPa) to around 800µm (under vacuum) [63]. Before the analysis, the sample is placed inside a vacuum chamber to eliminate humidity inside the sample. Then, mercury is introduced inside opened pores; Washburn equation (Eq.(9)) describes the correlation between pore diameter and the applied pressure.

$$D = -(1/P).4.\gamma.cos\theta \quad (9)$$

with D = pore diameter, P = applied pressure, Υ = mercury surface tension, Θ = mercury contact angle (130°)

Before Mercury Intrusion Porosimetry acquisition, samples are stopped in an oven at 105°C for 40 minutes. For the present study, the device is a Micromeritics porosimeter that applies pressures from 0 to 345kPa with a resolution of 69Pa. Then diameters of 360µm to 3.6µm are reached. It is a destructive method. At the end of the experiment, the pressure is increased up to 414MPa, to assess pore diameter down to 3nm. Pore diameter is calculated from Eq.(9), using a surface tension of 0.485N/m and a contact angle of 130°. The pore size distribution is analyzed assuming each individual pore class follows a normal distribution of the log10 of pore entry diameter. A pore class is characterized by its mean, standard deviation and relative volumetric abundance. The choice of two pore classes for MIP fitting (*Figure 58*) enables minimizing the Bayesian Information Criterion (BIC) value, by balancing residue against number of parameters [64].

A third class of pore is attributed to the air bubble analysis by AVA. Intruded volume corresponding to pore entry radius larger than 100µm is not considered in the minimization.

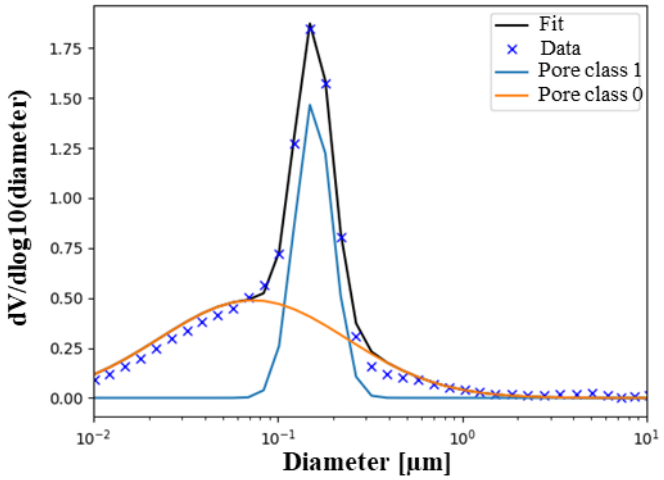

Figure 58. Example of 2 normal probability distribution functions that best represent MIP experimental data. y axis: dV/dlog(d) [1/log [m]], where V is the intruded mercury volume and d is the pore entry diameter.

3.3 Hydration study and chemical parameters

Cement hydration, which is at the origin of the volume deformation is characterized: the degree of hydration is calculated with calorimetry measurements. Then, volume evolution of the different phases is estimated with thermodynamic calculations to complete theoretical volume calculation and measurements.

a) Degree of hydration

Calorimetry measurement is used in order to follow the heat transfer of the sample and to analyze the hydration degree in continue [65].

The samples are introduced inside a tare cell, then sealed and introduced inside the calorimeter. Heat transfer is measured over time. The samples weight is around 5 grams. The samples are inserted inside a quasi-adiabatic chamber. For the manipulation, it is important that there is no material on the walls of the container because this weight would be taken into account but due to the place of the thermometer, its heat transfer will not be taken into account, this will reduce the accuracy of the measure.

The degree of hydration is defined as the ratio of heat transfer and total theoretical hydration heat transfer. Heat flow from hydrated cement is corrected by taking into account linked-water quantity. The standard deviation of the measure is around 8J/g, this means that the method is accurate if it is well calibrated. Calorimetry is used to follow the heat release of the sample and to deduce the evolution of the degree of hydration [65] [66]. The latter is an important parameter because hydration controls both the pore water pressure and the setting time.

The cumulated heat flow is the sum of the surface under the curve between two measurements. The surface under two points A and B of measurement of heat flow F [mW/g] as a function of the time t [s] is given by [37], Eq.(10).

$$surface = (t_B - t_A) * \left(F_A + \frac{F_B - F_A}{2}\right) \quad (10)$$

with t is the time of the point [s] F is the instantaneous heat flow [W/g]

The cumulated heat flow [J/g] is obtained by integrating the heat flow [W/g] with the time [67]. For the data treatment, the final heat value has been used as baseline which is a simplification because the wetting heat is not taken into account.

The pressure variation is considered negligible (the chamber is consequent), with the heat capacity of each component it is possible to evaluate the reaction enthalpy. It is important to keep in mind that the transfer is controlled by the climatic chamber at 25°C. Heat emission or absorption from the sample is compensated in order to have a constant temperature of the chamber, and then the flux is measured [68]. Tam air calorimeter is used to measure heat flux for cement hydration. It is composed of a thermostatic isotherm chamber with height calorimetric cells (sample + reference: usually an old cement paste). Thermic regulation is done with a Peltier system (external thermostatic bath).

b) Thermodynamic calculations

The phase assemblage, i.e. the relative volume fraction of each phase, is calculated as a function of system composition and degree of hydration at a constant system volume and temperature. The total volume consists of unreacted constituents (anhydrous cement and sand), reactive constituent at equilibrium (hydrates and water) and air to complete the volume balance. The system speciation at equilibrium i.e. hydrates and water mole amount is calculated with PhreeqC and therefore relies on thermodynamic database in the PhreeqC format [64] for species equilibrium constant (i.e. LogK values). It also relies on a database of species molar volumes and enthalpies of formation in addition to constituent specific density in order to evaluate phase volume fraction, chemical shrinkage, porosity and enthalpy of reaction. The species logK values come from the Thermoddem 2011 database [69] exported in PhreeqC format. The other thermodynamic data (molar volumes and enthalpies) are also coming from the Thermoddem 2011 database. The minerals considered in the calculation of equilibrium phase assemblage are: Portlandite, C-S-H (1.6), Monocarboaluminate, Monosulfoaluminate, Ettringite, Hydrocalcite, Goethite in additions to minerals present in the cement (see *section 3.1*).

3.4 Stress and volume evolution

At a larger scale, the volume of consumed water is evaluated through chemical measurements and the total volume of the sample is evaluated through hydrostatic weighting (autogenous shrinkage). Those volume deformations induce stress evolution on the sample which is quantified with compressibility measurements (odometric characterization). Finally, pore water pressure is measured to confirm the predictions.

a) Chemical shrinkage measurement

Different techniques could be used for chemical shrinkage measurements as dilatometry for example, by manual lecture. Here, chemical shrinkage is measured by continuous hydrostatic weighing in a oil thermo regulated bath at 20°C. The mortar sample (around 5g) is placed in an open pycnometer allowing the external water source to penetrate inside the sample. The sample is de-aerated and placed in a pycnometer just after mixing. The sample weigh is measured over time using Buoyancy principle as shown in *Figure 59*; the balance accuracy used for the study is 0.001g.

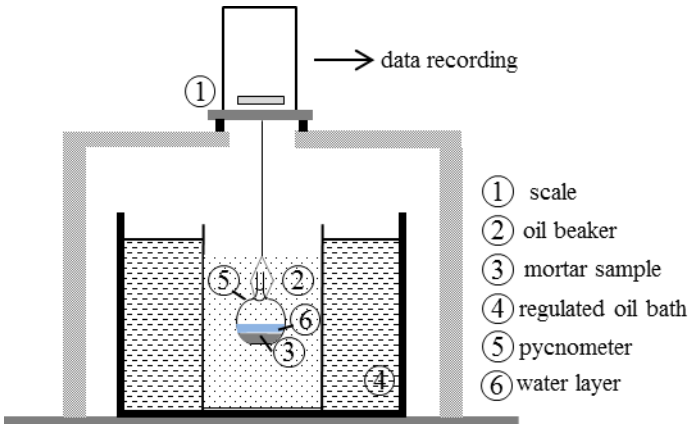

Figure 59. Scheme of chemical shrinkage measurement system measured in continuous by hydrostatic measurement.

It has been shown by Justnes et al. [70] that there is no influence of W/C ratio on chemical shrinkage for the same degree of hydration. Boivin [19] confirmed these results. Baroghel-Bouny et al. [48] confirmed that if W/C is higher than the stoichiometric ratio of the hydration reaction the amount of $Ca(OH)_2$ produced at a given age is not influenced by W/C. Geiker [58] showed the major influence of sample size, especially the sample thickness in order to allow water to go inside the pores.

b) Autogenous shrinkage measurement

For autogenous shrinkage, the measurement implies no exchange between the sample and the surrounding liquid. The only existing standard test to measure autogenous shrinkage is described in ASTM C827. It consists in measuring manually the vertical displacement on a steel ball placed on the surface of fresh concrete [71]. This method is limited, due to the fact that only vertical displacement is measured, which is primarily a function of settlement, especially at very early age. Then in the present study, the autogenous shrinkage is measured by volume deformation, even if some authors have shown that the correlation between linear deformation and deformable volume is not always direct [19] [72] [73]. These studies have also shown that latex membranes are not completely waterproof, but in our case, the effect of membrane during first hours seems to be negligible and does not explain the difference between linear and volume measurements. Furthermore, [74] has shown that at early age linear and volume deformation are well correlated (*Figure 60*). Another advantage of volume measurement is that it avoids bias due to friction between the sample and the mold [75].

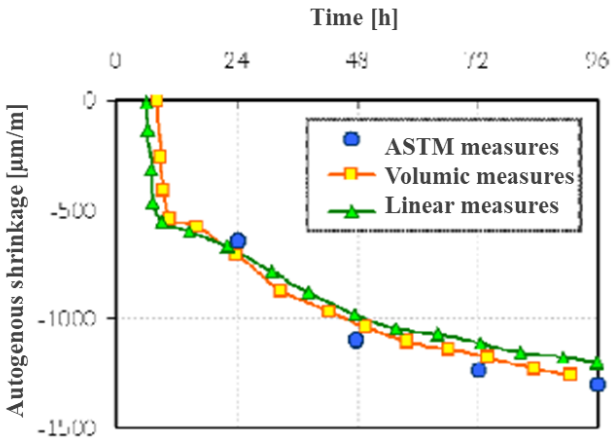

Figure 60. Comparison of ASTM, volumetric and linear methods for autogenous shrinkage measurement (adapted from [74]).

The autogenous shrinkage kinetics increases with low W/C ratios [72] which is expected because the degree of hydration is higher. When the humidity of the sample decreases, there can be self-desiccation which is a transfer of liquid water to vapor phase.

Three dimensional and continuous measurement is used: autogenous shrinkage is measured in a latex membrane allowing free deformation in all directions [19]. One mortar sample of about 100 grams is placed in the deformable membrane. Air at the top of the membrane is removed carefully in order to avoid increasing the bulk air volume and therefore perturbing the measurement accuracy. The sample is isolated from liquid exchange (contrary to chemical shrinkage measurement) and placed in a regulated bath at 20°C. The material-filled membrane is completely submerged in water and the weigh is measured over time thanks to continuous data recording by hydrostatic weighing (*Figure 61*). The data recording starts 50 minutes after mixing to capture the early age hydration. Each measurement is

repeated twice. The sample volume can be easily computed from the recorded mass variation over time.

Mounanga et al. [7] developed a device to measure autogenous shrinkage by adjusting the bath temperature to the temperature of the sample. This approach is relevant but in our study, measurements are carried out in a 20°C bath in order to use the results as a reference. In the present study, the evolution of the temperature and pore water pressure variations are measured in a separated container because direct pore water pressure measurement can perturb the shrinkage measurement.

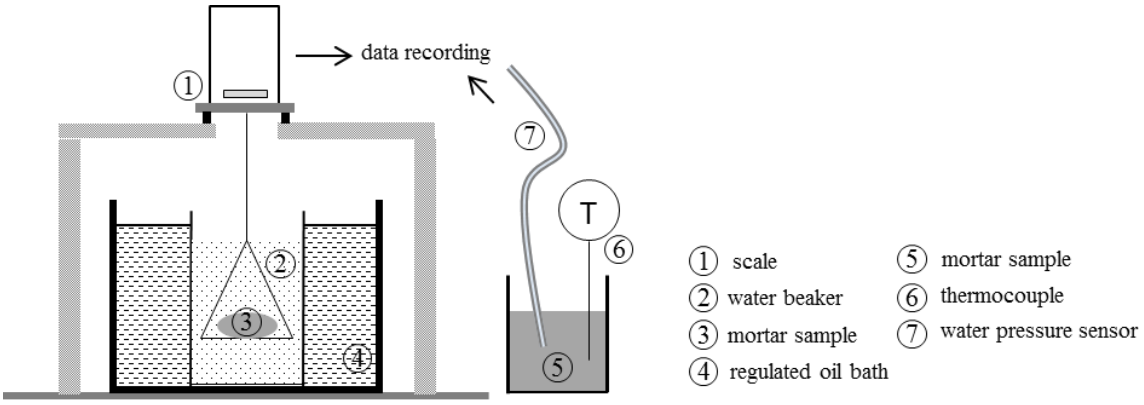

Figure 61. Scheme of autogenous shrinkage measurement system measured with hydrostatic weighting on the mortar scale.

c) Compressibility measurement

Compressibility measurements are performed using a constant rate of loading odometer (confined one-dimensional compression cell). The device used in this study is similar to the one used in Rangeard et al. [76] and Perrot et al. work [77]. The 20mm high-sample diameter is 50mm. A vertical total stress is applied to the sample while the pore pressure is recorded at the bottom of the cell. An increasing total stress ramp is applied on the sample (from 0 to 400kPa in 400 seconds). The simultaneous measurement of total stress and pore pressure allows to compute the effective stress using the Terzaghi's equation: effective stress is the difference between total stress and pore pressure.

The compressibility coefficient λ is defined as the slope of the plot between the logarithm of effective stress σ' acting on solid particles network [77] and void ratio e (ratio of fluid and air volume over solid volume) (Eq.(11)).

$$\lambda = d\log(e)/d\log(\sigma') \quad (11)$$

The compressibility coefficient [78] allows estimating the variation of the solid particles network under a given stress.

In this theory, the rigidity of the particles network of the mortar ($d\sigma'/dV$, with V, the volume deformation) can be computed from the local slope ($de/d(\log(\sigma'))$). Therefore, the particles network becomes more rigid when the mortar consolidates (lower void ratio, higher effective stress).

Tests are performed at different mortars hydration ages ranging from 2 to 10 hours in order to estimate the variation in the granular skeleton compressibility over time.

3.5 Pore water pressure sensor

Special care is taken for the followings terms: **pore water pressure** is the pressure of water inside the pores formed by the solid particles and hydrates whereas **capillary pressure** is defined as the difference between the gas phase and liquid phase at the interface of a meniscus, which depends on the Young Laplace law.

Pore water pressure is measured in a metallic cylinder placed in a regulated air atmosphere at 20°C +/- 1°C. A plastic tube (diameter of 1.5mm) is placed inside the mortar sample. The tube is filled with de-aerated water (warm water de-aerated with water vacuum pump). This tube is connected to a pressure sensor, consisting in a deformable membrane fitted with strain gauges, allowing to calculate the pressure value (positive and negative pressures up to 1bar).

4. Experimental results

4.1 Physical parameters

a) Surface tension

Interstitial liquid of the mortar after mixing is extracted thanks to centrifugation. Surface tension of the water with non-absorbed polymer is measured. The mean value of six measurements is γ = 57.2mN.m^{-1} (standard deviation 0.2) which is rather lower than pure water γ = 72.8mN.m^{-1}.

b) Air bubble size distribution

At initial time, air bubble size distribution (*Figure 62*) is characterized for the different air contents. Each data point is the average of two measurements.

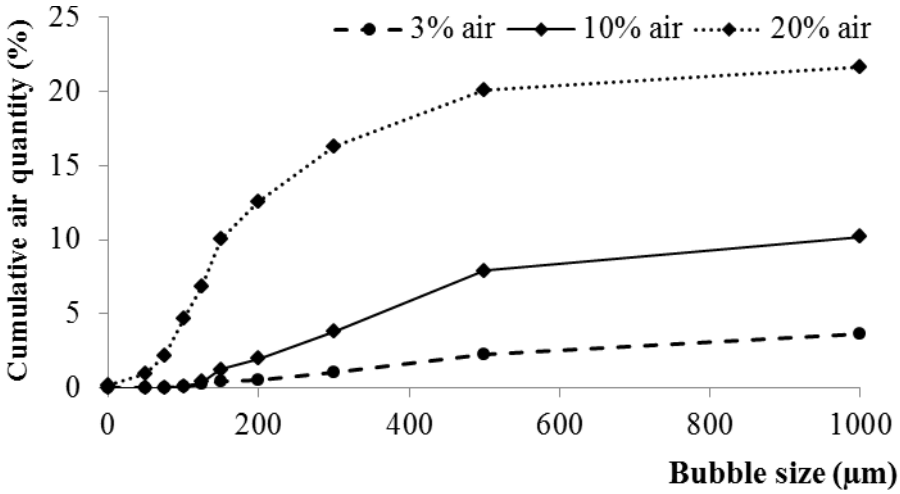

Figure 62. Air bubble size distribution at initial time, comparison of the mortar mix-design with3, 10 and 20% of air content.

Air void analyzer is not sensitive enough to measure air bubbles size distribution in mix-designs with almost 0% air content. It is observable that the size of the bubbles at initial time is mainly over 200µm for 3% and 10% mix-design, this data is compared later to the size of the pores during microstructural build-up.

c) Pore size distribution

Mercury Intrusion Porosimetry and the thermodynamic tool allow plotting maximal pore diameter filled as a function of hydration time (*Table 10*). Generally, three diameters categories are defined, d0 is the smaller diameter, d1 the second categories of pores and d2 the diameter of air fraction (not presented in the table).

Table 10. Pore diameters size evolution as a function of time for the four sample analyzed with MIP.

Hydration time [h]	First size meniscus diameter d0 [µm]	Second size meniscus diameter d1 [µm]	Volume fraction corresponding to d0 [-]	Volume fraction corresponding to d1 [-]	Total porosity
0	1.36	3.31	0.5	0.5	0.26
6	0.49	2.01	0.6	0.4	0.26
14	0.07	0.16	0.6	0.4	0.20
24	0.06	0.08	0.5	0.5	0.16

The volume fraction of the two diameters has small evolutions but the pore diameter decreases simultaneously with the total porosity.

4.2 Chemical parameters

a) Degree of hydration

Calorimetry is conducted on mortar, paste and mortar without the adjuvant. The aim of this measurement is to compare the hydration time of those different formula. For mortar and paste sample, the analysis is carried out on two sampling of the same mix-design. Without the adjuvant, the mixing is difficult, in order to be sure of the homogeneity of the sample, 4 sampling of the same mixing are analyzed. For each formula, the amount of cement inside the sample is noticed inside the software which gives directly the heat transfer power per gram of cement. The calorimetric curves of the samples are plotted on *Figure 63*.

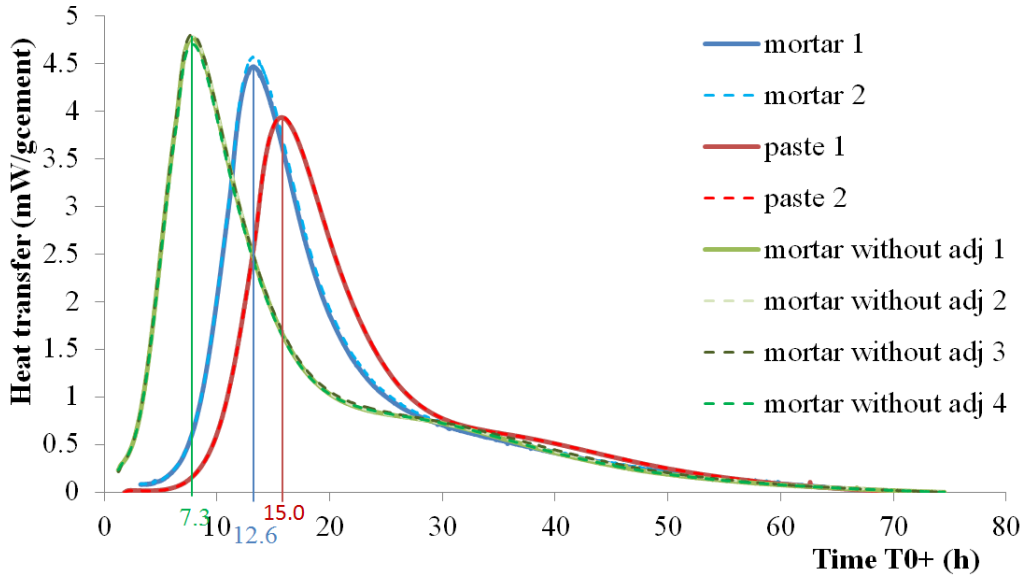

Figure 63. Comparison of calorimetry on paste, mortar and mortar without admixture (adj).

On the graph, the reproducibility test of the sampling is represented with a dash curve. At first, one can see that there is a difference on time on the maximum pick: the mortar without the admixture is faster; it has its maximal pick at 7.3 hours, followed by the normal mortar at 12.6 hours and the paste at 15 hours. These shifts are mainly explainable with the admixture effect. The adjuvant delays the setting because of its covering property and deflocculating effects (it explains the difference between 7.3 and 12.6 hours). The paste is more delayed than the mortar because the adjuvant quantity compared to the cement is higher: the sand absorbs a part of the admixture so there is less adjuvant available in order to deflocculate the cement. Moreover, sand will abrade the cement grains, the surfaces will be more accessible and this will accelerate hydration.

The first part of the curve: the wetting pic, has been removed in order to have the same starting point for the cumulative curve. There is a difference of temperature between the components, the mixing and the calorimeter. By removing the first part of the curve, the difference is not taken into account. Although, the heat transfer is not completely representative because a part of the heat elevation is removed.

The total theoretical enthalpy of the hydrates, ΔHr is assumed as 449J/g considering cement composition and the hydrates formation enthalpy from the literature [67]. Degree of hydration is plotted on *Figure 64*.

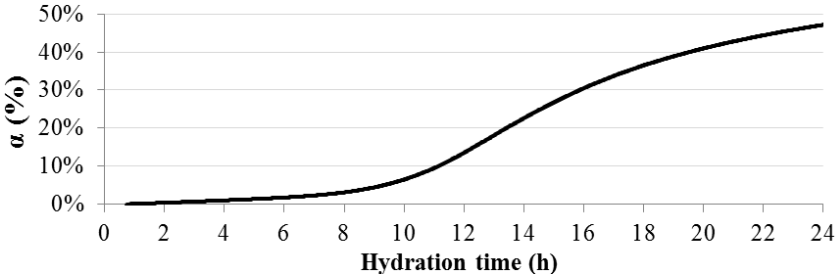

Figure 64. Degree of hydration of reference mortar as a function of time (after cement/water contact).

Cement's hydration kinetics is slow during the first 10 hours, and then it accelerates until 20 hours, reaching 47% of hydration at 24 hours. The degree of hydration is essential for the study because it shows when the maximum water consumption occurs. *Figure 12* summarizes the effect of admixtures on hydration kinetics.

Table 11. Influence of admixture on hydration time with the influence of air.

Mix-design	Moment of maximal hydration heat [h]
0% air (antifoam)	12.8
3% air (reference)	13.0
20% air (air entraining agent)	14.5

b) Volume evolution thermodynamic prediction

Thermodynamic prediction allows obtaining the evolution of each phase as a function of the degree of hydration (*Figure 65*).

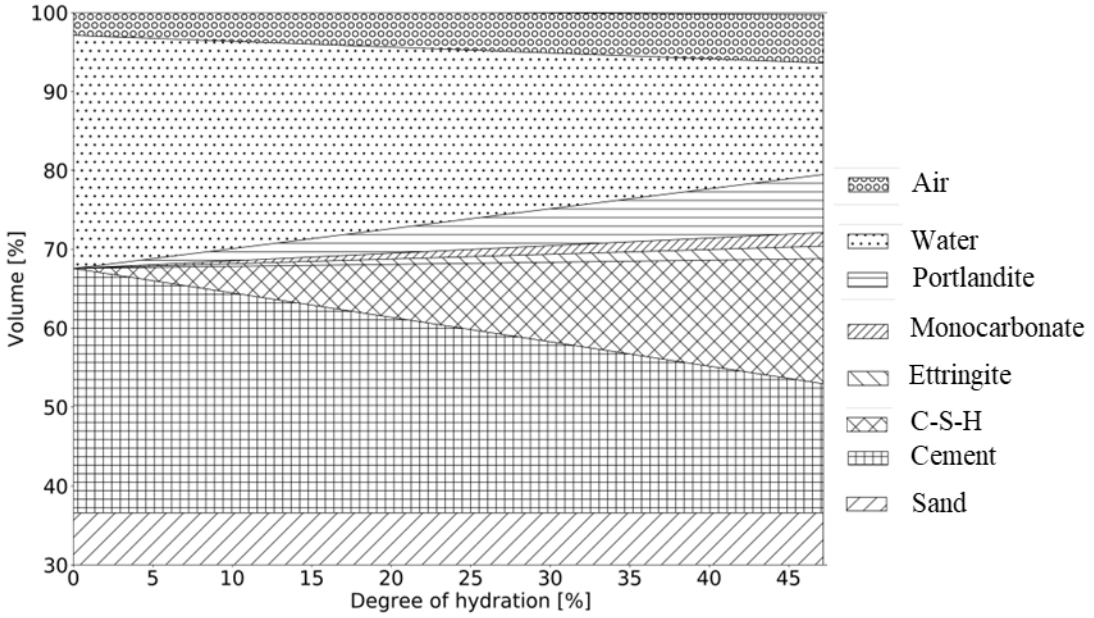

Figure 65. Volume phase evolution from thermodynamic calculation using degree of hydration from calorimetry as input. The lower volume fraction corresponds to the aggregate (37v%).

4.3 Stress and volume evolution

a) Analysis of measured shrinkage

Continuous evolution of autogenous shrinkage is observable on *Figure 66*. The volume variations are normalized by the volume of each sample. Variability is less than 5% and an average curve of two measurements is plotted.

The measured volume variations are consistent with the results observed in literature [34]: the higher the air content, the lower the autogenous shrinkage. This trend was expected because air

bubbles play a role of expansion cavities into the mixture, so the apparent volume deformation is higher with a lower air volume.

As highlighted by Loukili et al. [79] and Bjontegaard et al. [38] it is important to verify that the volume differences that are observed are not affected by the thermal expansion. In this study, this thermal expansion is evaluated by changing the bath temperature by 5°C. The observed gap on autogenous shrinkage is 0.1%. Thus, air and water thermal expansion are minimal compared to the variation of autogenous shrinkage. Therefore, thermal effects are neglected in this study.

Autogenous and chemical shrinkage measurements are plotted and compared (*Figure 66*). Chemical shrinkage is measured on a de-aerated mortar sample, and then rescaled with the initial volume of air.

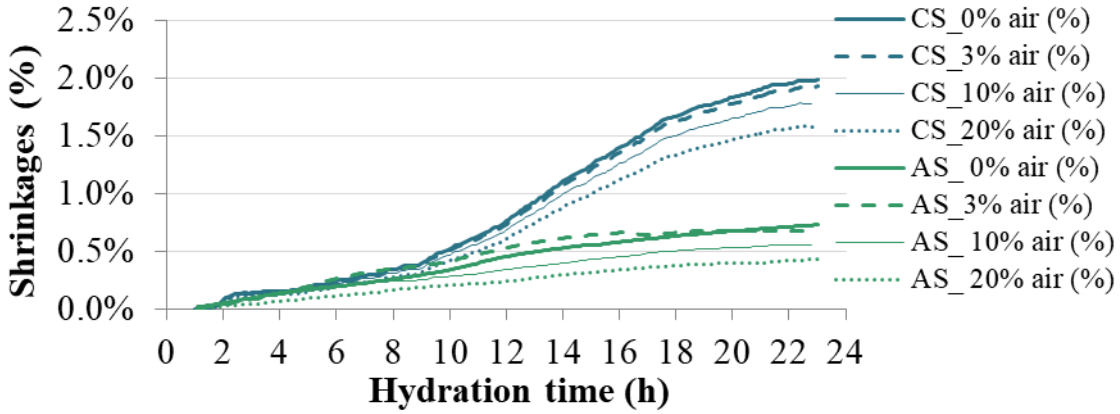

Figure 66. Autogenous and chemical shrinkage measurement comparison as a function of hydration time with different air content.

The chemical shrinkage variations are comparable with the order of magnitude observed in literature [80] [81]. Initial offset is corrected.

Chemical shrinkage and autogenous shrinkage seem to evolve similarly during the first hours of hydration until 7 hours. This moment corresponds to the increase of cement hydration rate that drastically increases the solid percolation and network rigidity. After this rigidification, autogenous shrinkage curves have small variations because the volume is almost fixed (the variation is limited by the compressibility of the solid skeleton) meanwhile hydration continues and chemical shrinkage increases until around 2% whereas autogenous shrinkage reaches 0.7% at 24 hours.

Actually shrinkages are hindered because of the increase of solid congestion (granular packing and hydrates formation) which strengthens the material and limits deformation despite the drop in pore water.

The curves of hindered shrinkage for the 24 first hours of hydration are plotted for mix-design with 0%, 3%, 10% and 20% air volume content (*Figure 67*).

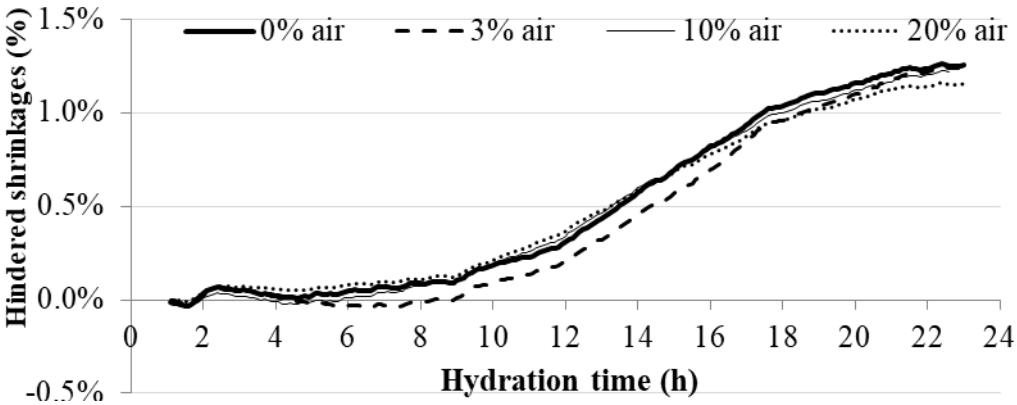

Figure 67. Hindered shrinkage for mix-design with 0 %, 3%, 20 % air volume content.

On this figure until 7 hours, hindered shrinkage is really low, because the sample deformations are free (high compressibility of the solid particle network). Hydration rate is high from 11 to 18 hours; hindered shrinkage slope is also high as observed in *Figure 67*. Hydration reaction rate slows down after 18 hours and variations of hindered shrinkage are smaller. Hindered shrinkages seem comparable for all mix-designs because the gap induced by the air content is almost the same for both chemical shrinkage and autogenous shrinkage.

b) Evolution of compressibility coefficient

The compressibility coefficient is measured on the reference mortar (3% air) in order to follow the evolution of the rigidity of the sample with hydration time.

The compressibility coefficient is computed on the range of pressure corresponding to pore water pressure variation recorded for the studied mortar (from 0 to 70kPa). An example of test results is plotted in *Figure 68* and provides the evolution of void ratio with effective stress.

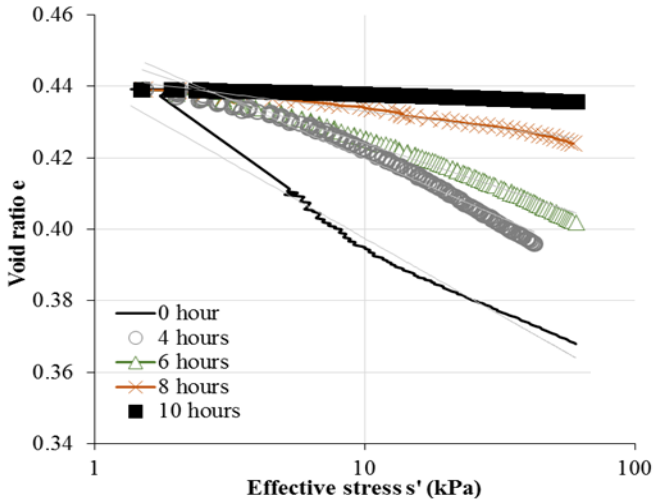

Figure 68. Recorded evolution of void ratio as a function of effective pressure for the reference mortar at 0, 4, 6, 8 and 10 hours.

As shown in *Figure 69*, the compressibility coefficient (slope of the curves of *Figure 68*) decreases with mortar age. The compressibility coefficient is divided by more than one order of magnitude at the

age of 10 hours (from 0.02 to 0.001). This build-up of the solid network due to hydrates creation permits to progressively hinder the chemical shrinkage.

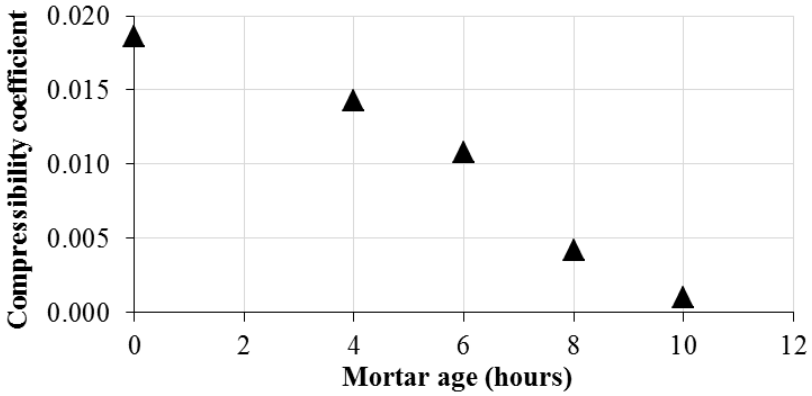

Figure 69. Evolution of the solid network (compressibility coefficient) of the reference mortar with material age.

4.4 Pore water pressure measurement

Pore water pressure evolution is measured in relative pressure (0 pressure considered as the atmospheric pressure) and plotted for each mix-design (*Figure 70*).

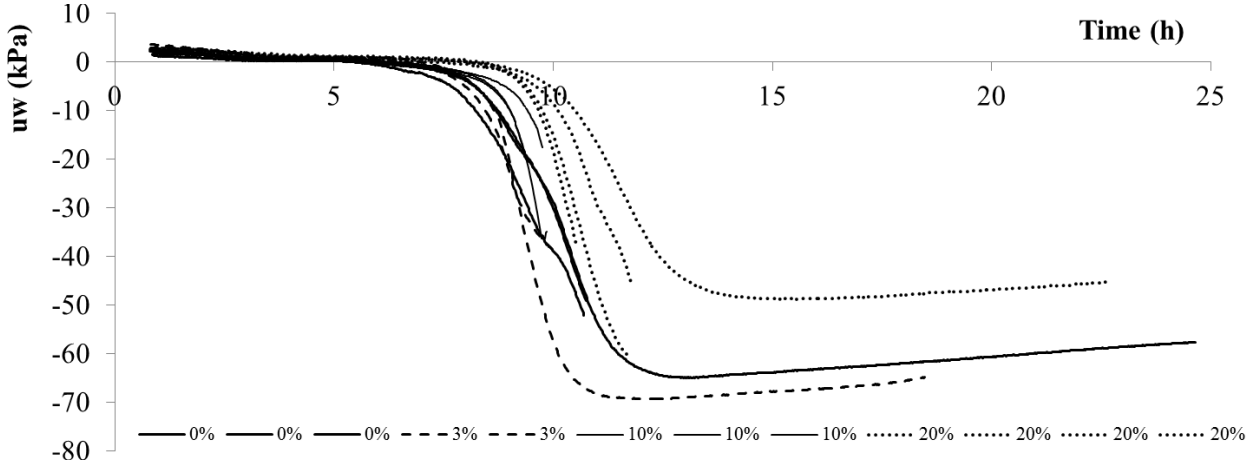

Figure 70. Pore water pressure as a function of time depending on air content.

It is observable that with lower air content, pressure drops faster. The sensor measures the pressure locally; this is why the curves of the same air content are slightly different. The curves were cut when the pressure comes back positive for better visibility, which represents the fact that at the measurement location, the air network is continuous.

Regarding *Figure 67* and *Figure 70*, two stages can be observed: in the first one, from 0 to 6 hours, the pressure slowly decreases. Then, in a second stage from 6 to 10 hours, hydration only consumes small amount of water, thus few hydrates are created, leading to a significant and rapid pore water pressure decrease. However, this sudden drop in pore water pressure has to be understood and explained by a model according to the microstructure morphology and the micromechanical behavior of the early-hydrating granular packing. In the following, a model is developed in order to link the stress evolution within the material to its volume deformation taking into account the ongoing chemical activity. This model aims to explain this two stages evolution of the pore water pressure.

5. Modeling

5.1 Physical assumptions on air cavities morphology, expected mechanism and modeling description

In order to link the macroscopic deformation of the sample (autogenous shrinkage) to the stress and pressure state within the triphasic system (air, interstitial liquid and solid network), it is necessary to make some assumptions and to evaluate the contribution of the different mechanisms acting at the microscale. As said before, there is no drying phenomena in the samples here. In *section 4*, it has been shown that the pore pressure exhibits a two stages evolution. This is assumed to be attributed to a change of pore size distribution and pore filled with air or water with hydration time.

Cement hydration increases the solid volume fraction of the material because of hydrates formation; there is a continuous volume evolution of the three phases, inducing variations on liquid pressure, gas pressure and effective stress submitted to the solid phase. Water volume reduction, hydrates creation and air expansion induce meniscus formation as represented in *Figure 71*. Air volume and shape are characterized over time: water consumption influences the air pressure that induces water pressure and granular skeleton stress evolution.

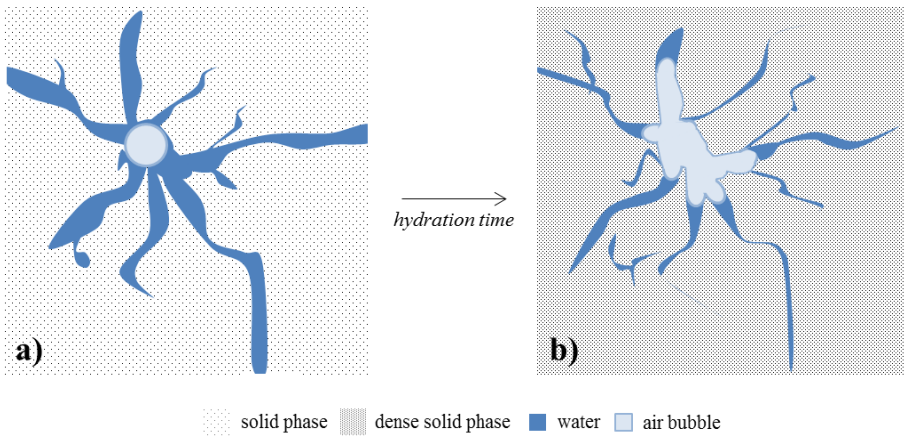

Figure 71. Hypothesis on the evolution of the shape of an air bubble in a water pore surrounded by solid phase.

The number of water pores increases and the size of pore diameters decreases upon hydration (*Figure 69* and *Table 10*). On *Figure 71.b*, the equilibrium of the system leads to the same meniscus radius for all water pores linked to the same air bubble.

Regarding the equilibrium on liquid and gas pressure, homogeneity of liquid pressure value implies the homogeneity of pore diameter filled with water. Furthermore, vapor transfer can be neglected because the relative humidity stays very high into the mixture: for a capillary pore diameter between 1µm and 10µm, which is the order of magnitude of the maximal filled pore, the capillary pressure is around 30kPa and according to Kelvin law, the relative humidity is 99.98%. In this range of relative humidity, the transfer between liquid water and vapor water is negligible. Moreover, the cavitation pressure is -5MPa at 18°C [82].

On *Figure 69.a*, at the beginning of hydration, air is in the form of spherical gas bubble surrounded by water, air pressure is equal to liquid pressure, this means the difference between liquid pressure and gas pressure can be neglected when the bubble radius is still high. When hydration accelerates, pore

diameters reduce and the difference between air pressure and liquid pressure has to be taken into account. In Laplace-Young equation, the angle θ is considered to be 90° because of the pore size. It is then assumed that in the first stage of the pore pressure evolution, the capillary pressure is close to 0 while in the second stage, capillary pressure increases with the appearance of small liquid menisci in the solid pores. Such phenomenon can explain the high drop in pore pressure (*Figure 70*).

Consequently, the maximum filled diameter is computed in different ways (from thermodynamic computation and shrinkage measurement) in order to verify this expected mechanism of pore water pressure evolution (*Figure 72*).

The first approach, named THERM, consists on predicting capillary pressure using the thermodynamic tool for the reference mix-design (3% of air content). In the second approach named EXP, the influence of air content is studied using hindered shrinkage and the measured liquid pressure. The different steps of the two methods are described in *Figure 72*. Finally, compressibility measurements confirm the effect of pore water pressure on the stress of the skeleton and is compared to autogenous shrinkage observations.

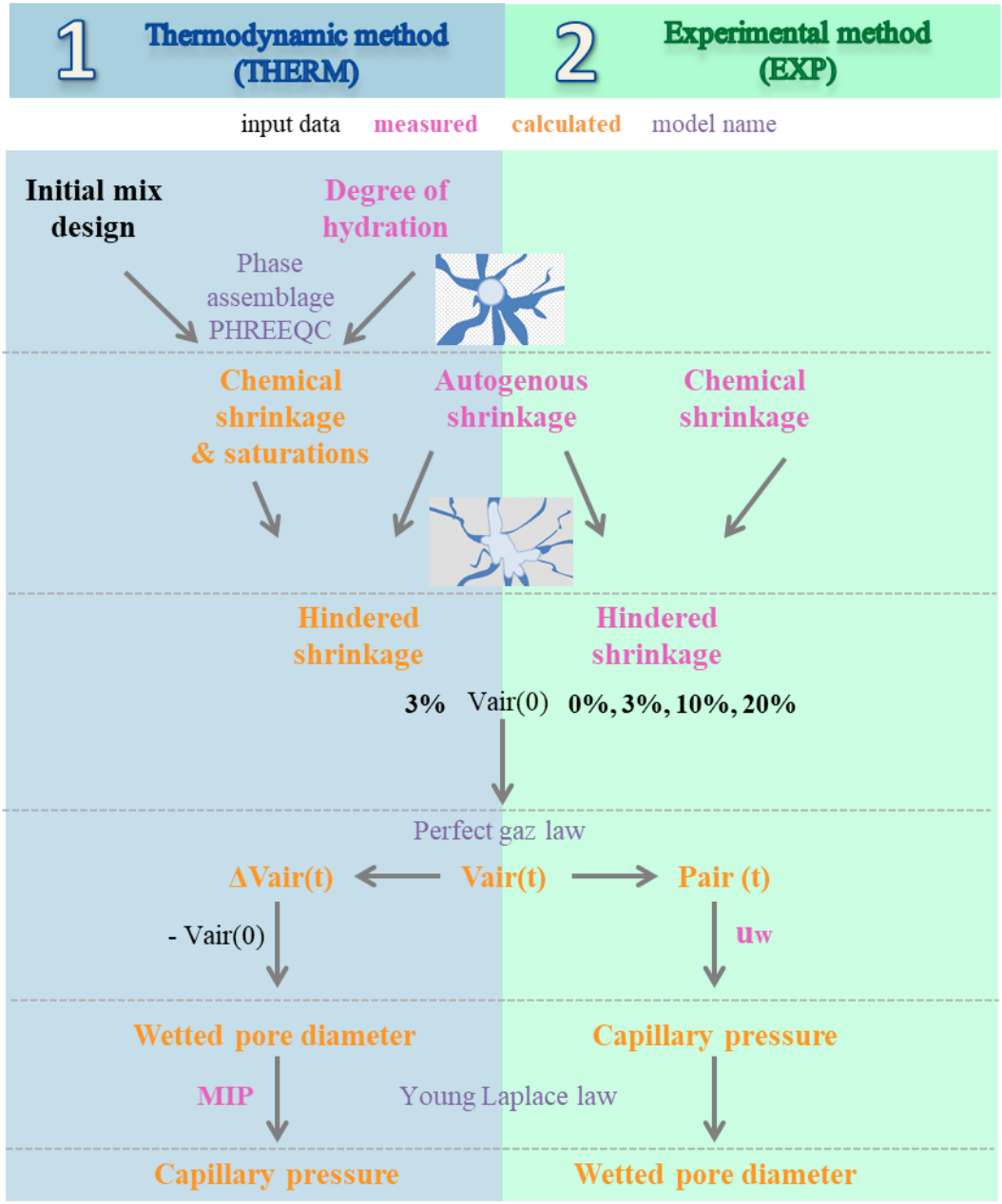

Figure 72. Description of the different data (input, measured and calculated) and protocol used for THERM method and EXP method.

It is also interesting to study the role of the solid matrix rigidity on the hindered shrinkage during the cement hydration. At first stage, the cementitious matrix presents a very low apparent rigidity and the volume variation is governed by chemical reactions. The order of magnitude of the rigidity computed with the compressibility curves ranges between 0.25MPa after the mixing and 0.5MPa at 4 hours.

However, when a solid hydrates network is formed, the rigidity raises up to 46MPa at 10 hours for the reference sample under an effective stress of 30kPa. This rigidity is calculated by linearization of the evolution of the effective stress in function of the deformation when the effective stress approaches 30kPa. This rigidity is in line with the measured hindered shrinkage under a given negative pore water pressure: according to Terzaghi's theory, the pore water pressure induced by the hindered shrinkage

creates equal effective stress acting on the granular network that deforms the mortar. According to the pore water pressure vs. hindered shrinkage curve, the mortar rigidity compensating the chemical shrinkage is equal to 45MPa which is very close to the material instantaneous rigidity evaluated using compressibility.

5.2 Analysis of the mechanism on reference mix-design

The different steps for this method are summarized on *Figure 72*. Knowing the initial air content, hindered shrinkage measurements lead to an increase of air volume. Degree of hydration determined in 4.2.a allows calculating the decrease of water content, hydrate and anhydrous volumes thanks to phase assemblage from thermodynamic calculation at a quasi-constant total volume (autogenous shrinkage almost constant). The result is a total decrease of porosity and evolution of liquid and air saturation in the porosity (volume fraction normalized by the volume of pores).

Mercury Intrusion Porosity data and liquid volume permits to calculate the maximal pore diameter filled (*Figure 74*). This diameter is calculated by minimizing the difference between liquid saturation obtained from thermodynamic calculation and saturation obtained from pore size distribution. For intermediate calorimetric point, linear interpolation of MIP fitted data is used to get pore size distribution information at any time. The calculation is very sensitive to the standard deviation of the mode 0 of pore size distribution. This measured standard deviation is adjusted to minimize the difference between wetted pored diameter of both THERM and EXP methods. Amplitudes and means of each mode are not modified. The final square root of mean squared error for liquid saturation is of the order of 4 percent.

Using Young-Laplace law and the maximal pore diameter filled, it is possible to calculate capillary pressure. Assuming a closed system, gas pressure is deduced from gas volume and the ideal gas law. Vapor pressure (2.10^3Pa) is smaller than the air pressure (10^5Pa), thus vapor total mass change is neglected as detailed before. Finally, liquid pressure is calculated from capillary and gas pressure and compared with experimental data in *Figure 74*.

The evolution of the pore diameters and air/liquid saturation as a function of the degree of hydration are plotted on *Figure 73*.

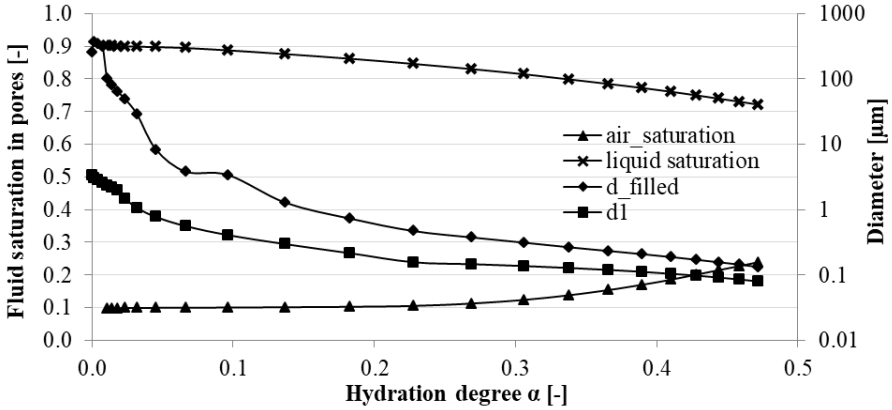

Figure 73. Evolution of air saturation, liquid saturation and pore diameter versus the degree of hydration.

The liquid saturation (which is defined as the ratio of liquid volume over the sum of gas and liquid pressure) decreases because air saturation increases. This is correlated with the desaturation of pores; this means the diameter of the pores filled with water decreases with the microstructuration from water

consumption. At the beginning, the filled diameter is controlled by the air bubble distribution, then the filled diameter is controlled by the paste microstructuration.

5.3 Pore size estimation with different air content

In order to estimate the pore size, chemical shrinkage and autogenous shrinkage first permit to calculate hindered shrinkage and therefore the increase in air volume. Considering the perfect gas law, the measured liquid pressure, the variation air pressure, capillary pressure and the wetted pore diameter are calculated. Those different steps are added up on *Figure 72*.

Pore water pressure can be described as a function of hindered shrinkage (HS), initial air content ($V_{air}(0)$), maximal wetted pore diameter (D(t)) and water surface tension (γ), Eq.(12).

$$u_{w(t)} = \frac{u_{w(0)}}{1 + \frac{HS}{V_{air(0)}}} - \frac{4.\gamma}{D(t)} \quad (12)$$

The maximal pore diameter filled with water can be written (Eq.(13)). It is compared with the first method in *Figure 74*.

$$D(t) = \frac{4.\gamma}{P_{air(t)} - u_{w(t)}} \quad (13)$$

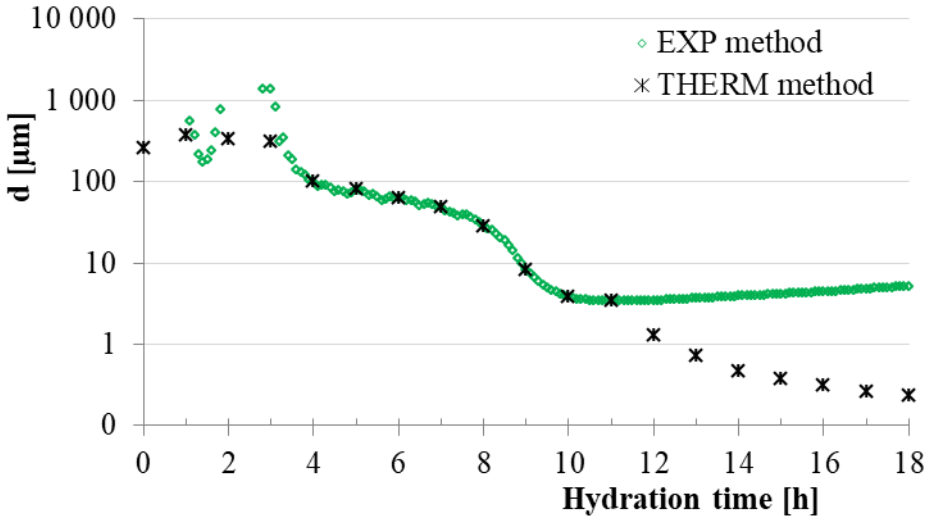

Figure 74. Comparison of prediction of maximal pore diameter filled with EXP and THERM methods as a function of time.

The order of magnitude of diameters predicted with the two methods is very close. The diameter predicted with method THERM decreases to lower values than the diameter predicted with method EXP because the range of measurement of pore water pressure is limited by the local sensor. This is also the reason why the diameters predicted with method EXP seem to increase; it is an artifact of the measurement of pore water pressure due to air entry.

The impact of initial air content is studied on the maximal wetted pore diameter; it is plotted as a function of the hindered shrinkage on *Figure 75* to be more representative of the phenomenon.

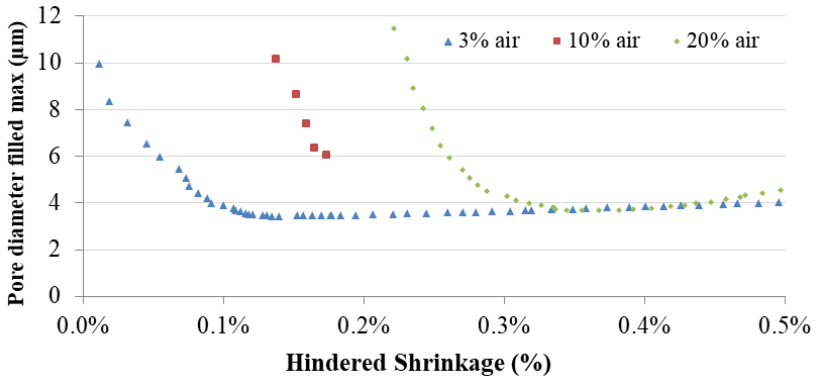

Figure 75. Pore size filled with water as a function of hindered shrinkage.

Pore diameter is calculated thanks to the EXP method, this means after air entry in the pore water pressure measurement, pore diameter calculation is not anymore valid. This is the case for the plot with 10% air content after 0.2% of hindered shrinkage. An increase of air content delays the hindered shrinkage. Moreover, it was not possible to apply the model for 0% of initial air volume.

5.4 Comparison of the methods and pore pressure prediction

The pressure of air and water are compared in *Figure 76*.

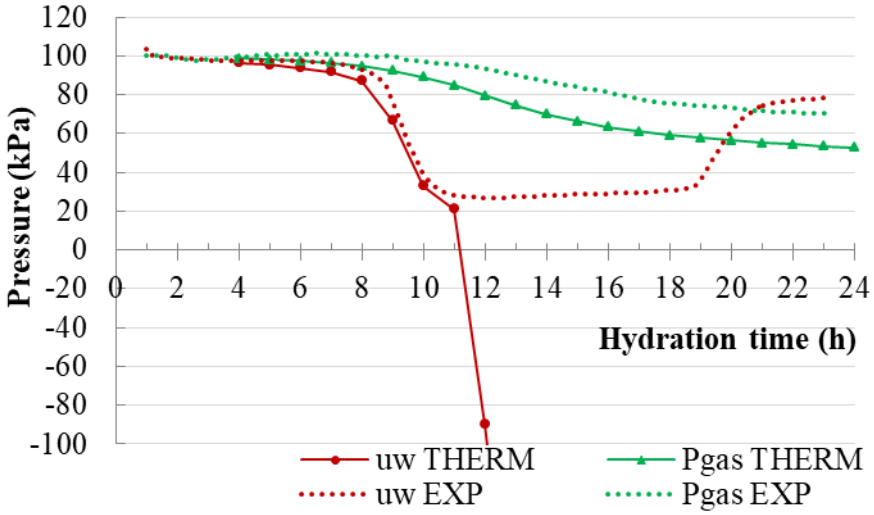

Figure 76. Liquid and gas pressure as a function of time, calculated from calorimety and MIP experimental data along with calculated phase assemblage and Young Laplace equation.

The liquid pressure THERM and EXP are close, up to 10 hours because of the proximity of pore diameters described in *Figure 74*. Gas pressure of the two methods are relatively close. This shows that the THERM method can be used to predict gas and water pressure when it is no longer possible to measure the pore water pressure.

6. Conclusion of chapter 2

Chemical and autogenous shrinkages have been linked to the pore water pressure. By calculating the air volume expansion directly linked to the hindered shrinkage and the ideal gas law, air pressure was calculated versus hydration time. The ideal gas law was appropriate because phase transfer from liquid to gas in the air bubble was shown negligible for those hydration times. Thanks to the capillary Young-Laplace law, the maximal water filled diameter was evaluated. Those values were confirmed with Mercury Intrusion Porosimetry measurements and water volume balance calculated by the thermodynamic tool. With calorimetry, a phase diagram was obtained. Beside to autogenous shrinkage, compressibility of the skeleton was evaluated thanks to odometric measurements. Influence of the used admixture was monitored especially regarding degree of hydration and surface tension. Finally, pore water pressure was predicted and compared to measurements. The influence of air was studied, air plays the role of expansion cavity, it reduces pore water pressure and lowers the effective stress. An original way of plotting the pore water pressure and pore diameter as functions of hindered shrinkage was described. One of the main outcome was the thermodynamic model allowing to predict pore pressure even when the measurement is no longer possible.

As seen in this chapter the negative pore water pressure has an important impact. It has an influence on the effective stress and surface properties. The following chapter focusses on the influence of this negative pressure on the rheological and tribological behavior of the cementitious materials, i.e. in the material matrix and at the interface.

Chapter 3: Controlling water pressure of mineral suspensions – and shear behavior characterization

1. Introduction

Taking into account the pressure drops monitored in the previous chapter, there is a need for a comprehensive and quantitative evaluation of the impact of pore water pressure on the bulk (rheology) and interfacial (tribology) shear behavior of cement-based materials in order to predict and prevent the occurrence of surface damages during the slipforming process.

The aim of the present chapter is to understand the phenomena affecting the adhesion and the friction at the interface between the building-up concrete and the steel formwork. More precisely, the objective is to quantify the relative influence of controlled negative pore water pressure on the interfacial and bulk rheological behavior of mineral suspensions, such as cement-based material in the fresh state. In order to isolate the effect of the pore water pressure from any chemical adhesion, the experiments are conducted on an inert material (limestone filler) using a water pressure-controlled device connected to a rheometer. This device has been specifically designed for the present work.

After a description of the device and a reminder of the theory of the physical phenomena, the behavior of the material is examined under various levels of pressure and device rigidities that may allow or not volume changes of the material. Initial air content, which is expected to be an important parameter (air volume variation with pressure), is adjusted to study its influence on recorded shearing behavior. Finally, the effect of negative pore water pressures on the bulk and interfacial shear behavior is determined and quantified for pressure values ranging from 0 to -30kPa.

2. Water pressure-controlled device

The designed device is composed of a small cylindrical box where the water pressure can be decreased under atmospheric pressure (controlled negative pressure) to simulate the effect of cement hydration. The bottom of the measuring cell is equipped with a membrane. The membrane type can be changed in order to test the rigidity of the device. The cell is placed on a rheometer with vane geometry in order to measure the yield stress (bulk shear yield stress), or with a smooth cylindrical geometry to characterize tribological properties (wall/material interfacial shear yield stress). The measuring cell is 50mm high and 50mm-in-diameter (*Figure 77.a)*, i.e. as small as possible to guaranty the homogeneity of the material and to neglect the particle size effect of the chamber (i.e. the gap between blades and chamber is 10 times larger than the diameter of the biggest particles [83]). The system is equipped with pressure volume controllers (GDS ELDPC) acting as instrumented syringes in order to control and to decrease the water pressure. The entries of the syringes are equipped with 15mm long filters made of cellulose acetate designed to retain small particles with diameter higher than 0.3µm that prevent solid particles migration. They are filled with de-aerated water and allow the data recording of pressure and volume variations. To improve the homogeneity of the material when water is pumped, a small metallic grid covers the inside of the chamber. A paper filter (Qualitative filters 5-8µm SERVILAB) is placed between the grid and the material. This system is designed to act like a drain through the outer surface of the cylinder box.

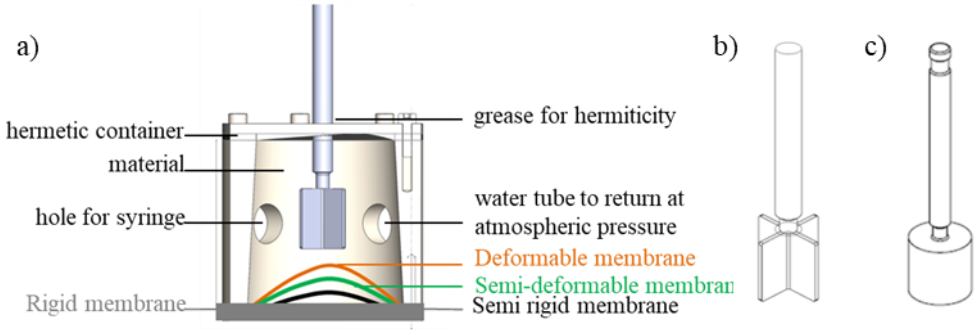

Figure 77. a) Controlled pressure device to measure yield stress. b) Vane geometry for bulk rheology measurements c) Tribology geometry for interfacial rheology measurements

This device shows similarities with the one developed by Lecompte et al.[83]. In their study, the authors developed a setup to measure simultaneously torque and pore water pressure for a concrete sample. However, in their system, the water pressure variation is the result of the dilatancy of the material and chemical activity; whereas in the present work, the aim is to properly control the pressure. The dimensions of both geometries are 18mm in height and 18mm in diameter.

During those states, the rheology and tribology are crucial parameters to characterize the cement-based materials. Rheology and tribology characterization are detailed in the first part of this chapter.

3. Physical background

3.1 Bulk yield stress measurement: rheology

The slump is the most used method to describe fresh concrete behavior because it is the easiest to use in the field but it is not representative of high shear rate. Slump is rather representative of the yield stress but the flow behavior can differ for two concretes with the same slump. This is why rheometry is used to describe fresh concrete behavior. Tattersall and Banfill [84] split the flowing properties between the qualitative properties that are observable on site, the empirical ones that are quantitative but not precise and the necessity of the rheological parameters (*Table 12*).

Table 12. Tattersall and Banfill flowing properties qualification [84].

Qualitative evaluation	Quantitative empirical evaluation	Fundamental rheological parameters
Fluidity	Slump	Viscosity
Spread	Slump flow	Yield stress
Stability	V-funnel flow time	Thixotropy
Pumpability		

Rheology was proposed first by Eugene C. Bingham in 1928, it is the “science for the study of deformation and material flowing” [84], it is the study of the manner of how the fluid flows under stress, it is used to describe a lot of material flowing as for instance cosmetics, drugs, plastics or food products.

Under laminar flow, the flowing can be described as *Figure 78*.

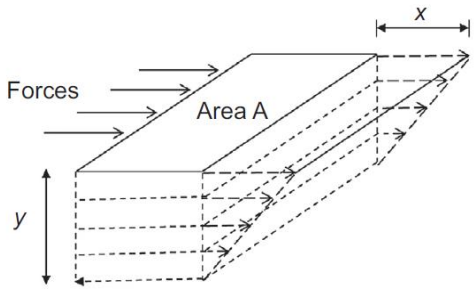

Figure 78. Schematic illustration of laminar shear flow [15].

During a laminar flow, two layers move along each other, friction between two layers is called shear stress τ [in Pascal] which is defined as the strength F to move a layer over the area of shearing S, Eq.(14).

$$\tau = \frac{F}{S} \tag{14}$$

The shear rate $\dot{\gamma}$ [expressed in s^{-1}] is the derivate with respect to time of the shear strain γ, Eq.(15).

$$\dot{\gamma} = \frac{d\Upsilon}{dt} \tag{15}$$

The different fluids can be classified as exhibited on (*Figure 79*).

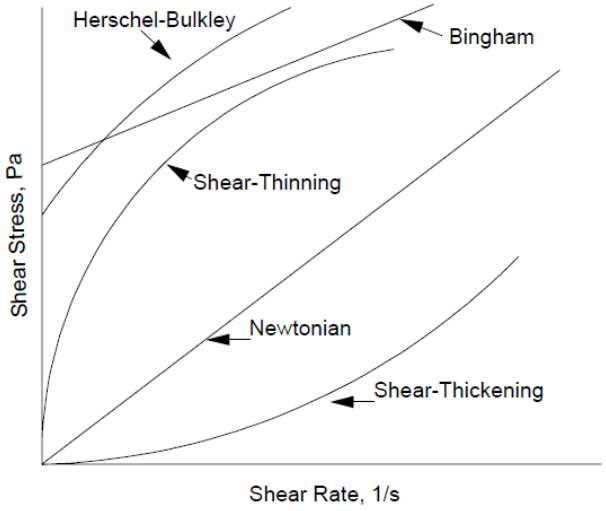

Figure 79. Curves from typical time independent fluids: shear stress evolution as a function of shear rate [85].

The slope of those curves from the origin corresponds to the viscosity [Pa.s]. The viscosity is the ratio of the shear stress over the shear rate. Excepted for a Newtonian fluid, it depends on the shear rate (Eq.(16)).

$$\eta(\dot{\gamma}) = \frac{\tau(\dot{\gamma})}{\dot{\gamma}} \tag{16}$$

The viscosity represents the resistance during the deformation under stress. All the other fluids - when viscosity is not linear- are called “non-Newtonian fluids”. The characteristics of these fluids is considered as not depending on the time. Shear thinning and shear thickening refer to pseudo-plastic and dilatant behavior. The viscosity of a shear thinning fluid decreases with shear rate whereas it increases for a shear thickening fluid.

Cement-based material is generally described as a Bingham fluid, which means that the shear stresses vary linearly with shear rate beyond the yield stress defined as a threshold shear stress above which the material starts to flow [15].

The proportional factor is called plastic viscosity μ_p [Pa.s] and Bingham model can be expressed as Eq.(17).

$$\tau = \tau_0 + \mu_p.\dot{\gamma} \tag{17}$$

In the present study, the shear stress is considered low enough to be neglected. Then only the evolution of yield stress with drop in pressure will be assessed.

3.2 Thixotropy

Thixotropy is a time dependent characteristic, it is a change of shear stress depending of the solicitation time (*Figure 80*).

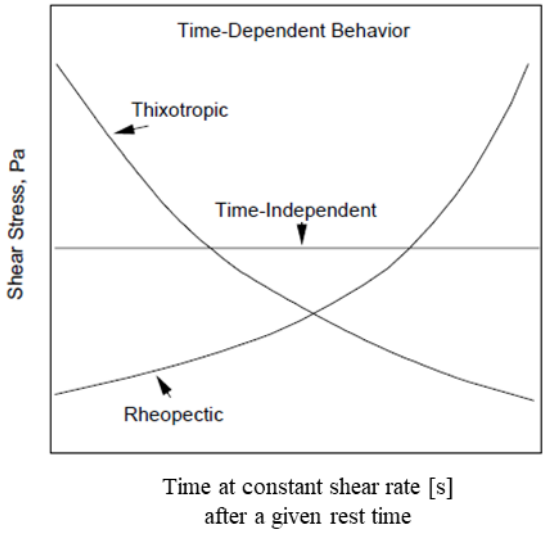

Figure 80. Time dependent behavior of fluids: evolution of shear stress as a function of time [85].

Thixotropy occurs in cementitious materials and is well known [8].

To understand why cement materials become rigid a rest, it is necessary to take into account the organization of the cement grains network in water. After mixing that leads to unstructured state, the cement grains begin to flocculate due to colloidal interactions. This flocculated structure induces an increase of both the rigidity and strength of the material, over time periods lasting tens of seconds [5]. Then, after this period but still before setting, early formation of C-S-H linkages in the contact zones between the grains go on to form the origin of the continued mechanical structural build-up of the cementitious material et rest [8]. These nucleation sites are chemically irreversible phenomena. However, if the power of the pumping and/or mixing system is sufficient, these links may be broken.

The increase of the progression of the yield stress over time is often considered to be linear and allows a structural build-up rate to be defined as A_{thix} [in $Pa \cdot s^{-1}$] [8]. Such evolution is likely to affect the static yield stress measurements at low shear rate and during long period. To avoid any perturbation induced by the material build-up due to cement activity, it has been chosen to work on an inert material suspension to more easily isolate the effect of pore pressure on shear strength. In this chapter, a limestone filler is used in order to not have a thixotropic behavior.

3.3 Shear stress measurements on the device

Dense colloidal suspensions, such as limestone or cementitious material pastes, exhibit shear yield stress in the bulk (rheological behavior) and at the interface (tribological behavior) as shown in [86] [87]. Torque (M_i) is measured using a MCR 502 Anton Paar® rheometer. τ_0, the bulk yield stress (rheological behavior) of the suspension is measured [83] with vane geometry (h: height, d: diameter of the tool), and τ_{w0} is considered as the wall/material interfacial yield stress (tribology) and measured with the cylinder geometry tool. The relation between torque and these two stresses is the same, assuming that the shear surfaces induced by the rotation of both tools are similar; Eq.(18) is applied.

$$\tau_i = \frac{2}{\pi d^3 \left(\frac{h}{d} + \frac{1}{3}\right)} . M_i \tag{18}$$

with M_i the torque during the shearing test. Note that i=0 when using the vane geometry to measure the bulk yield stress τ_0 (rheology) and i=w0 when using the smooth cylinder to measure the interfacial yield stress τ_{w0} (tribology).

Torque is measured with a rate of 0.01rad/s, for which the viscous effects can be neglected [88], and the interfacial velocity is close to the ones that are encountered during the slipforming process [4].

3.4 Rigidity of the device

Different configurations of the device are developed, from non-deformable to almost completely deformable volume, using membranes of various rigidities (*Figure 77.a*) since the purpose is also to take into account the influence of the container rigidity. The non-deformable system does not allow volume variation of the solid particle network and the removed water volume is compensated only by air volume expansion. In contrast, the completely deformable membrane (placed at the bottom of the box) should allow effective stress increase, following Terzaghi's principle (*Chapter 2*): the removed water volume is compensated by the volume variation in the device, depending on the rigidities of the membrane and of the granular packing. In this case, the volume variation is controlled by the consolidation kinetics of the granular network and limited by its compressibility.

The analytical calculation of the associated sample volume variation requires evaluating the elasticity parameters of the membrane. These elasticity parameters are taken from the literature (i.e. the stainless steel and polymer database) or determined by a uniaxial tensile test with a Shimadzu AGS-X tensile test machine at a speed of 0.1mm/s and a load cell capacity of 5kN +/- 0.5% (*Table 13*).

Table 13. Determination of the mechanical parameters of the membranes used in the pressure-controlled device.

Membrane type	Young modulus [MPa]	Poisson's ratio [-]	Thickness [mm]
Rigid Stainless steel	220 000**	0.29**	4.90*
Semi-rigid Polypropylene	1567*	0.43**	0.94*
Semi-deformable Rubber	6.60*	0.49**	2.00*
Deformable Polyisoprene	0.22*	0.49**	0.21*

**experimental determination* **Stainless steel and *Polymer database*

It is important to note that in the range of dense mineral suspensions Young modulus ranges around hundreds of kilo Pascal [89] [90] [91]. It means that the rigid stainless steel is approximately 10^6 times more rigid than the sample and therefore can be considered as perfectly non-deformable during the test. On the other side, the polyisoprene has approximately the same elastic modulus and is stressed in flexion. Therefore it is able to follow the deformation of the sample during the test. The sample volume depends on the membrane deformation. The volume is evaluated with the hypothesis of an ellipsoidal plate (*Figure 81.a*) to calculate the membrane deformation subjected to a uniform load with clamped edges [92] [93].

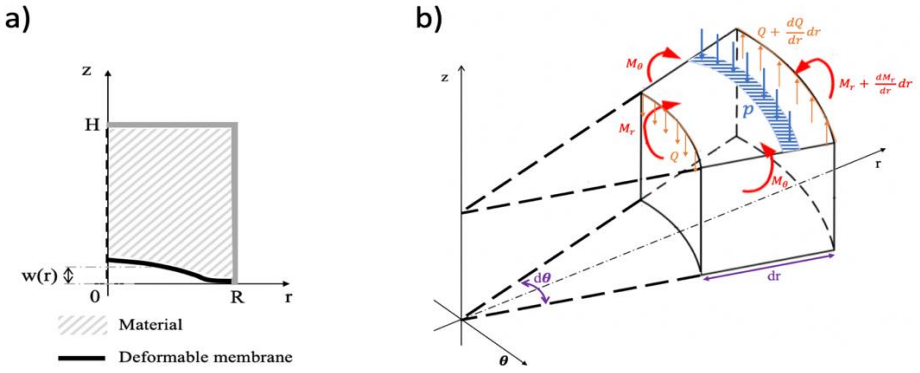

Figure 81. Scheme of the parameters needed for bending deformation a) axisymmetric representation b) cylindrical representation.

Thus, membrane bending displacement is defined as Eq.(19).

$$w(r) = \frac{3\,p\,r^4\,(1-\nu^2)}{16\,E\,t^3} \tag{19}$$

with w the membrane bending displacement [mm]; p, the uniformly distributed load [Pa]; r, the radius [mm]; h, the maximal bending displacement [mm]; t, thickness membrane [mm]; E, the Young modulus, υ, the Poisson's ratio

Each bending deflection is associated to a volume variation of the sample depending on the pressure considering the membrane as a spherical cap (Eq.(20)).

$$V_{sample} + V_{tool} = 2\pi \int_0^R r\,dr \int_{w(r)}^H dz = 2\pi \left[\frac{H\,R^2}{2} - \int_0^R r\,w(r)\,dr\right] \quad (20)$$

with r, the radius of the cap [mm]; h, the maximal bending deflection [mm], H, height of the box [mm]; R, device radius [mm].

Eq.(20) is applicable for semi-deformable and semi-rigid membrane. For the metal rigid membrane, the membrane deflection is considered as negligible. Finally, for the completely deformable membrane, the membrane deflection is related to consolidation. The volume change allows to calculate a new W/B ratio because the water volume which is removed is equal to the V_{cap} for a defined water negative pressure.

Moreover, the bending displacements are verified experimentally: a displacement sensor, with an accuracy of 10 microns is placed under the device in order to measure the maximal displacement value obtained for each level of water pressure. The degree of freedom given by the deformable membrane involves evaluating the device volume variations under negative water pressure. The analytical calculation of this volume variation requires knowing the elasticity parameters. The results are summarized in *Table 14*.

Table 14. Bending deformations calculated with the elasticity parameters.

	Water pressure	**Rigid** Stainless steel	**Semi-rigid** Polypropylene	**Semi-deformable** Rubber*	**Deformable** *Polyisoprene**
Bending deflection [mm]	-10 kPa	0.000	0.004	0.103	$2.63.10^3$
	-20 kPa	0.001	0.009	0.207	$5.26.10^3$
	-30 kPa	0.001	0.013	0.310	$7.89.10^3$
Cap volume [mm³]	-10 kPa	0.250	4.418	101.514	$9.51.10^9$
	-20 kPa	0.499	8.835	203.031	$7.61.10^{10}$
	-30 kPa	0.749	13.253	304.555	$2.57.10^{11}$

Bending deflection of the deformable membrane is not realistic, it was experimentally determined on traction machine but due to the compressibility of the material, those deflections are not observed. It means that with this membrane, the rigidity of the device has no influence on the results.

In order to verify this analytical extrapolation of bending deformation, a comparison can be made between these values and the bending deformation experimentally measured under negative water pressure for the semi-deformable membrane (*Figure 82*).

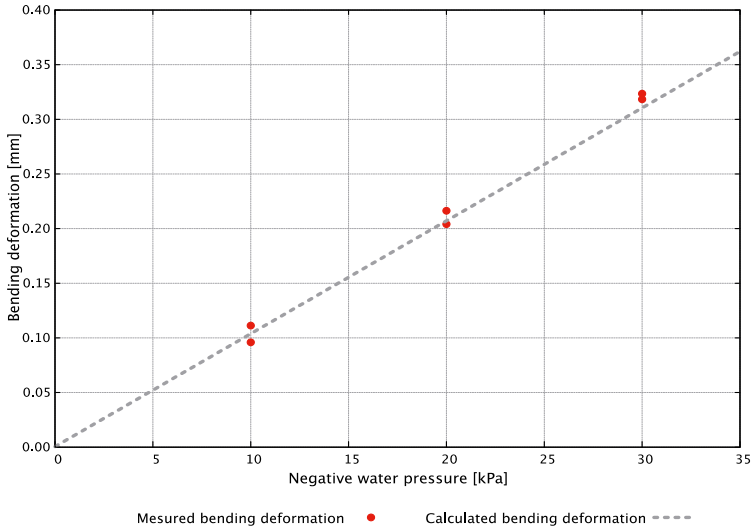

Figure 82. Bending deformation as a function of negative water pressure for semi-deformable device.

The accuracy of the analytical correlation allows calculating the volume of the sample for each configuration. The volume changes are used for the discussion part.

3.5 Air behavior in cement-based material

The impact of air on hardened concrete in order to improve the durability of concrete in severe winter conditions is well known. However, air content also affects fresh state behavior of concrete even if it decreases the mechanical performances.

Air content in concrete can be entrapped air or entrained air, this difference is important because the behavior of concrete is not impacted in the same way.

Entrapped air is the air entrapped during placing. Without an air entraining agent the bubbles collapse and thanks to buoyancy law, they go at the surface and are eliminated, the size of those bubble ranges between 0.3 to 5mm which is the **sand particles** size range. Air bubble entrapped with vibration after placing are large, irregular shape and irregularly distributed [15], the content of entrapped air depends on viscosity, size of the aggregates, slump, time of vibration and intensity. For usual concretes, the average of entrapped air content is 1.5% of total air content [15].

Entrained air obtained with an air entraining agent is used in order to have an air bubble network very fine and well dispersed. Gagné describes the mechanisms of air entrainment as the shear paddles of a mixer create vortexes that trap air bubbles in the paste [15]. The average diameter of **entrained** bubbles stabilized is from 10 to 300µm, which is close to the **cement** particle size range [15]. The air entraining agent does not entrain air by itself, they are surfactants that stabilize air and liquid interface for the bubbles not to collapse and resist during the mixing. The hydrophobic end is absorbed at the air interface and hydrophilic in the liquid. This adsorption decreases air-water superficial tension. This is amplified with an increase of air entraining agent content. It is important to note that usually air entraining agent concentrations are lower than the Critical Micellar Concentration.

Air entraining agent is less efficient when W/C is high because of dilution. When the viscosity of concrete increases, it is more difficult to shear concrete, thus the energy to create the vortexes to create bubbles is higher, but the network is more stable because bubbles move less. Low viscosity is better

for vortex formation but bubbles are not well stabilized. An adjustment of the viscosity is thus needed to entrain and stabilize air bubbles. Aggregates size, shape and surface rugosity can also modify the entrainment of air [15].

Hot, in her PhD thesis [94], shows that the data around the effect of entrained air on rheology are controversy. Yield stress and plastic viscosity of usual concretes and non-fluid pastes decreases when air content increases whereas for self-concretes and fluid pastes, yield stress seems to increase and plastic viscosity seems to decrease with air content [94]. Recent studies have shown that the impact of entrained air in rheology depends on the nature of the surfactant (anionic or cationic) [95] [96].

The behavior of concrete and paste with air also depends on the applied shear rate, as illustrated in *Figure 83*. At low speed, surface tension prevents entrained air bubbles from deformations, they act as solid inclusions, thus increasing apparently the solid volume fraction. This is supposed to increase plastic viscosity but the effect on yield stress is less clear, it may depend on the cohesion of air bubbles in the paste microstructure [94]. At higher shear rates, air bubbles would be transformed and those deformations should reduce the plastic viscosity. Capillary number Ca, which is the ratio between viscous forces and surface tension force, is the relevant adimensionnal number to take into account this approach. Kogan et al. [97] confirmed this shear dependence for air bubbles deformation. This shear stress dependence of air can be used for concrete processing [15].

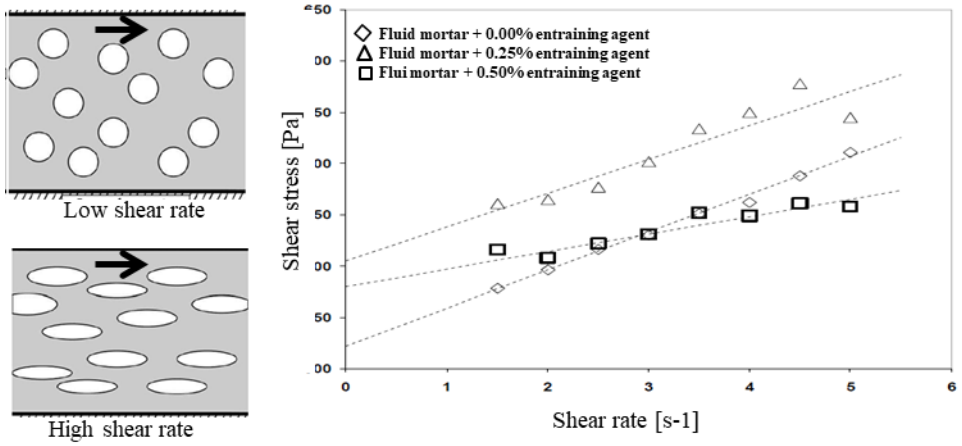

Figure 83. Scheme of the shape of air under shear and plot of shear stress as a function of shear rate for 3 fluid mortar with different air entraining agent quantities [adapted from Hot] [94].

It is known that air decreases the compressive strength of the hardened concrete. Nonetheless, the use of an air entraining agent allows to decrease the efficient water (with the lubrication effect), thus a small amount of air in concrete can be an advantage for workability. The durability of concrete is more affected by the W/C ratio than air entraining agent content [15].

4. Materials and mixing procedure

The inert mix is prepared with a Perrier mixer. It is made with a limestone powder (Saint Beat) and 37v% of fine sand (PE2LS 0/0.315µm) with a common polycarboxylate plasticizer admixture: Glenium 27 from BASF (0.063wt%/binder). The W/B ratio varies from 0.31 to 0.34. The limestone is

chosen in order to be representative of the particle size distribution of the cement, as illustrated in *Figure 84*.

The air volume fraction of the reference mix-design is 3%. Density is evaluated at 2168kg/m^3. To assess the effect of air inside the suspension, four air contents are tested: 0, 3, 10, and 20%. In this study, the air entraining (Master Air 104, solid content: 4w%) is an anionic surfactant that adsorbs to the mineral particles surface. This type of surfactant is known to increase the suspensions yield stress [95]. The material air ratio is determined by computing the difference between theoretical material density and material density measured before the test: These air ratio values have been checked by using an aerometer designed for cementitious materials.

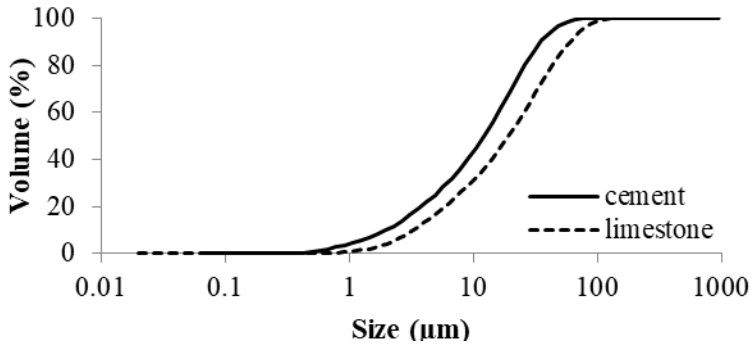

Figure 84. Cement and limestone cumulative particle size distribution used the material for the pressure-controlled device.

5. Experimental procedure and assessment of the device

5.1 Protocol

The protocol to assess the interfacial and bulk shear behavior of the material under the imposed negative pore pressure involves two distinct measurements:

- Step 1: the yield stress of the material is measured at atmospheric pressure (i.e. a relative pressure of 0kPa);
- Step 2: the sample undergoes negative pressure. Once the water pressure and volume are stabilized, the yield stress of the material is measured. Pressure stabilization lasts around two minutes.

Before each experiment, the material is mixed in the Perrier mixer in order to ensure the homogeneity of the material and avoid any dependency on the stress path history.

5.2 Device verifications and possible drawbacks

Interpreting the results requires that several assumptions are verified experimentally. First, homogeneity of the samples -when water is removed- is supposed (the water distribution in the material under pressure is assessed to control the relevance of this assumption). Uncertainties about the air volume in the sample during the test exist because part of the air volume can be removed with the liquid in the syringe. Membrane deformation and material consolidation during the test are characterized.

Waterproof grease is used between the tool and the hole in the lid that is needed to connect the rotating tool to the rheometer head. The friction of the greased joint is measured eight times. The shear

torque at atmospheric pressure is reproducible (standard deviation of 0.016mN.m) and very low compared to the expected contribution of the material (which is at least one order of magnitude higher). Friction between the tool and the top of the device is subtracted from all measurements.

5.3 Water distribution characterization

The water distribution around the tool is checked to control the homogeneity of samples and the preferential location of water removal with the syringe during the test. Water distribution is deduced using image analysis with a fluorescent agent. The single connection between the pressure/volume controller and the measuring cell makes it possible to localize the consolidation of the material, inducing heterogeneities within the sample.

To characterize water dispersion, a fluorescent agent (fluorescein) is dissolved in water and the material is prepared with the colored water (15mg/L). Image analysis is performed for water quantification, according to the standard RGB (8bits) coloring definition NF X08-010. The optical characteristics of the fluorescein are described in the literature [98] [99].

Calibration is conveyed with seven mixes with the W/B mass ratio ranging from 0.28 to 0.35 (*Figure 85.c*). Correlation between the green intensity and the W/B ratio is determined from a mean value of green intensity, on a square of 700 x 700pixels (*Figure 85.a*).

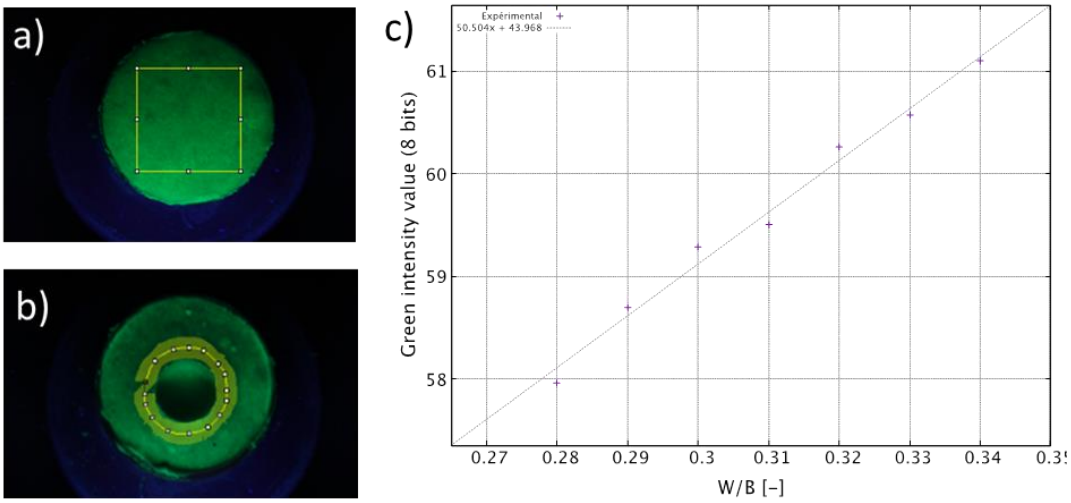

Figure 85. a) Calibration sample b) Cylindrical path around the tool for image analysis with fluorescence c) Calibration curve for fluorescence analyses W/B 0.28 to 0.35, r^2=0.98.

Once the proportionality coefficient between the W/B ratio and the green intensity transmitted is known, it is possible to determine the local water content for each point of a given sample after negative pressure conditions. The material is placed under pressure, removed from the mold, sliced precisely to 18mm high above the tool, placed in a transparent box and put in a black box lit with a UV-light (254nm) in order to take a picture of the sample on each of its side by flipping the box (*Figure 85.b*). A first profile in grey color on a circular path of 1600 pixels long and 140 pixels wide around the cylindrical geometry is computed with ImageJ, an image analysis software. Each of those values is then associated with a green value (436nm) and each of these green values can be assimilated to a local W/B ratio.

5.4 Compressibility measurements

Consolidation of the material is the main driving phenomenon of the deformable membrane (polyisoprene). As for the cement mortar (*Chapter 2, section 3.4.c*), odometric tests in drained conditions are conducted to estimate the consolidation as a function of the applied load, according to standard XP P94-090-1. When the volume variation of the sample settlement reaches a plateau, the whole of the applied load is viewed as being carried by the granular skeleton that has been consolidated because pressurized water has flown out of the sample: in this final state, the water pressure is null, and the effective stress is equal to the total stress acting on the sample. Consolidation tests are conducted on a reference mix-design with a W/B ratio of 0.34. The incremental loading is carried out on samples of 0.5kg in mass.

5.5 Total pressure and stress transfer

Total pressure is measured with a 250mbar pressure sensor FD8214 Ahlborn. Total pressure measurements are carried out apart from the regular test. Vane and tribology tools are not used for this specific test. This device is developed in order to verify Terzaghi's equation on the stress distribution between water and particles and to estimate the effect of air content on the stress balance. A new lid is designed: the device is placed upside down so that the material is in contact with the sensor. The holes for water removal are placed on both sides of the normal pressure sensor (*Figure 86*).

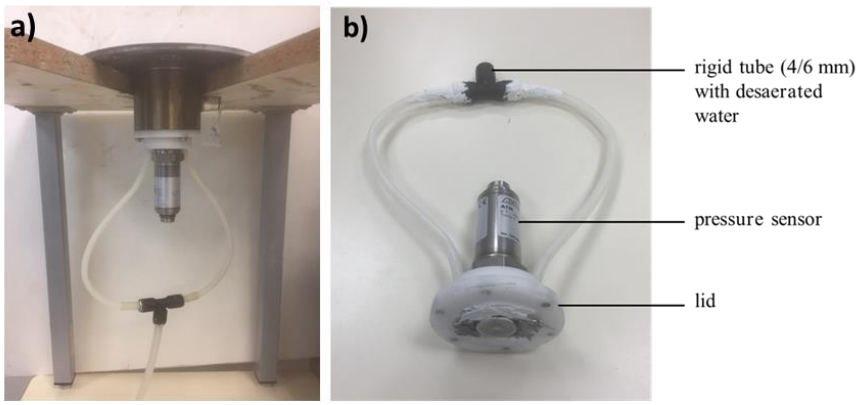

Figure 86. Illustration of total pressure measurement with the modified lid adapted on the pressure-controlled device.

6. Results

6.1 Device verifications and calibration

a) Membrane influence on yield stress behavior

The membrane influence on bulk (rheology) and interfacial (tribology) yield stress is examined for the reference mix-design (W/B: 0.34); the results for a negative water pressure of -20kPa are plotted in *Figure 87*.

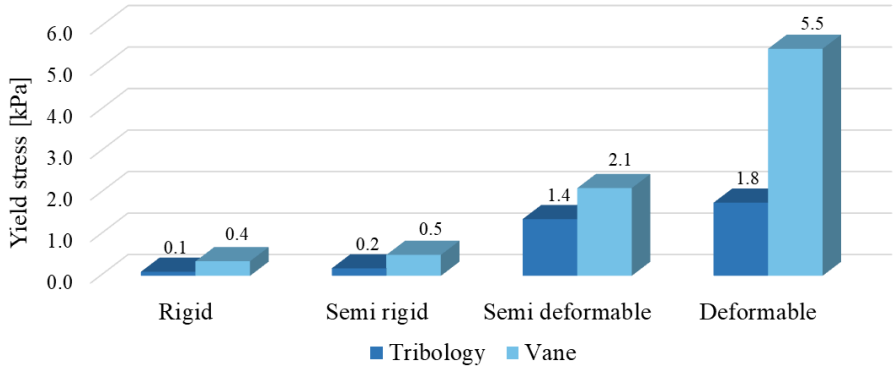

Figure 87. Yield stress values of the reference mix W/B 0.34 with the four different membranes of the pressure-controlled device.

The behavior of the material with the semi-rigid membrane is close to the one with the rigid membrane for both geometries: one possible explanation is that the two elastic moduli are largely higher than the one of the fresh suspensions (about three orders of magnitude for the polypropylene and six orders of magnitude for the stainless steel). Consequently, both of them hinder the sample deformation. The yield stress is increased by one order of magnitude between the rigid and the deformable membrane: the consolidation of the limestone suspension increases with the membrane softness. The vane geometry is more sensitive to the consolidation because it characterizes the bulk behavior of the material.

The following sections report the results of tests carried out with the rigid and semi-deformable device because on one hand, the semi-rigid membrane is close to the rigid one, and on the other hand, the deformable membrane is a limit case, in which the low compressibility of the limestone powder material limits membrane deformation.

b) Water distribution

The profiles are plotted for negative water pressures of -10, -20, -30kPa in *Figure 88*. Even if there is a slight variation in the water distribution for tests carried out with the rigid device, the W/B ratio varies of approximately 5% for the three tested pressures. This result is considered to be low enough to assume that the material remains homogeneous during the test.

Water distribution is also analyzed for the semi-deformable membrane, plotted in *Figure 88.b*. The test clearly shows that the consolidation of the material is higher and more heterogeneous at -20kPa and -30kPa pressure. This water content and the heterogeneity should be taken into account when dealing with the test results analysis.

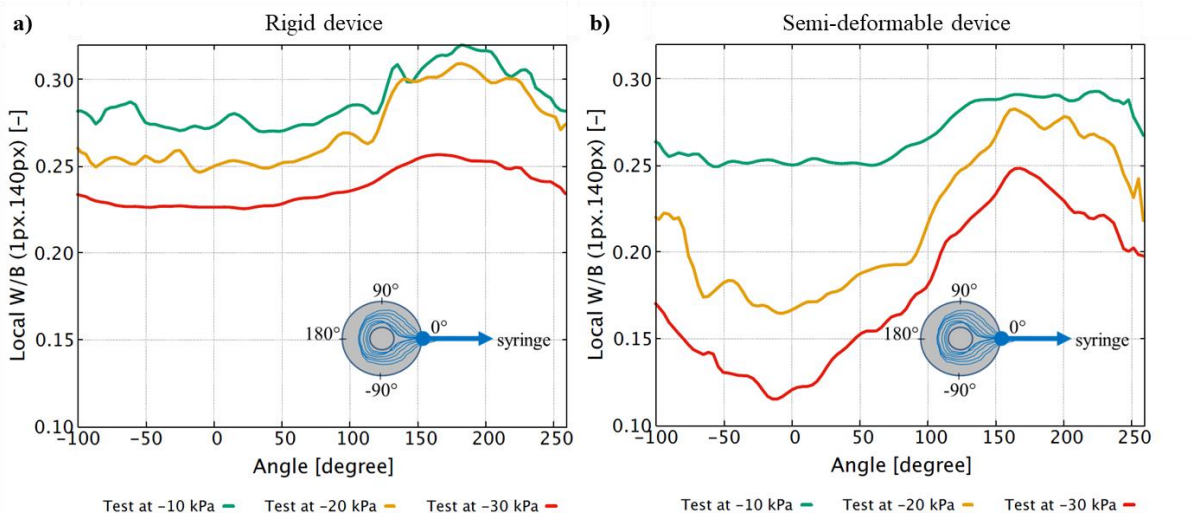

Figure 88. Local Water/Binder profile around the tool for a) the rigid device b) semi-deformable device in order to evaluate water distribution during water pumping in the pressure-controlled device.

c) Analysis of the effect of the pressure

For the analysis of the results, it is important to verify that the negative pressure is at the origin of the increase in yield stress and that it is not due to the change of water content in the material only. Hence, three different measurement steps are performed: at 0kPa (step 1) and -20kPa (step 2) for a given initial W/B ratio, and at 0kPa with the W/B ratio that is reached at -20kPa. This third step is called the "verification step".

With the rigid device, the pumped water volume enables direct calculation of the new W/B ratio because the sample volume and the solid fraction are constant. With the semi-deformable membrane, the sample volume changes and the solid fraction increases. Typical yield stress measurements are plotted in *Figure 89*.

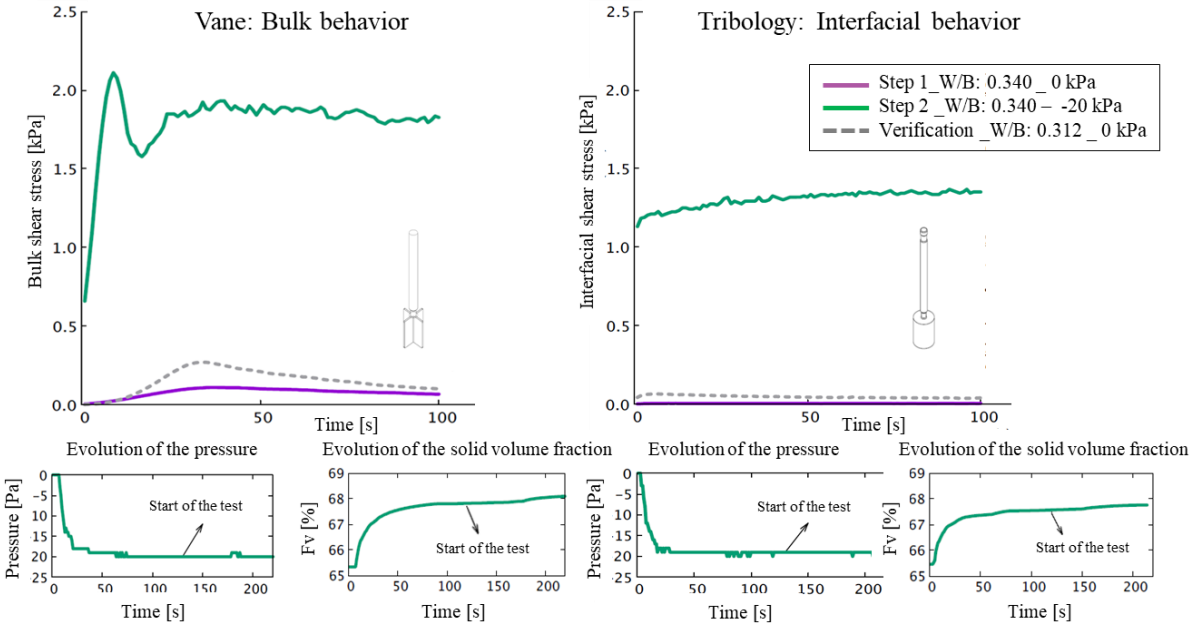

Figure 89. Verification of the effect of negative pressure with the semi-deformable device: on the left, bulk shear stress evolution as a function of time, and on the right the equivalent for the interfacial shear stress.

At atmospheric pressure, the yield stress of the material is low with both geometries (around 50Pa); under 20kPa negative water pressure, it increases to 2kPa. The verification step shows a small increase compared to step 1, but it is small enough to emphasize the effect of the negative water pressure on shear behavior. Hence, it appears that the increase in yield stress with pressure is mainly due to the effect of the negative water pressure that affects the stress acting on the particle network.

6.2 Total and effective stress

Total pressure is measured on the reference mix-design at 0, -10, -20, -30kPa with the semi-deformable and rigid membranes, and three initial air contents: 0, 3, and 10%. The effective stress can be calculated using Terzaghi's equation (*Figure 90).*

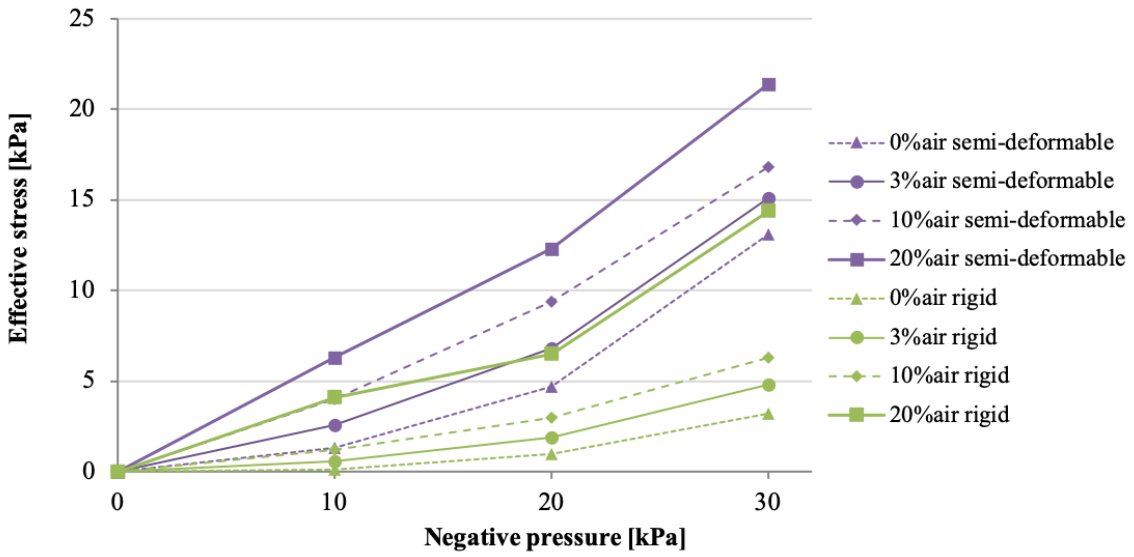

Figure 90. Effective stress as a function of the negative pressure for rigid and semi-deformable membrane, varying air content.

As shown in *Figure 90*, the effective stress increases with air content and with the rigidity of the membrane. Basically, the more sample deformation is allowed (by entrained air compression or by sample consolidation allowed by membrane deformation), the higher effective pressure is. Under negative pressure, consolidation and air volume increase (predicted by constant gas law) raise the density of the granular matrix and therefore the effective stress.

6.3 Detailed mechanisms of stress transmission phenomena- Yield stress results

a) Water pressure influence

The reference material (W/B: 0.34) is characterized at four negative pressures: atmospheric pressure, -10kPa, -20kPa, and -30kPa. The yield stresses (the difference between step 2 and step 1) are plotted in *Figure 91*. Each point corresponds to the average value of two measurements, and the discrepancy of the results is less than 7% under negative pressure and less than 1.4% at atmospheric

pressure. Note that the bulk yield stress value measured at atmospheric pressure is in line with values measured on limestone powders suspensions in the literature [100].

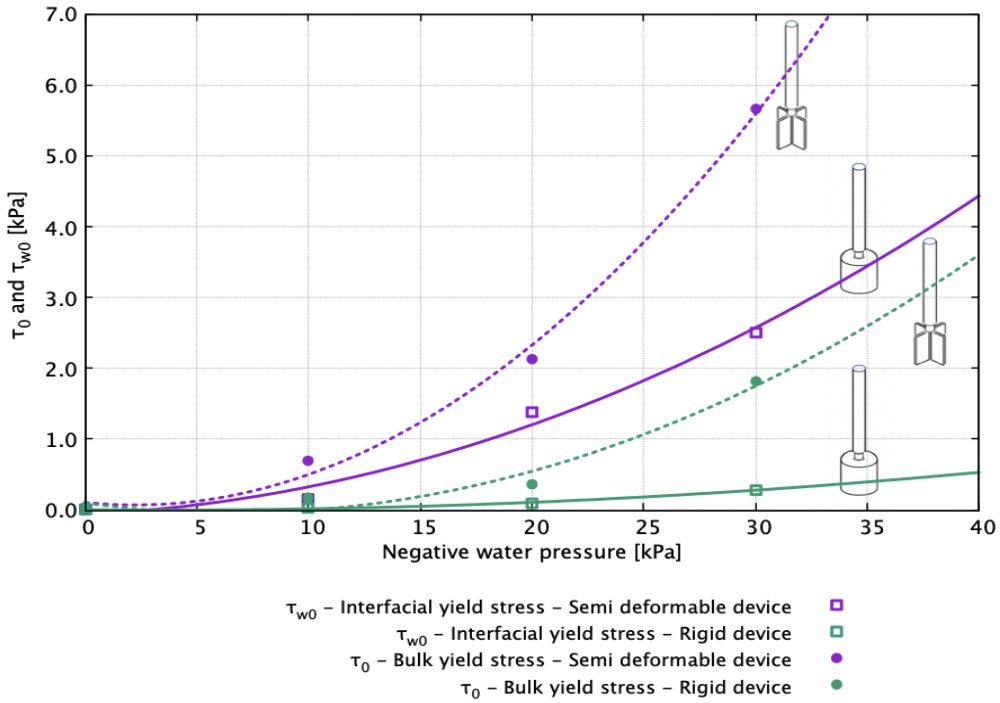

Figure 91. Yield stress of reference mix-design W/B: 0.34 as a function of negative water pressure, vane geometry in dash line, tribology in smooth line.

The yield stress increases with negative pressure and it is higher for vane geometry, which means that slippage occurs at the surface of the cylinder tool, as expected. The yield stress is higher for the semi-deformable membrane compared to the rigid device because of the effect of consolidation on the material with the deformable membrane, which tends to stress the suspension.

b) Air content influence

The yield stress is measured in both rigid and semi-deformable devices at water negative pressure of -20kPa, varying the air content (0, 3 and 10%). Each measurement is plotted in *Figure 92*.

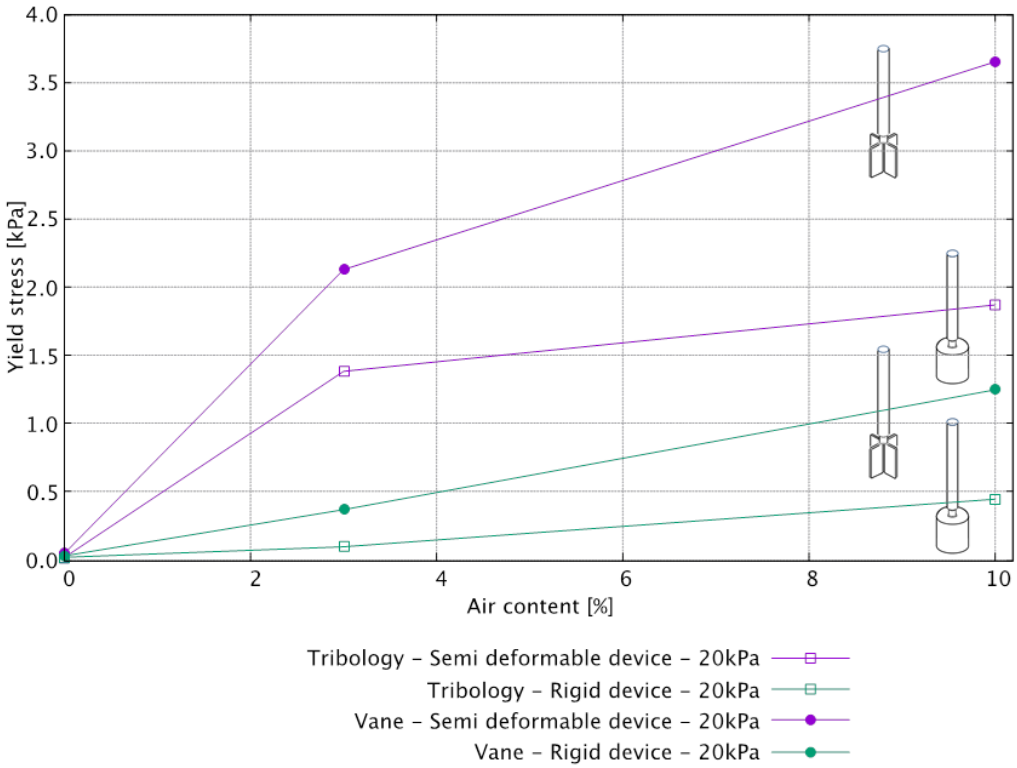

Figure 92. Influence of air content on yield stress, rigid and semi-deformable membrane, -20kPa: yield stress evolution a function of air content.

Air content increases the yield stress and 10% of air content increases the yield stress significantly for all the configurations.

Previous studies have shown that air bubbles obtained with anionic surfactants in mineral suspensions can affect the rheological properties of suspensions in a non-expected way [95] . With this type of surfactant, cement particles cover the bubbles surface creating a rigid interface. Then, at low shear rates, bubbles act as solid inclusions and then increase the bulk yield stress [101]. Moreover, the bubbles and sand particles are of the same size orders of magnitude and may interact together and may contribute to enhance granular interactions. It is also noticeable that negative water pressure will increase the size of these bubbles, according to the ideal gas law, increasing the volume fraction of inclusions (bubbles + sand).

6.4 Friction coefficient

The friction coefficients are calculated with Coulomb law. The interfacial yield stress and bulk yield stress (the initial yield stress is removed) are plotted as a function of the effective stress (calculated with total pressure measurements). Normal stress applied under the tool is taken into account because of the consolidation effect, especially for the measurements at -20 and -30kPa applied to the semi-deformable device. The bulk friction coefficient (*Figure 93*) is then 0.33 and the wall/material friction coefficient is 0.11. These values are in accordance with the literature [102]. It is worth noting that the measurement of dense suspensions friction coefficient is not so common for cement or limestone powder suspensions. Soils mechanics based tests such as simple shear tests or triaxial tests [103] [104] can be used to assess the bulk behavior of the suspensions and inverse data interpretation of drained extrusion tests can be used to evaluate the interfacial friction coefficient [105]. However, those methods work with positive pressure and have an opposite effect than the

designed device on the gas phase. The originality of this device is its ability to assess the bulk and interfacial shear behavior of dense mineral suspensions under negative pore pressure (effect on effective stress, volume variation and shear resistance).

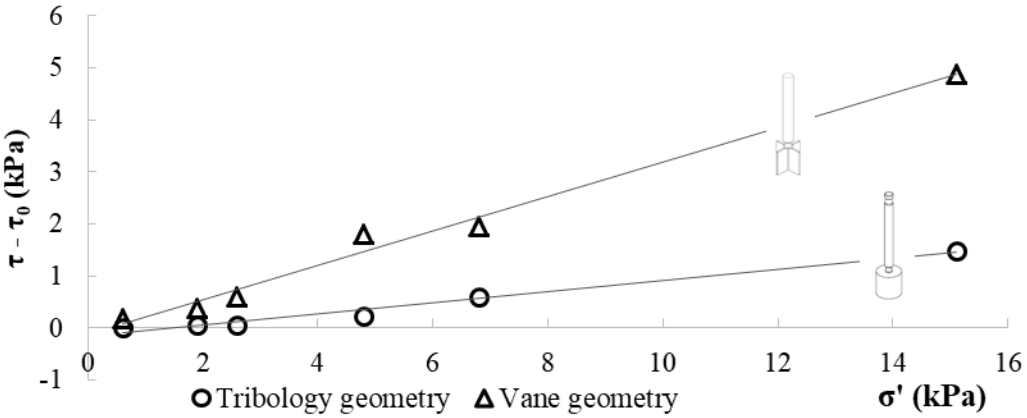

Figure 93. Friction coefficient determination: 0.33 for vane tool (r^2=0.99) and 0.11 for tribology geometry (r^2=0.98).

Hence, Eq.(21) and Eq.(22) can be written to compute yield stress as a function of the effective stress in the granular packing.

$$\tau = \tau_0 + 0.33.\sigma' \quad (21)$$

$$\tau_w = \tau_{w0} + 0.11.\sigma' \quad (22)$$

with τ_0 and τ_{w0} the yield stresses under atmospheric pressure and σ' the effective stress submitted to the particle packing.

7. Discussion

7.1 Mechanisms

The limestone-based material may be considered as a granular packing of inert aggregates that are held or suspended in a deformable matrix of liquid and air bubbles, as described for cement-based material in the literature [39]. The hypothesis regarding the mechanism under controlled water pressure, for the rigid vs. the deformable membrane, is presented in *Figure 94*.

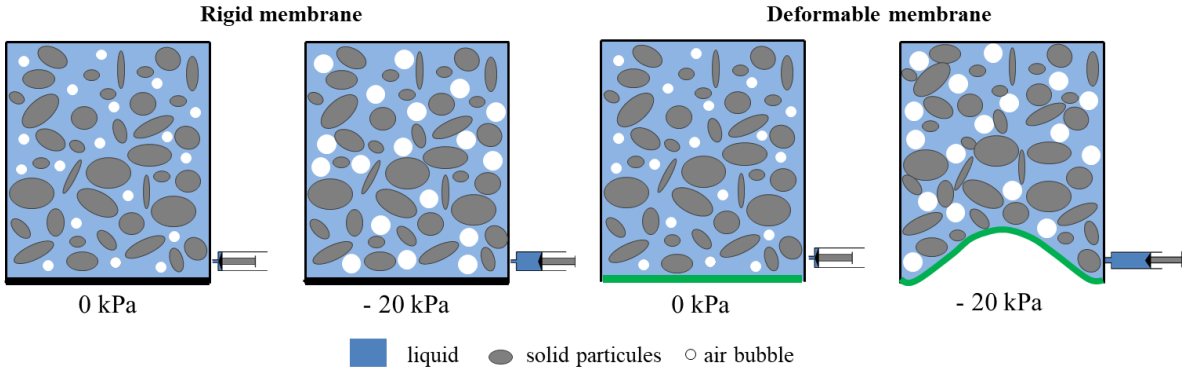

Figure 94. Mechanism of the rigid (on the left) and semi-deformable membrane (on the right) under negative water pressure.

In the rigid device, the sample volume does not change and the solid fraction remains constant. By removing water, the W/B ratio decreases and the sample pressure decreases; thus, the volume of the air bubbles increases.

In the deformable device, the water volume that is removed implies a volume reduction depending on the rigidity of the membrane. Under atmospheric pressure, solid particles seem to be suspended. Then, when the water pressure becomes negative, the particle network is strengthened. When percolation is reached, the particles are pushed together to form chains and increase the particle friction force [106]. Therefore, the effect of entrained air can be important because the volume of air bubbles increases. As observed on the sample, the bubbles size distribution stands around 500µm. This means that the pressure of the air bubbles is the same as the water pressure, as Young-Laplace capillary forces are negligible considering the meniscus radius. Thus, the air bubbles play the role of expansion cavities. When the initial air content increases, this phenomenon is amplified.

The volume variation is plotted as a function of the effective stress in *Figure 95*, in the controlled pressure device of the present work as from odometric measurements. The slope of the two curves is comparable, showing that the compressibility of the material is a driving parameter and that its compressive behavior is the same under positive external pressure (odometer) and under negative pore pressure (the device used in this study).

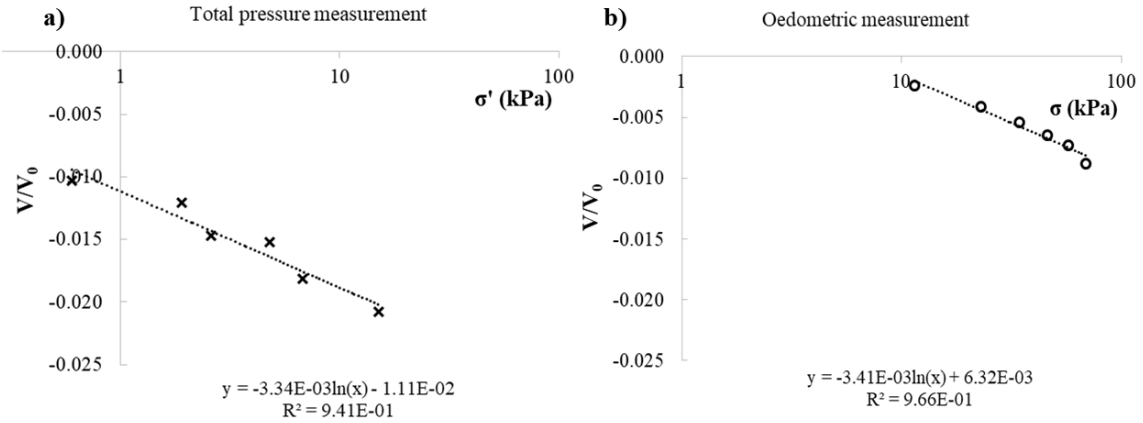

Figure 95. Comparison of a) controlled pressure device and b) odometric measurements: evolution of the volume normed by the initial volume as a function of the effective stress on the left, and as a function of the total stress on the right.

7.2 Water pressure participation to yield stress increase and modeling

At atmospheric pressure, yield stress and interface yield stress for different W/B ratios are determined (*Figure 96*).

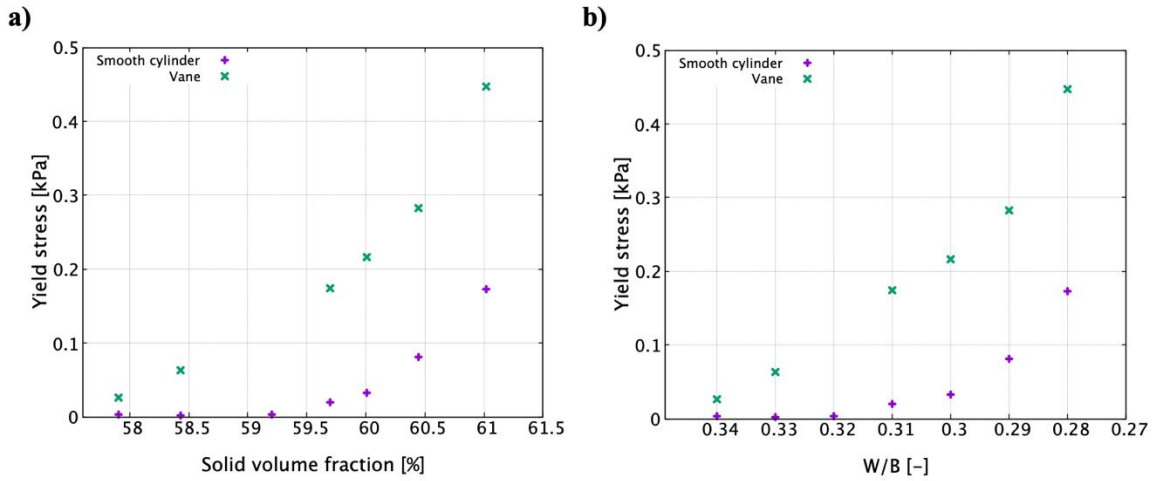

Figure 96. Yield stress and interface yield stress evolution at atmospheric pressure for mix-design from 0.28 to 0.34 W/B ratio, rotation speed 0.01 rad/s.

Low W/B ratio mixes are difficult to prepare due to the rigidity of the material. Thus, the evolution of W/B is determined in order to extrapolate the low-W/B-mix-design behavior with an exponential law (Eq.(23) and Eq.(24)).

$$\tau_w = 5.10^{11}.e^{(-78{,}36\,.[W/B]_{recalculated})} \text{ for tribology geometry} \quad (23)$$

$$\tau = 9.10^{7}.e^{(-43{,}07\,.[W/B]_{recalculated})} \text{ for vane geometry} \quad (24)$$

These equations enable calculation of the equivalent yield stress provided in *Table 15*.

It can be noted that an attempt has been made to use physically-based modeling such as the Yodel to study the yield stress of the limestone in water suspensions [41] coupled with the Mahaut et al. modeling to capture the effect of sand (non-colloidal particles) [88] However, higher numbers of required modeling parameters and worse prediction accuracy of the physically-based modeling made empirically based-modeling approach more efficient. It is also important to notice that predictive modeling of the yield stress of the suspensions is beyond the scope of this study.

The participation rate ζ is defined in Eq.(25) and assesses the effective participation of negative pressure on the yield stress level.

$$\zeta = (\tau_{measured} - \tau_{predicted})/\tau_{measured} \quad (25)$$

Table 15. Pressure participation to yield stress increase in the pressure-controlled device.

		Cycle 1: 0kPa		Cycle2: water pressure			Check	
		W/B ratio	**Yield stress [Pa]**	**Water pressure**	**Recalculated W/B**	**Yield stress [Pa]**	**Predicted Yield stress [Pa]**	**Participation rate ζ [%]**
Tribology geometry	**Semi - deformable**	0.346	3.1	-10 kPa	0.316	147	**9**	94 %
		0.346	3.0	-20 kPa	0.306	1384	**19**	98 %
		0.346	3.1	-30 kPa	0.282	2513	**127**	95 %
	Rigid	0.346	2.6	-10 kPa	0.333	4	**2**	46 %
		0.346	2.5	-20kPa	0.300	99	**31**	68 %
		0.346	2.7	-30kPa	0.276	385	**202**	47 %
Vane geometry	**Semi - deformable**	0.346	41.9	-10 kPa	0.319	701	**97**	86 %
		0.346	41.5	-20 kPa	0.297	2129	**250**	88 %
		0.346	42.7	-30 kPa	0.271	5657	**768**	87 %
	Rigid	0.346	41.5	-10 kPa	0.328	175	**66**	62 %
		0.346	41.8	-20kPa	0.306	370	**170**	54 %
		0.346	41.8	-30kPa	0.273	1809	**704**	61 %

ζ values are relatively high, regardless of the rigidity of the box. This result confirms that the effect of negative pressure is high, even in the rigid configuration. The bubbles expansion is a parameter of the first order that significantly drives the particles contacts and the shearing resistance of the packing.

8. Conclusion of chapter 3

A specific and suitable device was designed to study the behavior of an inert material with the same granulometry properties as a micro-mortar under controlled pressure conditions with different device rigidities and tool geometries. The reliability of the device was fully verified. The increase of shear stress is mainly a result of the negative pressure state in the material. A complete study was conducted, varying negative water pressure, initial air content and compressibility. This study provides an efficient tool able to capture the shear behavior of dense mineral suspensions under controlled negative pressure. It helps to understand the effect of negative pore pressure on the bulk and interfacial shear behavior of dense suspensions. It provides useful information on the effect of a negative drop in pressure on the shear resistance of dense mineral suspensions.

The main results are as follows:

- The rigidity of the container has an impact on the yield stress level into the granular packing: with a soft container, a drop in pressure induces a container deformation and then a change in the solid volume fraction. Furthermore, the volume reduction of the suspension is limited by both the container and the granular packing stiffness.
- Even with a perfectly rigid container, the yield stress increase caused by negative pressure is meaningful. In this case, the air in the suspension plays a major role: air bubbles expand and it induces jamming in the packing, as if they were solid particles. They also transfer the stress from the gas and liquid phases (negative water pressure) to the solid phase (effective stress).

A perspective of this chapter would be to involve measurements with cement mortar to confirm the observations. Improving the system would entail multiplying the number of syringes in order to ensure an evenly distributed removal of water around the tool.

The negative pore water pressure has a major impact of the material shear stress behavior. The following chapter tends to measure the effect of the pressure on the device more representative of field case.

Chapter 4: Experimental approach of a moving formwork

1. Introduction

Industrial slipforming setup is very complex. Many process parameters influence the stress which is induced on the concrete. The frequency and the velocity when elevating the panels, the roll angle, may influence strongly this stress. In order to understand the key material parameters involved in the slipping resistance, a simplified device is design and tested. The objective is to measure the evolution of the interfacial behavior of cementitious materials against a steel surface during the dormant and early hydration periods. A multi-scale approach taking into account the effect of cement hydration on the cementitious material behavior at the interface between the concrete and the steel plate is proposed. The aim is to follow the evolution of the tangential shear stress on a moving interface during the cementitious material setting process.

It consists of a parallelepiped box, filled with mortar. One face of the box, attached on a traction machine, can be lifted upward and is made of a material that represents the formwork interface (*Figure 97*). In order to study the interface at the material scale, the lifting is continuous and only one layer of the material is studied. The plate and the mold are instrumented with force and pressure transducers as well as home-designed local shear stress sensor in order to measure the evolution of those physical parameters during the lifting operation while cement hydration is occurring.

The main difference between conventional formwork and largescale slipforming is the lifting operation, which means **the impossibility of using demolding agent**. Moreover, unexpected levels of friction have been reported and have led to damages on the cementitious material surface [107].

The experimental moving formwork allows to improve the understanding of the impact of suction on granular/interfacial friction and to assess its relative influence on the interfacial stress.

Then, this lab-scale device can be considered as a cementitious material's tribometer designed for the measurement of interfacial friction at very low speed in order to cover the whole setting period. For this reason, it differs with devices used for other studies dealing with cementitious material tribology [108] [109] [110].

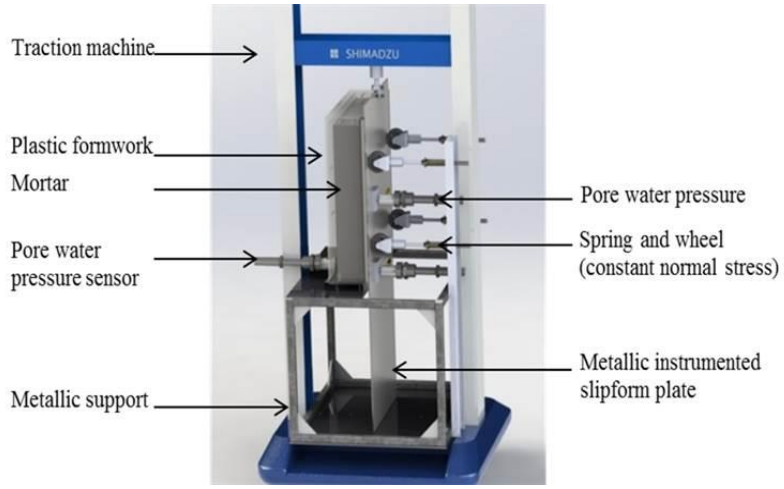

Figure 97. Illustration of the vertical shear stress device developed to study slipforming operations.

The influence of key mix-designs parameters on the interfacial stress is studied: initial air content, W/C ratio, surface tension of the liquid phase and granular arrangement. The influence of lifting speed is also assessed.

Modeling aspect of the stress on the plate is also considered, even though all the parameters are not completely over control.

2. Physical background and state of the art

In an industrial slipforming process, the formwork is in contact with concrete at different ages as illustrated in the introduction *Figure 4*. Therefore, the interface between the moving steel surface is heterogeneous whereas, it can be considered as homogeneous in the developed device. In the case of the vertical shear stress device, the lifting speed is continuous and slow, it allows studying the interface during 12 hours. As Hammer [34] described in his PhD thesis, the concrete behavior at early age can be divided into 3 stages.

The "**liquid phase**" which starts from T_0 (when cement and water are mixed together) until the concrete can support its own weight. Hammer named this point "point of self-support". In this stage autogenous and chemical shrinkage have the same evolution as seen in *Chapter 2*. It can be noted that this limit depends of the sample geometry (gravity effect will be higher for high and slender sample) and that it does not correspond to a real intrinsic material parameter but is representative of a transition in the mechanical behavior of the cementitious materials.

This stage is followed by the "**semi-liquid phase**", it lasts until significant stiffness starts to develop; this corresponds to the initial setting time. At the beginning of this stage, the pore water pressure starts to decrease. He considered that this phase coincides with the time when the concrete can be brought back to liquid phase with agitation.

The third stage is the "**early hardening phase**", it is from final setting-time to the following few hours. In this phase the concrete gains resistance and is hardening.

The developed device aims to capture the interfacial behavior during all these three stages with cementitious material going through the dormant and setting periods. Therefore, this chapter focuses on friction during all those stages. The friction is the resistance to the flowing.

In this section, first tribological measurements on concrete is described, then the influence of the surface roughness of the formwork on the concrete surface is developed, then a formwork pressure approach on conventional formworks. In the literature, granular packing and air content are known to modify friction. At the end of the bibliography part, stress distribution models such as the one developed by Janssen are presented [111].

2.1 Concrete interfacial behavior

a) Tribological behavior of concrete

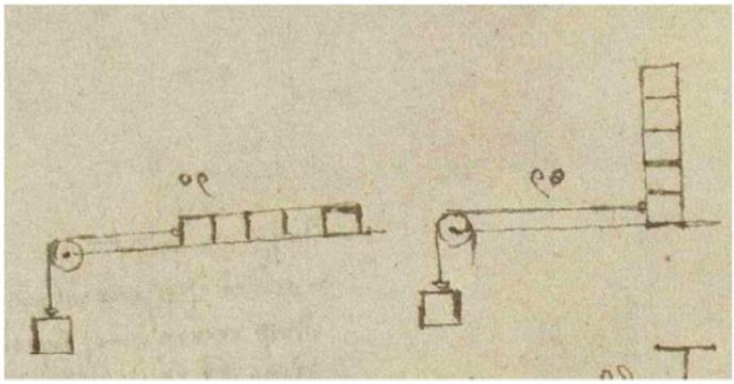

Figure 98. Sketches illustrating the effect of contact pressure or contact area friction [112].

In 1493, the drawing of Leonardo Da Vinci on *Figure 98* presented in the literature by Hutchings [112] illustrates that the force of friction is independent of the apparent contact area. This sketch was accompanied by a written statement "you will find such effort in the motion made by small and heavy contact, as in that made by a large and light contact".

The concrete at the interface is exposed to high shear stresses. Internal friction depends on the shape of the particles, size distribution, solid fraction and friction coefficient of particles [107]. In the literature most tribometers were developed in order to predict pumpability pressure as presented in the early works of Best and Lane (1960) [113] who developed a tribometer validated with pumpability trials. The device consists of a hydraulic cylinder that pushes the concrete inside a pipe with a reduce diameter. It is quite close to the concept of the Sliper tribometer recently developed by Schleibinger [114].

Morinaga (1973) [115] developed a tribometer based on real conditions of pumpability. Kaplan (2000) [2] in his PhD thesis developed a predictive model for two phases concrete pumpability. Chapdelaine (2007) [116] developed a tribometer with which it is possible to test different surfaces as rubber and steel, he used small blades inside the concrete container so that the concrete does not slide during the test. The aim was to link the results with pumpability. *Figure 129* illustrates Ngo tribometer (2007) [117] and the different steps during analysis.

Figure 99. Pictures of tribometer developed by Ngo [117].

Other types of tribometers have been developed in order to assess the effect of normal forces on the interfacial shear stress in order to model the pressure acting on formwork or to model the extrusion of

firm cementitious materials. The tribometer designed by Djelal [110] consists of a plate that is moving against a box filled with concrete and the one designed by Mélinge [108] of a rotating plate that slides against a box filled with materials. In both cases, the authors have shown that under given conditions of age and solid volume fraction, cementitious materials can exhibit a pressure dependent Coulomb-like behavior.

b) Pressure dependent frictional behavior

Coulumb friction can be evaluated by **Casagrande test**; it is represented on *Figure 100*. It is usually used for soils characterization. The material is placed inside the box; this last one is composed of two boxes which allow shearing of the material at constant speed. Normal stress is applied on the material before testing. The shear stress of the material increases until a maximal value, which is called the shear strength. Different normal stress can be applied in order to determine cohesion criterion (static yield stress without normal forces) and friction coefficient. A vertical comparator allows measuring the height variation of the sample (dilatancy or contractancy). It is important to note that dilatancy is a sign of a densely packed granular material.

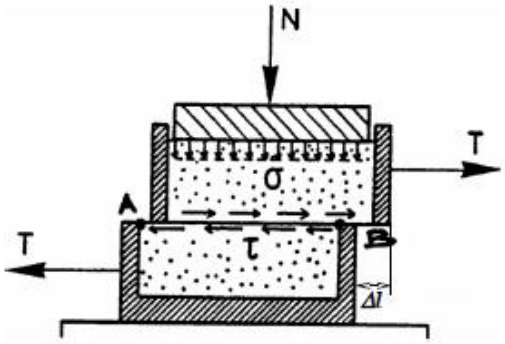

Figure 100. Illustration of Casagrande device.

Friction coefficient μ [-] is defined (Eq.(26)) as the ratio between interfacial friction stresses and normal stress.

$$\mu(t) = \frac{\tau_w(t) - \tau_{w0}(t)}{\sigma(t)} = \frac{\Delta\tau_w(t) - \Delta\tau_{w0}(t)}{\Delta\sigma(t)} \quad (26)$$

According to soil mechanics, two friction coefficients can be defined and depend on the apparent behavior (taking into account the total normal stress) and the behavior of the solid network that is responsible for the friction stress (taking into account the effective stress as defined by Terzaghi). Therefore, there is a need to distinguish the effect of the solid network to the one of the interstitial liquid phase.

As illustrated on *Figure 42* of *Chapter 2* and following Terzaghi's assumption, the effective stress is the average grain to grain pressure and can be calculated from the total stress and interstitial fluid pore pressure.

The effective stress is pushing on the area A whereas the water pressure acting where the water network is continuous that means subtracting the granular contacts area (A-Ac).
The force of the pore water pressure is expressed in Eq.(27).

$$F_{uw} = (A - A_c).u_w \quad (27)$$

The force of the effective stress is expressed in Eq.(28).

$$F_{\sigma'} = A.\sigma' \quad (28)$$

The normal force is expressed in Eq.(29).

$$F_N = F_{uw} + F_{\sigma'} \quad (29)$$

This gives Eq*(30)*.

$$F_N = (A - A_c).u_w + A.\sigma' \quad (30)$$

The effective stress is described in Eq.(31).

$$\sigma' = \frac{F_N}{A} + uw.\frac{A - A_c}{A} \quad (31)$$

And A_c is considered to be very small compared to A even when A_c will increase with hydration [1], thus Terzaghi's equation can be written Eq.(33).

$$\sigma' = \sigma - u_w \quad (32)$$

When the behavior of the solid particles network is considered, *Eq.26* can be rewritten considering the effective stress (Eq.(33)).

$$\mu'(t) = \frac{\tau_w(t) - \tau_{w0}(t)}{\sigma'(t)} = \frac{\Delta\tau_w(t) - \Delta\tau_{w0}(t)}{\Delta\sigma'(t)} \quad (33)$$

In soils mechanics, this friction coefficient is equal to tan(ϕ') where ϕ' is the so-called drained angle of friction that depends on the intrinsic behavior of the granular skeleton.
If the apparent behavior of the material is studied, as in Eq.(26) the friction coefficient μ is equal to tan(ϕ_u) where ϕ_u is the instantaneous apparent so-called undrained angle of friction of the material.

For cementitious materials undergoing hydration, the notion of drainage is not really adapted. However, it can be noted than when pore water pressure is negative (for example during cement early hydration) the effective stress pushes the particles together (because the variation of total stress is relatively low) that increases friction by transmitting the stress (water does not transfer shear stress for the considered speed).

For unsaturated materials, poromechanics concepts can also be introduced (Eq.(34)). In this case, the Terzaghi's equation is adapted using Biot [56].

$$\sigma' = \sigma - \chi.u_w \quad (34)$$

In this study, the compressibility measurements confirmed that it can be considered that χ=1 for the whole period considered during the test (12 hours after the cement/water contact).

2.2 Interaction between concrete and formwork

a) Formwork surface

Concerning moving formwork, it has been shown that the roughness of the formwork has an influence on the interfacial behavior. Kordina et al. (1990) show that static friction increases with panel roughness. Horgnies [118] also showed that surface type and roughness of the formwork influence the concrete surface roughness and the hydrates formatted at the surface.

Friction does not only depend on the formwork roughness but also on the chemical nature of the formwork because it implies different hydrates formation at the surface of the concrete as illustrated in the PhD thesis of Martin [119]. She showed that depending on composition, surface roughness, demolding way: the results are very different and concrete aspect can be shiny or mat. The main explanation is the water absorption of the formwork, the interaction with demolding agent, and the effect of formwork roughness. An absorbent formwork allows to decrease bubbles at the surface (with pressure, water movement toward the formwork allows air evacuation). The formwork is usually one of the most expensive piece for construction. Wood formwork containing sugar can delay the setting time. Formwork with controlled permeability as textile membrane can be used for art pieces for example: it drains the water. Glass has a very low roughness coefficient; capillaries forces create a water layer at the interface. Water is then reabsorbed in the paste, but there is still a very thin gap where Portlandite crystals develop, thus a shiny surface. It is like the interface between paste and aggregate but at bigger scale. With a demolding agent, capillary forces are decreased and there is no water layer anymore, this does not allow Portlandite to develop. Globally W/C and porosity at the interface are higher than in the bulk.

b) Formwork pressure

Formwork pressure has been much studied but it is also very controversy. This can be explained because concrete can display large range of rheological behavior-from self-compacting concrete to no-slump granular mixes-resulting in different types of stress distribution within the formwork. The major parameters [120] for ordinary concrete pressure exerted on formwork are vibration (because of the air decrease and because it breaks arches), rheology of concrete, speed of pouring, aggregate volume content. All these parameters are linked to concrete density. For self-consolidating cementitious materials, the structural build-up rate of the materials is the material parameter that governs the pressure acting on formwork [8].

Lateral pressure measurement is usually carried out with a pressure sensor with a membrane which is in contact with the material as described by Perrot et al. [121] (hole in the panel). The membrane is deformed by the action of the material pressure, this induces a change of the resistance on the membrane (gauge) and the tension of the sensor translates this information. For concrete, which is a hardening material, the measure can be difficult to interpret around the setting time, because the deformation of the membrane could be not reversible even if the concrete pressure decreases. Some sensors have been developed by Amziane [120] with regulation of air pressure to avoid the non-reversibility of membrane deformation.

It is well known that the thixotropic behavior for fluid concrete is at the origin of the pressure decreasing of a material after a time of rest. It has been shown by Perrot [121] and Ovarlez [8] et al. that part of the pressure decreases with the use of rebar because that helps the concrete to sustain its weight with more vertical shear surfaces during the hardening, as illustrated on *Figure 101*. In those

studies, the authors uses a Jansen's stress distribution model (without friction angle) and obtained the evolution of pressure exerted on the formwork with resting time.

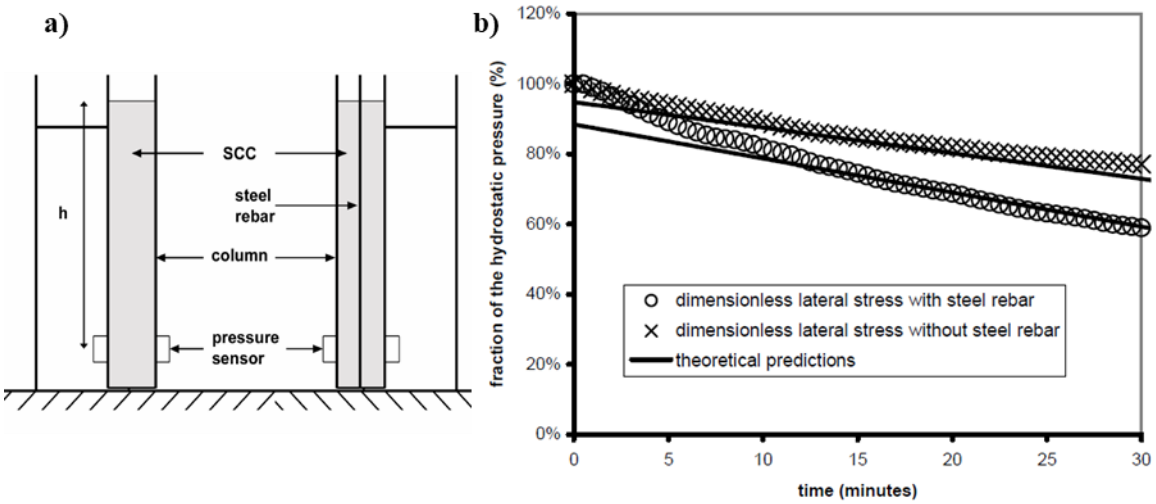

Figure 101. a) Illustration of the columns used for the measurement of the pressure on the formwork, on the left without rebar, and on the right with rebars. b) Evolution of non-dimensional pressure as a function of rest time after pouring [121].

As carried in the case of static formwork, in a moving formwork, Jansen's model can also be used to discretized in elementary slices the material in order to predict the evolution of pressure. The model is described in the literature [111], it will be used in the discussion on this chapter in order to model the evolution of the vertical stress of one horizontal slice of mortar (*Figure 121)*.

c) Comparison between the study and slipforming process

One critical disadvantage of slipforming process is the surface defects created on the surface concrete. Those damages occur when the concrete strain capacity is exceeded [4]. For Fossä, any damage is initiated when the concrete starts to lose its workability to the slipform panel and is detached from the concrete. In this period the concrete strain capacity is low.

As discussed before, during sliding water layer is formed between the moving formwork and the concrete.

In Fossä PhD thesis, the parameters affecting the friction are summarized in *Table 16*. As the process is discontinuous, he divided the friction in the static friction which is the first peak at the beginning of each movement and the sliding friction which is just after the peak.

Table 16. The parameters assumed to affect the friction as described in [4].

	Sliding friction	**Static friction**
Pore water pressure	x	x
Normal force	x	x
Movement height and frequency		x
Crushed aggregate	x	
Rough slipform panel	x	

It is really important to highlight that most of the studies of Fossä has been performed on only one layer of material and he verified on three layers that **the same tendencies were observed**. This confirms the adapted approach adopted in this chapter (one layer of material and continuous lifting).

Smart Dynamic Casting [1] is a combination of robotization and slipforming. Friction force on the formwork is crucial and the material could be submitted to the same kind of damages at the surface even if the formwork is much smaller. In this case, it is really important to link the process parameters (lifting speed and geometry) to the structural build-up and early hydration of the cementitious materials.

2.3 Effect of concrete mix-design on interfacial behavior

a) Granular packing influence on pore water pressure and rheology

The granular packing has an influence on friction because it has an influence on concrete rheology and pore water pressure. This is illustrated for example on *Figure 102*, Hammer [15] compared the pore water measurement with 5, 10 and 15% of silica fume. It is observable that the finer the skeleton, the faster the pore water pressure decreases. In the experimental part, the fineness of the skeleton will be changed.

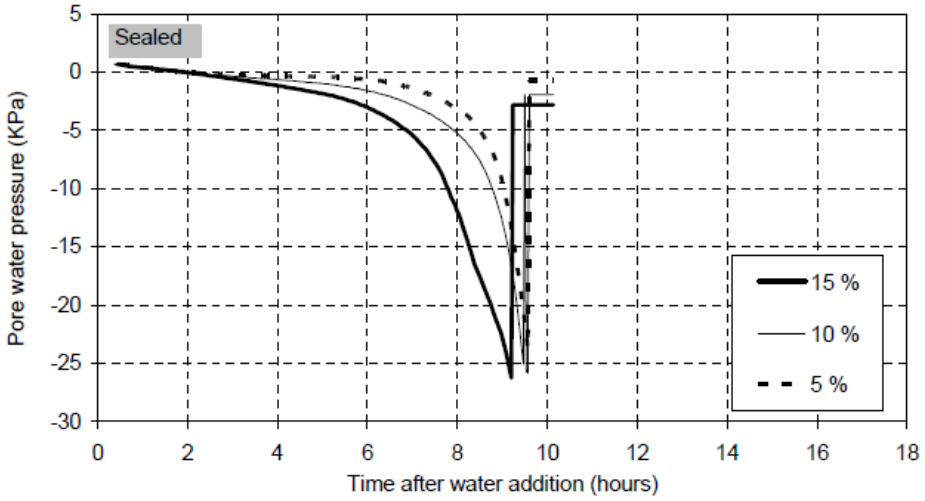

Figure 102. Pore water pressure at 50mm depth of sealed concretes with w/c=0.40 and with different amount of silica fume [34].

b) Influence of air

The influence of air on the rheology of suspension was studied in *Chapter 3*. Air plays also a role in cementitious material as seen in *Chapter 2* also, especially on friction and pore water pressure. Hammer measured pore water pressure in pastes with different air content (*Figure 103*). Globally, air seems to delay the drop of pore water pressure but it is not the cases for all mixes. This will be discussed in the following with pore water pressure. Air entraining agent delays hydration, this has to be taken into account for the analysis.

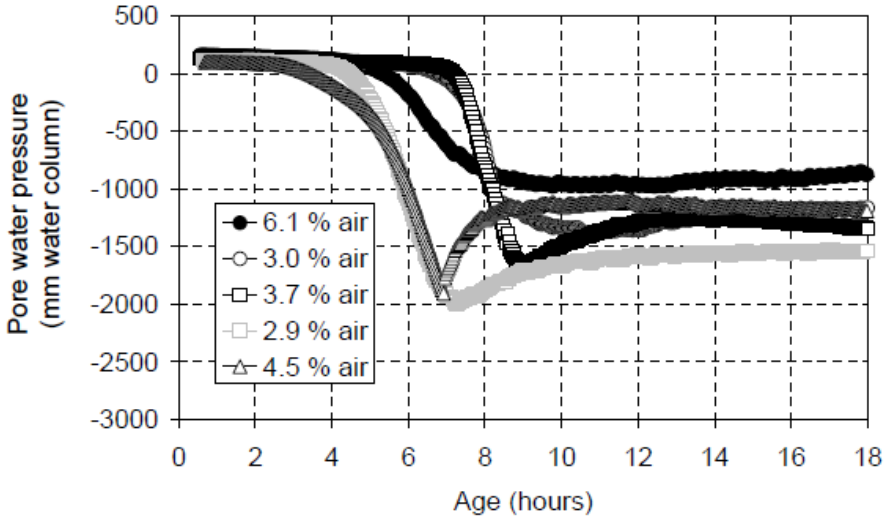

Figure 103. Pore water pressure of paste with air entraining admixture [107]as a function of time.

Fossä [4] showed that there is a relation between pore water pressure and the effective stress as illustrated on *Figure 104*.

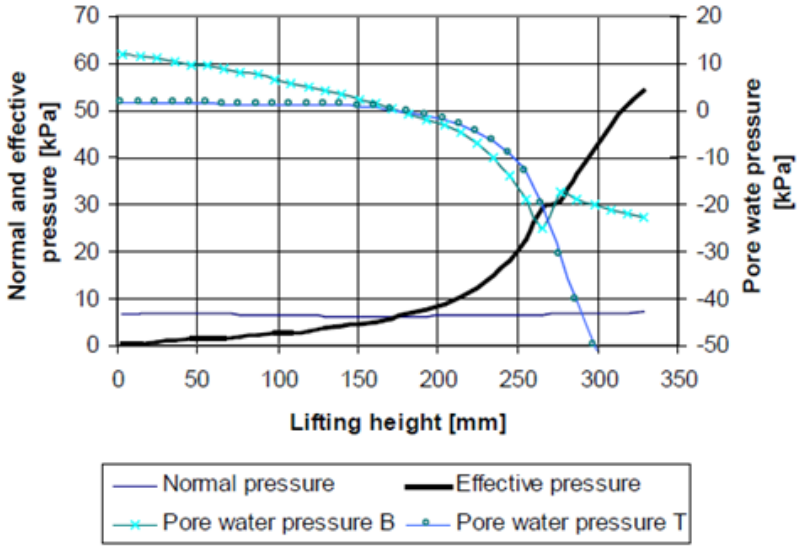

Figure 104. The effective, normal and pore water pressures measured in concrete as a function of lifting height in the device developed by Fossä [4].

3. Experimental procedures

3.1 Material characteristics

The reference mix-design is the one described in *Chapter 1*. The changes in mix-design are detailed later with varying mix-designed parameters.

3.2 Cement hydration kinetics characterisation

Hydration kinetic is followed using different devices Vicat needle penetration used for setting time determination (every 10 minutes for 90 penetrations), data acquisition of the sample temperature evolution (in 9 liters mold) and isothermal calorimetry in order to determine the hydration degree.

Yield stress with vane and smooth cylinder tool are measured with the procedure detailed in *Chapter 2*.

3.3 Device equipment

a) Device specificity

The moving formwork is a steel plate of 6mm with the roughness close to field formwork. A load cell permits to measure the global interfacial shear load and different sensors are present on the moving plate and on the mold.

The continuous lifting speed is 0.5mm.min^{-1} in order to characterize the friction during 12 hours on a 380mm course.

The spring locations were optimized before the device conception (*Figure 105*) in order to minimize the slipping plate deformation. The springs at the top are situated at 90mm from the top of the mold and the ones at the bottom at 290mm from the top of the mold.

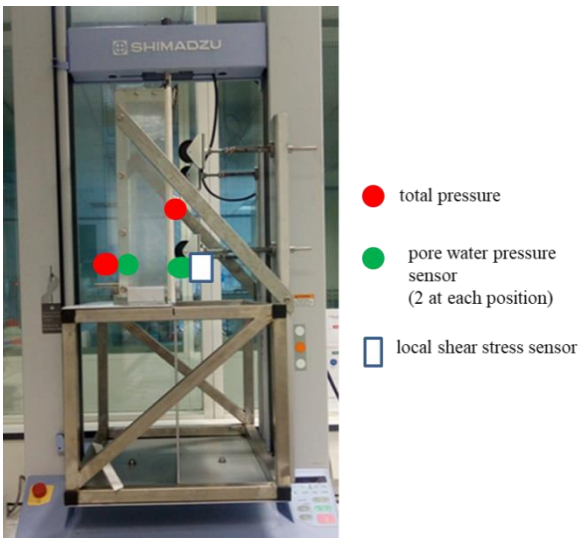

Figure 105. Illustration of the position of total pressure sensors, water pressure sensors and local shear stress sensors in the vertical shear stress device.

b) Pore water pressure sensor

In the literature, as developed in the *Chapter 2*, pore water pressure is usually measured in the bulk. It is difficult to measure the pore water pressure at the interface. Lecompte et al. [83] developed a device to measure it at the interface, but it did not permit to measure pressure above 5kPa relative water pressure due to air entry in the saturation system.

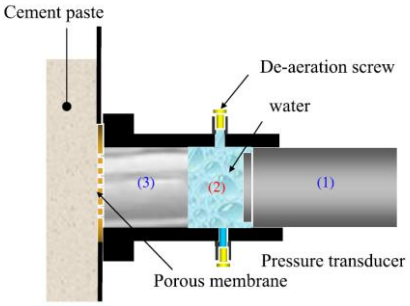

Figure 106. Illustration of the device to measure pore water pressure at the interface developed in [83].

With the developed device, pore water pressure has to be measured on longer period. It is measured along the formwork using a pressure transducer device (*Figure 107*): a tube is filled with de-aerated water (warm water de-aerated with water vacuum pump). This tube is connected to a deformable membrane fitted with strain gauges, allowing to calculate the pressure value. It allows measuring and recording positive and negative pressures up to 1bar (±100kPa). The de-aerated water tube is directly in contact with the concrete and incorporated on the surface of the moving formwork, thus it is flushed and at the interface between the mortar and the moving plate. This measurement is similar to the one developed by Radocea [66] who designed an experimental device consisting of a water-filled tubing connected to a pressure transducer. This is the first time to our knowledge that the pore water pressure is measured directly at the interface of a moving formwork.

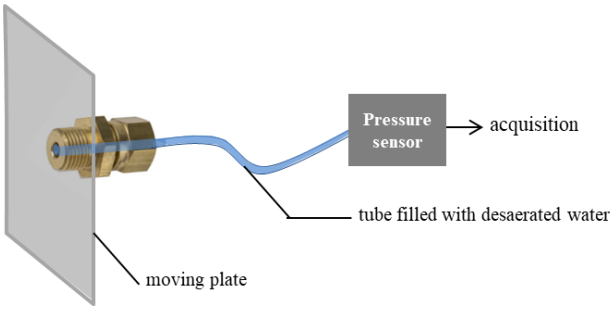

Figure 107. Interfacial pore water pressure measurement system placed on the vertical shear stress device.

Two sensors are located at the bottom of the mold and two are located on the plate. Note that they are placed at the same height at the beginning of the test. This repartition is chosen in order to see if there is any difference between the pressure at the interface on the moving formwork and on the static mold (as it is assumed in most of the literature but not measured). For each height, there are two sensors to ensure the measurements because when air comes to the sensors the signal is lost.

For each test, four curves are obtained. There is no apparent difference of measurement of the pore water pressure at the interface and at the mold regarding the scope and the moment when there is an air bubble at the sensor (and a loss of the pressure signal). The measurement is local, even if the phenomenon is global. For each measurement, a single curve is selected for better visibility, the one

that allows for the longest measurement (before air entry at the measurement point) this means the pressure on the mold or the plate indifferently.

c) Total pressure sensor

Total pressure is measured with a 250mbar pressure sensor FD8214 Ahlborn (*Figure 108*).

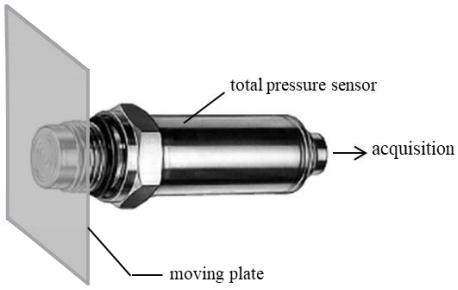

Figure 108. Interfacial total pressure sensor placed on the vertical shear stress device.

The device is equipped with two total pressure sensors: the first one is situated at the bottom of the mold (35cm of mortar above), the second on the plate at 15.5cm from the top of the mold.

d) Local shear stress measurement

An innovative sensor has been developed to assess the local shear stress and to compare it with the average shear stress obtained globally on the plate. The sensor is composed of a flexural sensor of 250g range fixed by a metal rigid square (*Figure 109*). The friction on the extremity of the sensor induce a displacement and bending of the sensor as the sensor is surrounded by a thin layer of silicon joint to avoid leaking.

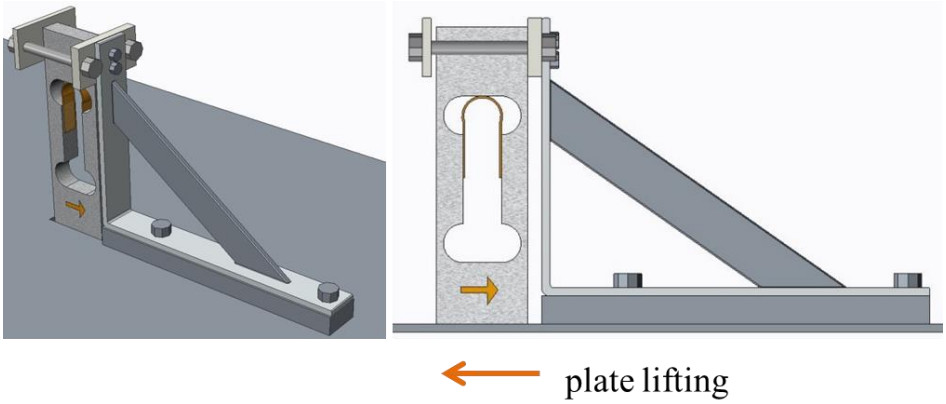

Figure 109. Scheme of the interfacial local shear stress sensor developed for the vertical shear stress device.

Calibration is very sensitive; it is obtained by hanging different masses to the extremity of the sensor before each measurement.

The position of each sensor is represented on *Figure 105*. The data acquisition frequency of the measurements is every 30 seconds. The data recording starts at 40 minutes to allow for sufficient filling time. Then, the plate is lifted at T_0+60min.

3.4 Metallic surface roughness characterization

The evolution of the roughness of the metallic plate during the experimental testing campaigns is measured with a manual roughness meter (10 times for before each test). The device gives Ra, an arithmetic mean roughness value of the individual measurements of peaks and valleys. There was not visible evolution of Ra over time. The variance of all measurements was of the order of 7.7%. Thus, the age of the plate will not be considered as an influent parameter.

The average surface roughness in Fossä PhD [4] was at the same order of magnitude (around 1µm).

3.5 Interfacial shear stress

Interfacial shear stress is determined using two different protocols with the speed and experimental protocol described in *Chapter 2*:

- $\tau_{w0,\ static}$. is measured with a smooth cylinder surrounded by the reference material every hour on a separated sample with the rheometer (this means that a new material is prepared for each measurement). This yield stress is always smaller than the bulk yield stress determined with a vane tool. It means that slipping should occur before damaging the mortar structure.
- - $\tau_{w0,dynamic}$ is determined continuously until 8 hours (the incertitude of the measurement is quite significant because there can be air between the tool and the material), their evolution is represented on *Figure 110*.

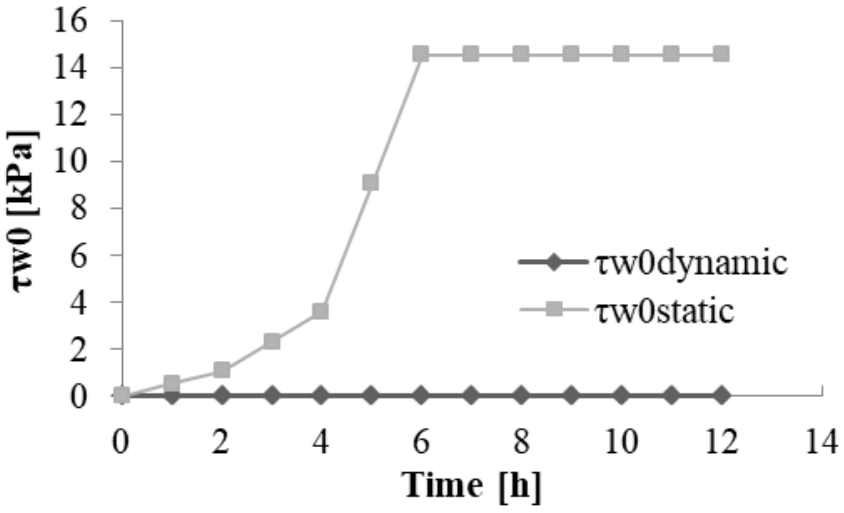

Figure 110. Evolution of $\tau_{w0static}$ and $\tau_{w0dynamic}$

It is first important to note the discrepancy between both interfacial shear stress values. As expected, the static measurements provide higher yield stress values. However, it can be noted that the measured dynamic values are surprisingly low (they appear to be 0 on the linear scale y-axis on *Figure 110*). Those measurements of dynamic interfacial values are not taken into account in this study because long duration coaxial cylinder measurement (drying, dilatancy…) may have induced an unexpected small gap between the rotating cylinder and the material

In the following, the dynamic interfacial yield stresses are considered to be a fraction of the measured static interfacial yield stress.

3.6 Influence parameters

The reference mix-design is the one used in the former chapters. *Figure 111* from Hot [94] summarized the impact of air, water, granular packing (silica fume) and superplasticizer action on rheology parameter of the concrete.

It was first observed that the average lifting speed has a very limited influence on the results. The different tested influencing other parameters are related to the material mix-design and are summarized in *Table 17*. Effects of air and water contents, surface tension and granular packing (cement substitution by ultrafine limestone powder) are studied. The initial workability (spread value) is kept constant for all tests.

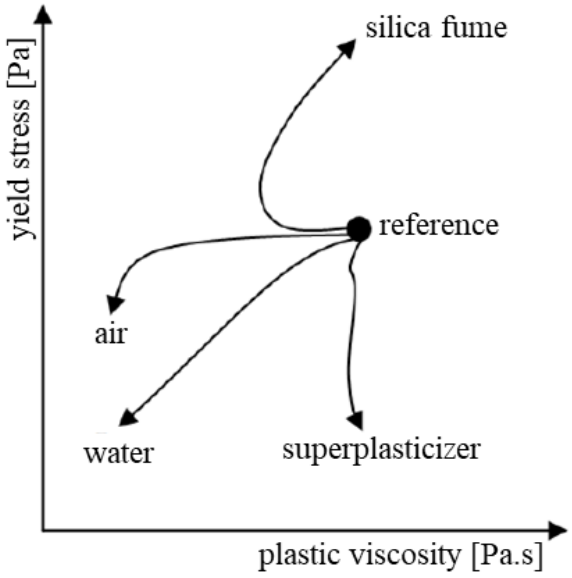

Figure 111. Illustration of the effect of air content, admixture, silica fume on the rheological behavior of fresh concrete (adapted from [94]).

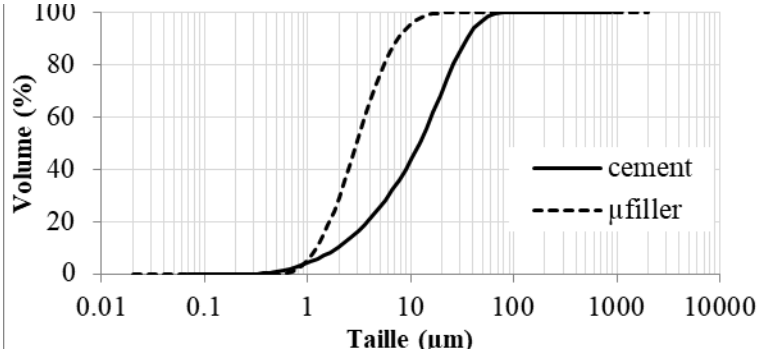

Figure 112. Particle size distribution of the cement and ultra-fine filler. 30v% of the cement is replaced with ultra-fine filler for granular packing influence tested on the vertical shear stress device.

Table 17. Description of the mix-design with the influence parameters tested on the vertical shear stress device.

	Tested parameters	Comments
Speed	Reference mix-design: **0.5mm/min** Test:**1mm/min**	No apparent influence of the speed at least for the 6 hours measurement possible with the 1mm/min. In order to maximize the time of the experience, the reference speed is kept to 0.5mm/min.
Air	Reference mix-design: **3%air** Test: **12%**	A surfactant, Master Air 104 is used to increase air content.
Water content	Reference mix-design: **W/C: 0.30** Test**: 0.36** Test: **0.45**	Admixture content is adapted to stay at same initial rheology (monitored with slump test). The admixture content and W/C ratio change both the hydration time which is not the desired effect (degree of hydration are computed).
Surface tension	Reference mix-design: **54mN.m** Test: **40mN.m**	Surface tension is decreased with a specific admixture. Centrifugation is used in order to extract the liquid after mixing. The surface tension is measured on the extracted liquid with Wilhelmy plate.
Granular packing	**"Ref":** 100 v%cement, 0 v% ultrafine limestone, 302 L efficient water for 1m^3 mortar, 0.151 w%/binder admixture **"µfiller Weff302":** 70 v%cement, 30 v% ultrafine limestone, 302 L efficient water for 1m^3 mortar, 0.107 w%/binder admixture **"µfiller Weff293":** 70 v%cement, 30 v% ultrafine limestone, 293L efficient water for 1m^3 mortar, 0.112w%/binder admixture	The granular packing is increased by replacing 30v% content of the cement with an inert ultra-fine limestone (see granulometry curve in *Figure 112).* The mix-design "µfiller Weff302" has the same water volume than the reference mix-design "Ref" but the fine limestone improves the packing that means there is more "free" water, thus admixture content can be decreased. Therefore, another mix-design is tested with less water "µfiller Weff293". Rheology of the mixes is adapted with the admixture content to obtain constant slump.

3.7 Verification of the device

a) Empty test

The tensile machine allows measuring total tangential shear stress on the plate. It corresponds to the sum of the shear stress on the plate due to the joint and the shear stress on the plate due to the material τ.

An empty test is performed in order to get the shear stress due to the joint. It will be then subtracted to all measurements with the material. The tension on the springs is adjusted to produce the same counter-effort than the material (when hydrostatic pressure is assumed). To determine the tension on the spring, the plate is separated in two: two springs at the top and two at the bottom represented in *Figure 113*.

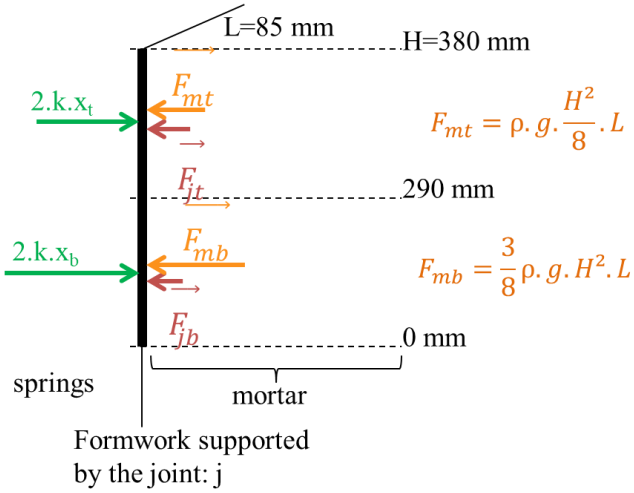

Figure 113. Representation of the division of the formwork and the applied forces. F_{mt} and F_{mb} are the material force (assuming hydrostatic pressure) situated respectively at the top and the bottom, F_{jt}, F_{jb} the force of the joint situated at the top for the empty test carried out on the vertical shear stress device.

At the top:

$$F_{mt} + F_{jt} = 2.k.x_{mt} \tag{35}$$

$$x_{et} = x_{mt} - \frac{\rho.g.L.H^2}{16.k} \tag{36}$$

with x_{mt} the elongation of the spring at the top with the mortar, x_{et} elongation top empty, F_{mt} is the material force situated at the top, F_{jt}, the force of the joint situated at the top.

Thus at the bottom:

$$x_{eb} = x_{mb} - \frac{3}{16.k}.\rho.g.L.H^2 \tag{37}$$

with x_{mb} the elongation of the spring at the bottom with the mortar, x_{eb} elongation bottom empty

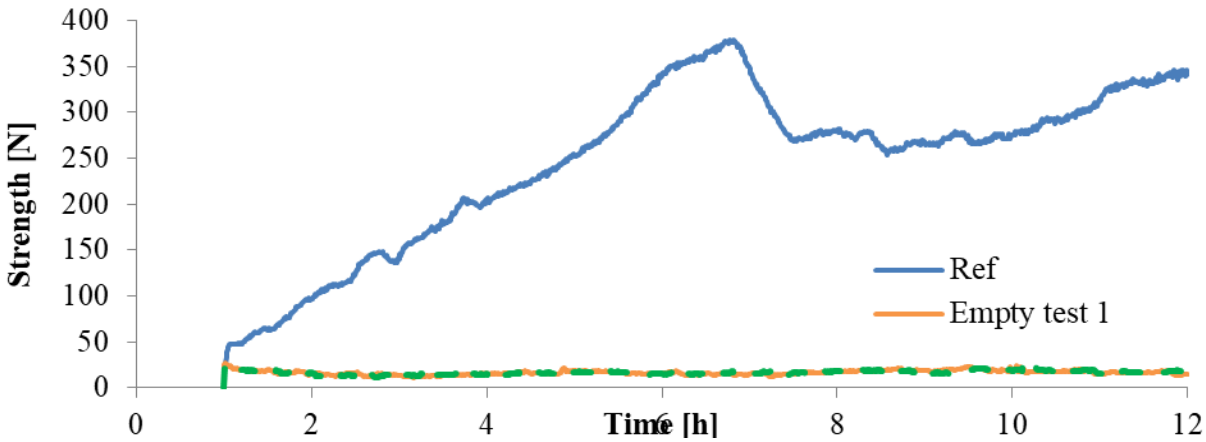

Figure 114. Plot of the empty test comparing to the test on the reference mix-design: evolution of the strength recorded with the vertical shear stress device as a function of the 12 hours test.

The strength of the spring represents a small amount of the total signal of the material (*Figure 114*) but not negligible at the very beginning; it is removed from all tests.

b) Test with an inert suspension

The cement is replaced by limestone in order to test the device and sensors. The friction of the joints is measured with the empty mold; then, friction on a material without cement (particle size distribution of limestone is shown in *Figure 115* measured because it is supposed to provide a constant friction force (no structural build-up and hydration). This mix-design is stabilized using a Viscosity Modifying Admixture (Diutan Gum) in order to avoid sedimentation during the 12-hour test.

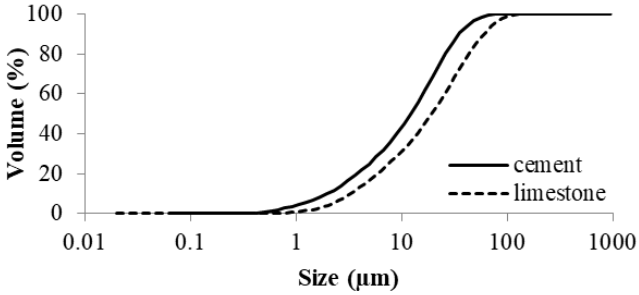

Figure 115. Cement and limestone cumulative particle size distribution curve in order to test the vertical shear stress device without the hydrates effect.

c) Terzaghi's theory validity range and total pressure sensor place choice

Before 6 hours, total pressures measured on the mold or on the plate show the same trend as one can see on *Figure 116* where the pressure normalized by the product of the gravity and the height of the sensor is plotted. In most cases, the mold pressure is more stable than the measurement at the moving interface, this is why the curve from the mold is used.

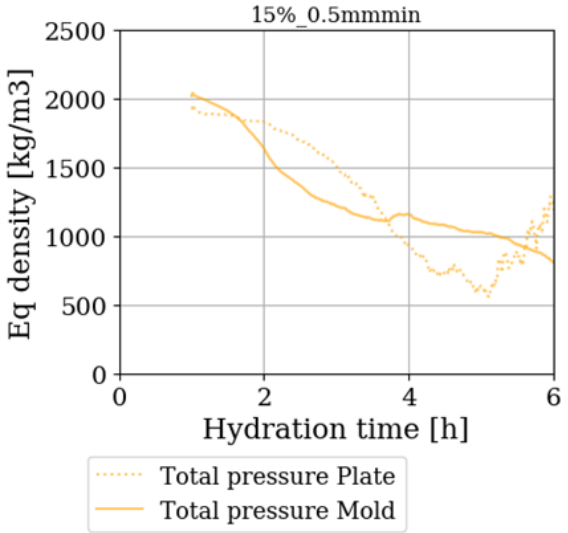

Figure 116. Comparison of the equivalent density of the pressure measured at the mold and on the moving plate on the vertical shear stress device.

After 6 hours, at one point the system will desaturate, and the validity of Terzaghi's equation has to be verified. After this time, the pressure at the mold and the plate diverge: the one at the mold decreases and at the one on the plate increases. Total pressure variations are compared to pore water pressure variation after 6 hours, to check if the total pressure can be neglected after this time.

4. Experimental results

4.1 Total tangential shear stress measurement and local shear stress comparison

The measured tangential shear stress and local shear stress are plotted as a function of the time until 5 hours (*Figure 117*).

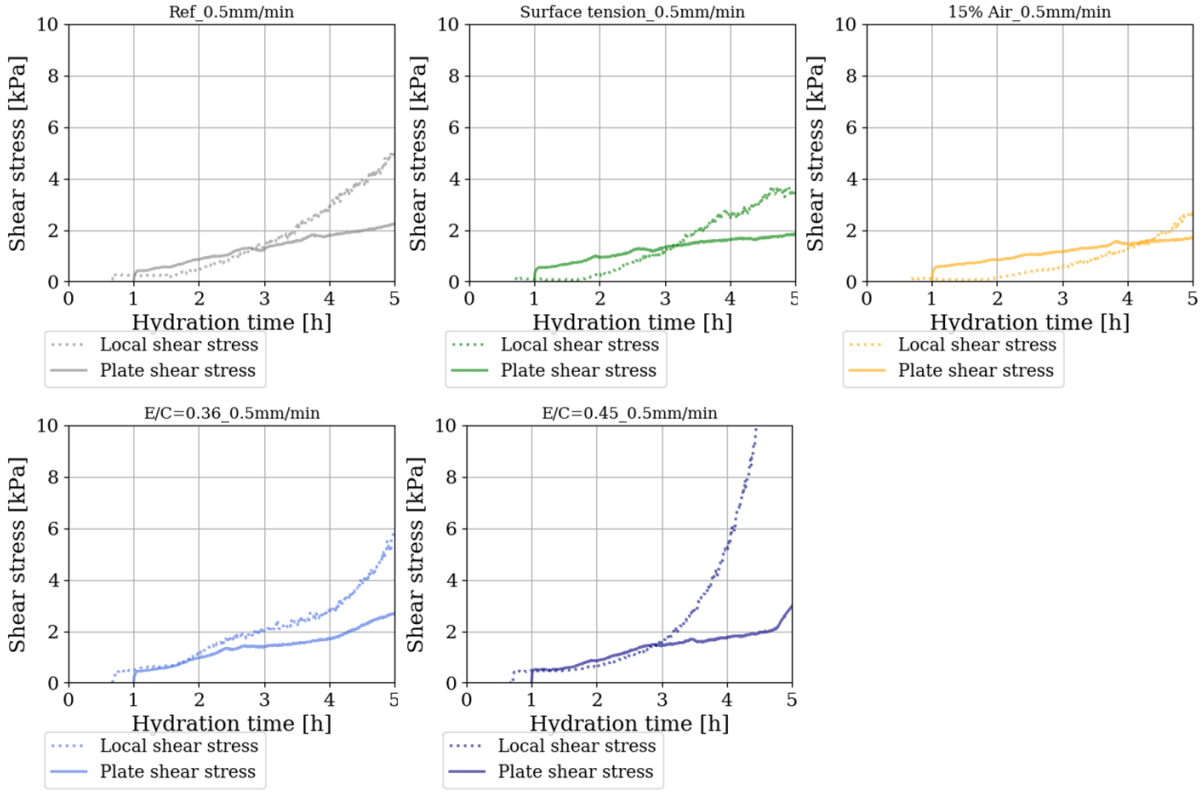

Figure 117. Local and global shear stress measurements comparison measured on the vertical shear stress device.

Local shear stress is close to the tangential shear stress on the plate during the first hours. The different of the stresses can be explained with local approach that is described in the discussion. Local shear stress can differ depending on the height of the plate. Moreover, some cement paste penetrates within the silicon joint between the sensor and the formwork. This may alter the measurements, especially when cement becomes harder with hydration.

4.2 Tangential shear stress vs effective stress

Tangential shear stress (obtained with the traction machine) is plotted with the calculated effective stress (difference between total stress and pore water pressure) as a function of the time of hydration (*Figure 118*). The setting time measured with Vicat penetrometer and the start time of temperature elevation are indicated on the graph.

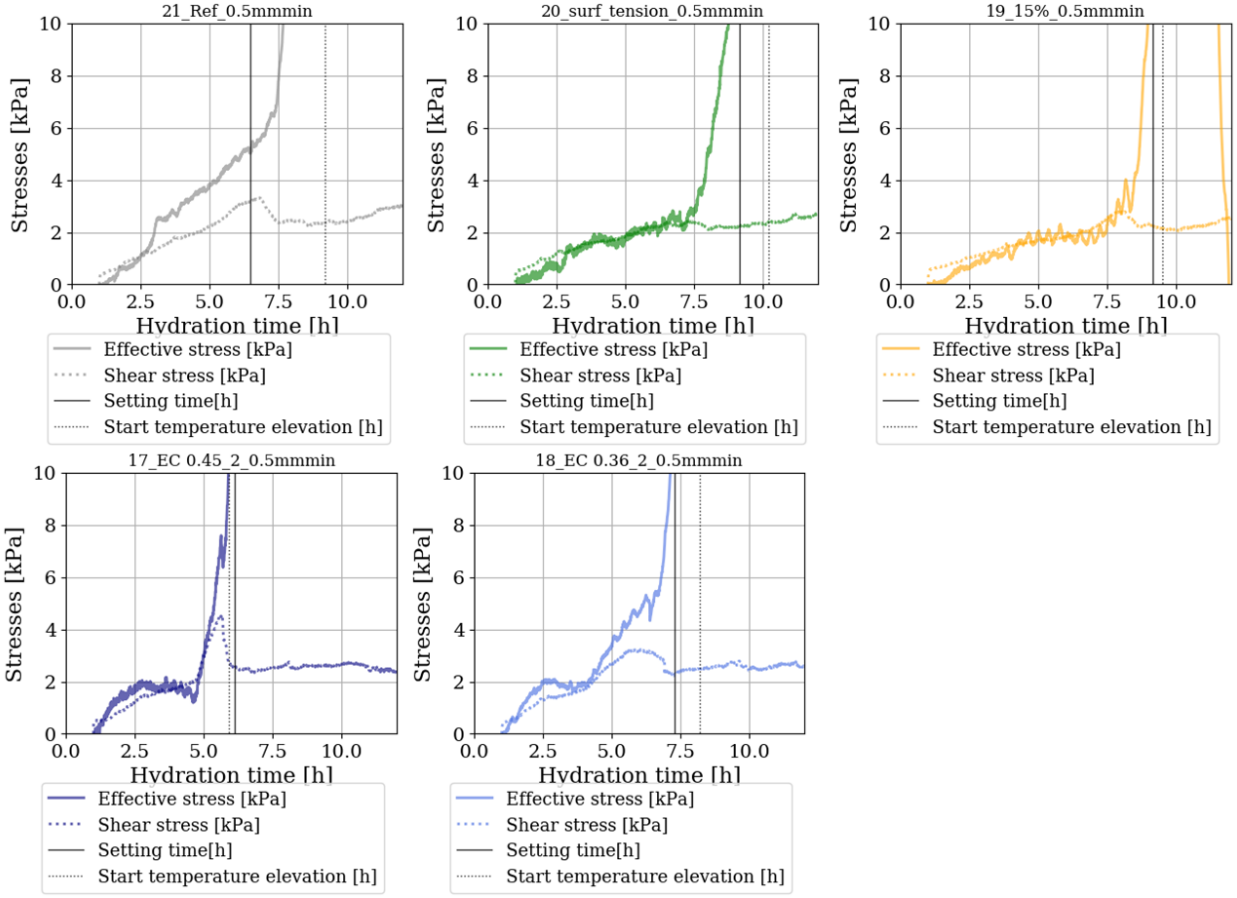

Figure 118. Comparison of the effective stress and tangential shear stress.

Figure 118 shows that the shear stress and effective stress are closely linked. The increase of effective stress is governed by negative pore water pressure which is correlated to the setting time. In field work time is the key parameter, because the faster the construction is, the better it is for industry.

A two stage evolution is clearly found. Before an age close to the Vicat initial setting time, the interfacial shear stress and the effective stress evolve in a similar manner. Such link demonstrates the role of the pressure-dependent friction at the interface between hydrating fresh concrete and moving steel interface.

However, after a critical time, both stresses diverge showing that the interfacial behavior changes. This could be attributed to the air entry on the edge of the moving plate and also to a change of the behavior of the material from liquid or semi-liquid to semi-hardening (according to Hammer). In this state, once the interface is broken, gravity and load are not high enough to overcome the material strength and constant solid friction appears.

4.3 Mix-design comparison in function of degree of hydration

In order to understand the mechanisms it is relevant to plot those tangential shear stresses as a function of degree of hydration. The degree of hydration of each mix-design is first plotted as a function of time (*Figure 116*).

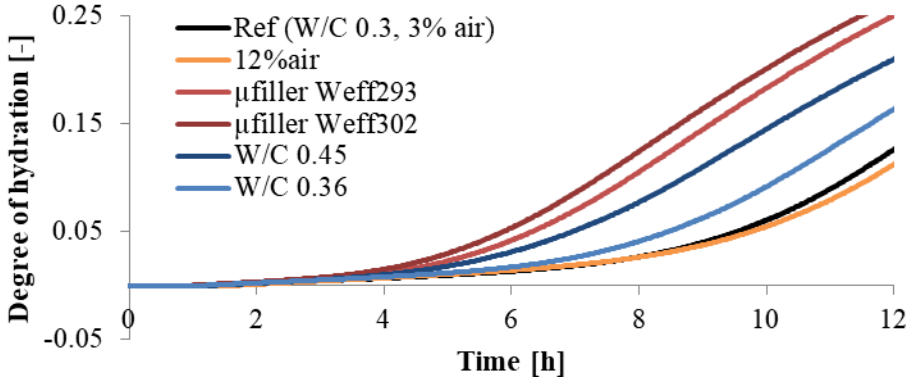

Figure 119. Comparison of degree of hydration as a function of time of the tested mix-design on the vertical shear stress device.

It is observable that the µ-filler mix-designs have a similar degree of hydration, even if there is less cement, there is less admixture (which delays hydration) and the µfiller creates nucleation sites. The increase of W/C should delay hydration, but by increasing the water volume, the admixture content has to be reduced, thus the mix-design are less delayed. Mix-design with entrained air and the reference have similar degree of hydration.

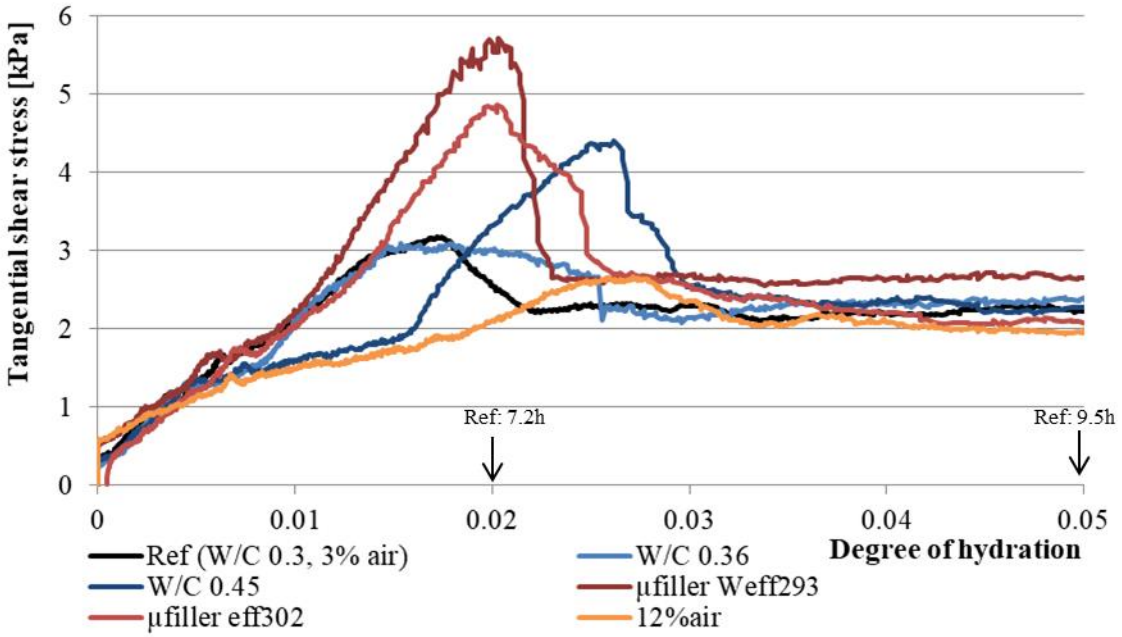

Figure 120. Comparison of the shear stress measured with the vertical shear stress device as a function of the degree of hydration.

Figure 120 is the comparison of the tangential shear stress of the different mix-designs as a function of degree of hydration. It is observable that air decreases the shear stress. The µfiller mix-

design increases the shear stress, because the microstructure is thinner (lower pore size leads to higher capillary pressure as shown in *Chapter 2*). W/C ratio effect is not clear, in the first stage, it seems to decrease the shear stress but in the second phase, shear stress has increased for W/C ratio 0.45. For completeness of the conclusion, the measurements should be repeated, and it could be very interesting to cross link those results with hindered shrinkage. This should be done in further study.

5. Discussion and modelling approach on the reference mix-design

Jansen's method is applied to the vertical shear stress device. General method is described first and then the variation and influence of the major parameters are discussed. The mortar in the mold is discretized in elementary in slices of 0.02m thick (dz). z axis is oriented toward the bottom as illustrated in *Figure 121*. The perimeter of the layer is noted P and its horizontal surface A.

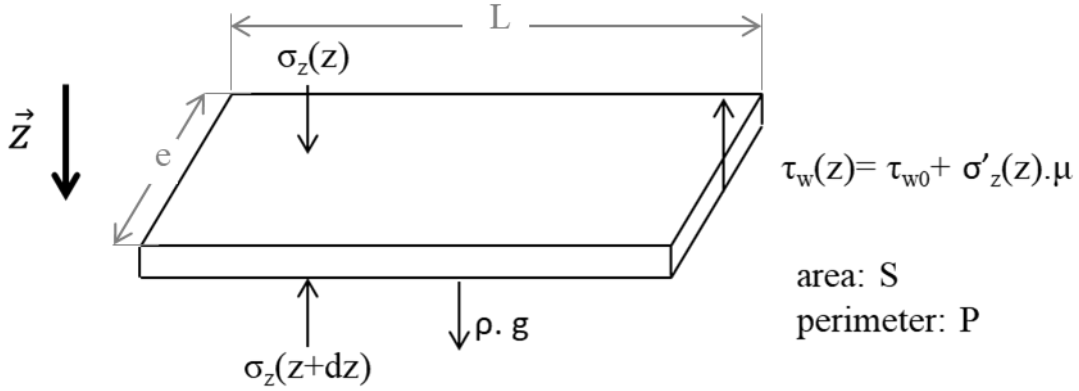

Figure 121. Scheme of horizontal slice of mortar for Jansen's model analyze.

The force balance equation (Eq.(38)) along the z axis on a single layer of thickness dz can be written.

$$\big(\sigma_z(z) - \sigma_z(z+dz)\big).S + \rho.g.S.dz - \tau_w.P.dz = 0 \tag{38}$$

The hypotheses considered are the following:

- $\sigma_{horizontal} = \sigma_z$ for saturated material and incompressible, as in the study of Roussel and Ovarlez [8].

$\tau_w(z) = \tau_{w0} + \mu.\sigma_z'(t)$ Coulomb friction plus yield stress of the material,

- All pressures are defined **relatively with respect to the atmospheric pressure:**

$\sigma_z(z=0) = 0$, $u_w(z=0, t=0) = 0$.

- $\sigma_z' = \sigma_z - u_w(t)$, Terzaghi's equation,
- $u_w(z,t) = \rho.g.z + \Delta u_w(t)$ here variations of Δu_w with respect to time are assumed to be small enough so that Eq.(38) is satisfied at any time (quasi-static approximation)
- τ_{w0} is evaluated with static tribology factor of $(2.e + L)/P$ and dynamic tribology factor of $\frac{L}{P}$

Thus, the quasi-static equation becomes Eq.(39).

$$\frac{d\sigma_z}{dz} + \frac{P}{S}.\mu.\sigma_z = \rho.g - \frac{P}{S}(\tau_{w0} - \mu\rho g z - \mu.\Delta u_w) \tag{39}$$

Thus, the solution is given in Eq. (40).

$$\sigma_z(z,t) = \left(\Delta u_w - \frac{\tau_{w0}}{\mu}\right).\left(1 - e^{-\frac{P}{S}.\mu.z}\right) + \rho.g.z \quad (40)$$

Concerning the first hypothesis ($\sigma_{transversal} = \sigma_z$) It is worth noting that the validity of this assumption can be discussed when the internal friction angle of the material increases.

Pore water pressure variation is measured on the device as explained in the device setup description. It is assumed that the vertical stress σ_z cannot become negative. This means that interfacial shear stress can eliminate the load due to gravity effect. This seems a reasonable assumption even if there is a heterogeneity of the interfacial conditions (three static walls and one moving) that can create complex vertical stress distribution within the layer.

In order to discuss the validity of the combination of these t_{w0} last assumptions, predicted $\sigma_{transversal}$ and measured $\sigma_{transversal}$ will be both used to compute the interfacial shear stress.

Among the other hypothesis, one parameter of influence is τ_{w0}, the interfacial yield stress. As described earlier $\tau_{w0,\ static}$. and $\tau_{w0,\ dynamic}$ has been determined.

In order to take into account the difference of behavior at the sliding interface and static one, the definition of $\tau_{w0,average}$ could be used (Eq.(41)).

$$\tau_{w0,average} = \tau_{w0,static}.\frac{2.e + L}{P} + \tau_{w0,dynamic}.\frac{L}{P} \quad (41)$$

However, $\tau_{w0,\ dynamic}$ measurement is difficult therefore in the following $\tau_{w0,\ static}$. is used, it is multiplied by a coefficient a_{dyn}. The value of a_{dyn} is found by adjusting the modeling prediction on the experimental data. The values of a_{dyn} are found to be less than 1.

Figure 122.a. represents the vertical stress (equals to the horizontal stress, see the first hypothesis) as a function of the height for each hour after mixing time. 0kPa corresponds to atmospheric pressure. As stated before, the vertical stress is limited to positives values. On *Figure 122.b* the horizontal force on the total plate (integral of the horizontal stress on the plate surface) is plotted as a function of time. The decrease of the horizontal force is related to the time when the t_{w0} increases as seen on *Figure 110*.

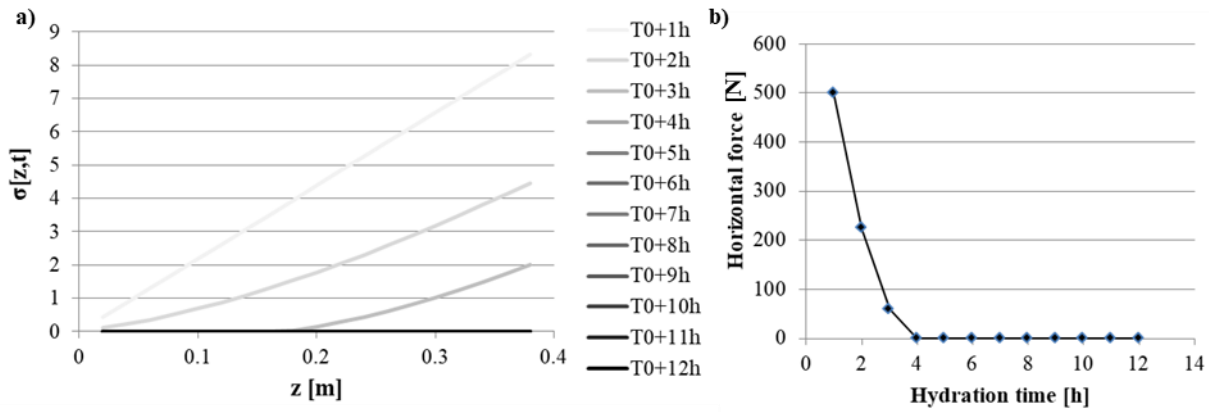

Figure 122. Horizontal stress as a function of the height for the 6 first hours and horizontal force as a function of time analyzed with Jansen model and vertical shear stress device dimensions. For the horizontal stress, after T_0+4h, all the curves are superimposed.

In the following, in order to determine the friction coefficient, the measurement of the shear stress on the plate of the vertical shear stress device is compared with $\tau_{w(z)}$ ($\tau_w(z) = \tau_{w0} + \mu.\sigma'$) calculated with the model. The model prediction is fitted on the period where the evolution of interfacial shear stress and effective stress are similar (i.e. until 6 hours). It can be seen that the model is able to capture the interfacial shear stress evolution until 6 hours. After that, the prediction provides higher values because of the vanishing of the interfacial yield stress (the material becomes elastic solid) and because of the air entry that decreases the suction effect due to the pore pressure drop.

The measurements of σ(t) can also be used to calculate σ'(t) and therefore $\tau_w(z)$. The friction coefficient should vary with time according to Mettler et al work [122]. However, it is first considered to be constant in this analysis (its impact is law at early age when pore pressure is equal to 0). These calculations depend on the ratio P/S. μ and a_{dyn} seems to be close to 0.2. It can be also observed on *Figure 123*, that both interfacial shear stress obtained with the horizontal stresses provided by the model and measured values are very close. This observation validates the assumption made with the Janssen like stress distribution modeling.

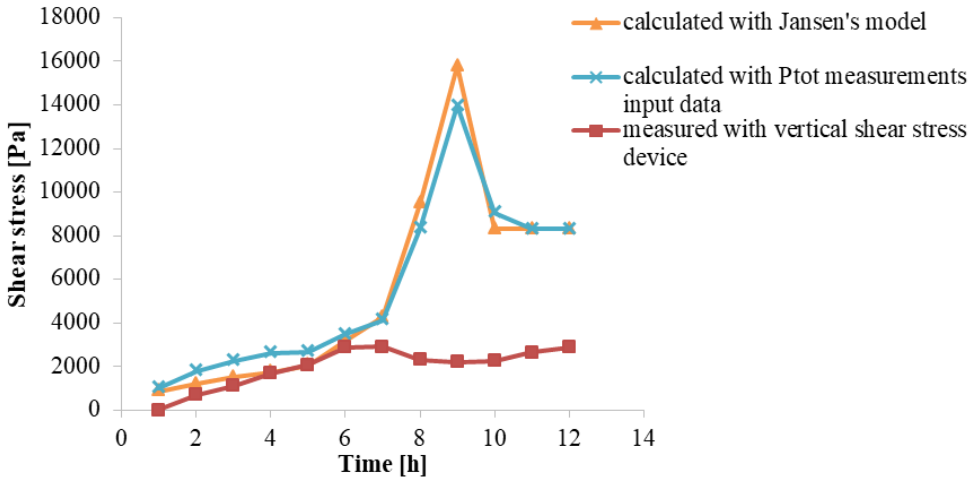

Figure 123. Comparison of the models for μ=0.2 and a_{dyn}=0.2.

A friction coefficient that varies with time can be tested in the modeling. It is chosen here to use an evolution that is close to the one proposed by Mettler et al. [122] (*Figure 124*).

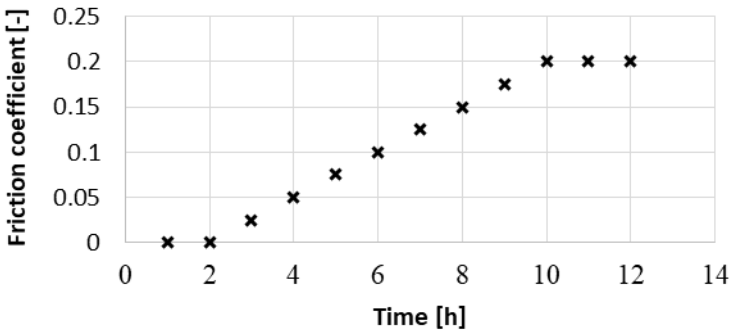

Figure 124. Evolution of the friction coefficient as a function of time.

It can be seen that the model using a varying friction coefficient provides also interfacial shear stress evolution that is in agreement with measured interfacial shear stress (*Figure 125*). The qualitative behavior of the shear stress is similar to the one with constant friction coefficient.

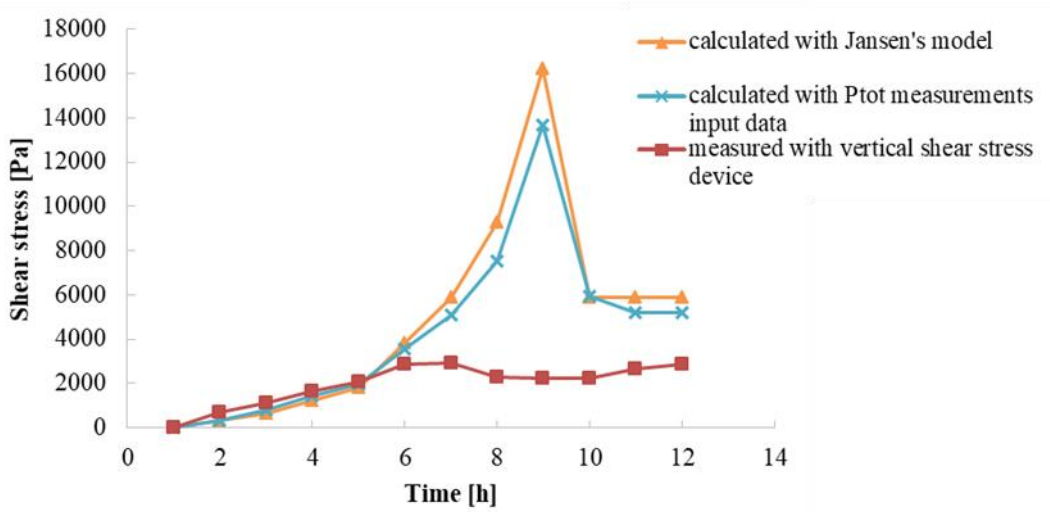

Figure 125. Comparison of the models using a variable friction coefficient.

It is interesting to note that using this variation of the friction coefficient, the determination of a_{dyn} provides a value of 0.3 that is higher than the value obtained with the constant friction coefficient in *Figure 123*. This shows that the interfacial shear yield stress is dominant over the three first hours (the friction angle is taken at 0 at this time) and that friction role increases after until the air entry at the interface.

Scale up trials were also performed at the LafargeHolcim Innovation centre. The vertical shear stress device has been used on parallel of mock up trials: concrete wall, two meters high, were slipformed (*Figure 126*). Four mixed design have been tested.

Figure 126. Slipform mock up trials illustration.

The slipformed mock-up test permits to confirm that the vertical shear stress measurements were relevant, the higher shear stresses were observed for the wall with damages. The adhesion peak appearing in the second part of measurement was usually not prejudicial for the concrete. Considering the tapered panel angle on the panel and the optimization of the process in term of lifting frequency, the concrete is generally no more in contact with the concrete at this stage, but shear stress before is important. The mock-up trails have also shown that the concrete stickiness has also an impact on the surface damages. The tests were performed inside a building, this means that the environment was controlled. In real conditions of construction site, temperature and wind can modify a lot the surface and the matrix of the material. The objective is always to limit localized adhesion.

6. Conclusion and perspectives of chapter 4

An experimental setup has been designed to study the friction behavior between cement-based materials and a moving steel formwork from fresh state to early age. It can be considered as a new-tribometer allowing to describe the interface between a given surface and the concrete at different levels of hydration. The system is equipped with sensors on the fixed mold and on the moving panel. Homemade sensors (pore water pressure at the interface and interfacial local frictional sensor) have been developed. A first modeling approach is proposed. It is based on coupling a Janssen's model with interface yield stress and a friction coefficient.

A complete study has been performed varying different mix-design parameters: water content, air content, granular packing, and surface tension.

Air seems to be the most influent parameter to decrease the friction and therefore limit surface damages, but it decreases the mechanical performances. Nevertheless, the compressive strength is rarely a limiting factor contrary to durability considerations which could be less affected by air entrainment than strength. Surface tension is also an interesting parameter to decrease friction. The increase of granular packing is harmful for the friction.

As Fossa shown, the one layer study is relevant for slipforming application. Further prospective would consist of measurements with multiples layers and a discontinuous process. It could be also interesting to use concrete in the device. The impact of fibres would be worth to try to see if there is an improving on cracks. For Jansen's modeling, developing a device with four sliding parts would be relevant as it will provide homogeneous stress conditions on the mortar contour and as sliding on the opposite way on the vertical shear stress device could be interesting. Other interesting key parameters to test would be to change the type and roughness of the moving formwork and also to test others admixtures like superabsorbant polymers.

General conclusion and perspectives

The many ways of processing concrete involve many different interface interactions. In the fresh and hardened state, physical phenomena are quite well understood. This research work aims to understand the behavior of cementitious materials at the interface during the period around cement setting. Concrete slipforming is a specific process which is directly concerned by this research topic. It allows pouring continuously concrete with an interface which starts in the fresh state of the concrete with lubricated interface, ending in the dry state with pure Coulomb friction. Usually, the vertical stress is maximal at the middle of the slipform panel where concrete is hardening. In this zone, cracks or surface damages may appear on the slipformed concrete surface and are the consequences of the concrete adhesion to the panel creating high friction and so high shear stress.

A multi-scale approach has allowed to describe the friction phenomena from the nano-scale of the hydrates, through physical consequences as pore water pressure drop and effective stress development, to the macro-mechanical observations (adhesion, friction). Finally, the description of the interfacial behavior of cementitious materials is sought in order to understand the cracks and defects formation.

This manuscript showed an attempt to make links between phenomena involved in the friction occurring at the interface between fresh to hardened cementitious materials and a steel surface. Then, a significant part of this PhD consisted of developing new devices and sensors in order to describe in the best way the phenomena and to isolate them as much as possible.

The impact of cement chemical reaction on the microstructure (pore size, volume change, pore water pressure) has first been studied. Then, the impact of those changes, especially in the stress distribution within the granular network and liquid phase, on the rheological and tribological behavior of a dense mineral suspensions has been highlighted. Finally, the mechanical behavior of the fresh-to-hardened cementitious material has been taken into account in order to predict the friction stress on a moving steel panel (to simulate part of the slipforming process). Such prediction has been compared with experimental results obtained on a dedicated, designed and developed lab-scale slipforming device.

In the first chapter, the hydration mechanisms of the tested reference mix (fluid mortar) is fully described. Using pull-off tests carried out with different surface roughness and porosity, it has been shown that the adhesion comes from the physical bounding of the hydrates to the formwork and the effect of pore water pressure. It has been shown that the contribution of pore water pressure to the shear stress is dominant with respect to the hydrates bounding effect.

Then, the origin of the pore water pressure was explored resulting in a model linking capillary pressure with the hindered shrinkage and the pore size diameter evolution in *Chapter 2*. Air volume expansion is directly linked to the hindered shrinkage. One of the main outcome is the thermodynamic model allowing to predict pore pressure even when the measurement is no longer possible. It is a key parameter to predict the granular stresses.

In *Chapter 3*, a negative pressure-controlled device has been developed, connected to a rheometer and has allowed to monitor and control the suction phenomenon and to assess its influence on the bulk and interfacial shear behavior of dense mineral suspensions without the hydrates effect (*Figure 127*).

This device allows to isolate the influent parameters. To avoid any hydrates effect, an inert material with the same granulometry properties as a micro-mortar is used to study the shearing behavior under controlled pressure conditions with different device rigidities and tool geometries. The influence of different parameters was monitored: negative water pressure level, initial air content, material compressibility and various rigidities of the container. This small device showed that the increase of effective stress and shear stress originates from the negative water pressure effect. The volume reduction of the suspension is limited by both the container and the granular packing stiffness. With the tested surfactants, air bubbles showed a solid-like behavior regarding rheological parameters and increase the macroscopic yield stress.

In *Chapter 4*, an experimental setup was designed and built, to be able to follow the evolution of the concrete interface with a plate, during this window of interest. Contrary to the industrial slipform process, which is concerned by all the concrete evolution at a given time as successive layers are poured, all the material has the same age in the laboratory setup. It allows to dissociate the effects occurring in the industrial slipform process (see *Figure 127.a and b*). In this main experimental setup, the formwork is lifted continuously in order to focus on the impact of the material independently of the process.

The developed vertical shear stress device (*Chapter 4*) and the pressure-controlled device (*Chapter 3*) have pointed out that the material has to be studied with the surrounding system. The outcome of the pressure-controlled device was that there is a competition between the material rigidity and the device rigidity. Volume variations (material and device) have a strong influence on the drop of pore water pressure and thus impacts on rheological and tribological behaviour. Therefore, this is also the case with the vertical shear stress: the material building up increases the friction on the panel. The material and the container must be study together. Futures perspectives can be drawn for the developed devices. It could be interesting to test cement-based material in the pressure-controlled device to confirm the observations. This device could also be improved by multiplying the water aspiration points in order to limit material inhomogeneities. Such system could be used at different ages of cementitious materials in order to study the change in material behavior with resting time (until the limiting torque of the rheometer).

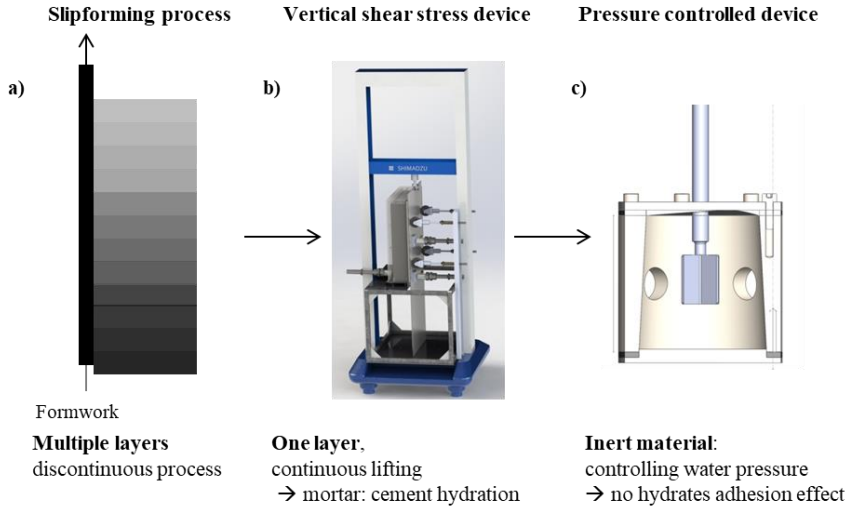

Figure 127. a) Representation of the concrete layers in the slipforming process, b) The vertical shear stress device, c) the pressure-controlled device

A complementary mechanical approach, using the pore water pressure, the interfacial yield stress and Jansen's considerations, allows to calculate the vertical shear stress and therefore the global sliping resistance of a steel surface against a cementitious material undergoing hydration. The comparison of the modeling with the experimental results demonstrates that the hydration of the cementitious material magnify the effective stress through the drop of pore water pressure, increasing friction. The combination of those models should allow to predict, in further work, the friction behavior knowing the degree of hydration, the mix-design and internal friction coefficient.

Moving from mortar to concrete, vertical shear stress device measurements have been crossed with field slipforming measurements of two meters high wall. This has confirmed that high shear stress measured on the device where linked to surface damages. However, the surface of the vertical shear stress device is too small to observe any surface damages. Thus, the measurements can only be used for qualitative comparison regarding damages predictions.

The devices have allowed identifying influent parameters to decrease shear stress. Air plays the role of expansion cavities; it reduces pore water pressure and lowers the effective stress. Surface tension reduction also allows to reduce shear stress. The different parameters as W/C ratio and granular packing change hydration time because of the water or admixture content, this is why the data where compared as a function of the hydration degree. As time is the used for field trials, there were also plotted as a function of time. The different steps of the research work and the highlights are summarized in *Figure 130*. As future prospects, it could be interesting to combine the model linking capillary pressure with pore size with drying mechanisms as it may occur during real slipforming process. It is important to note that no experience performed during this PhD has led to surface defects. Therefore, it could be interesting in further studies to test more granular mixes in order to make a link between friction stress and defects formation. In those conditions, it could also be very relevant to test the role of fibers in the vertical shear stress device to reduce surface damages. Likewise, other surface tension reducing agents can be tested as they seem to have friction reduction impact. Roughness and nature of the surface panel are also an interesting field of investigation.

All the studies carried out in that direction aim at better understanding the mechanisms to decrease friction. The industrial solution to tackle surface damages will benefit from these works and will be chosen as the most profitable.

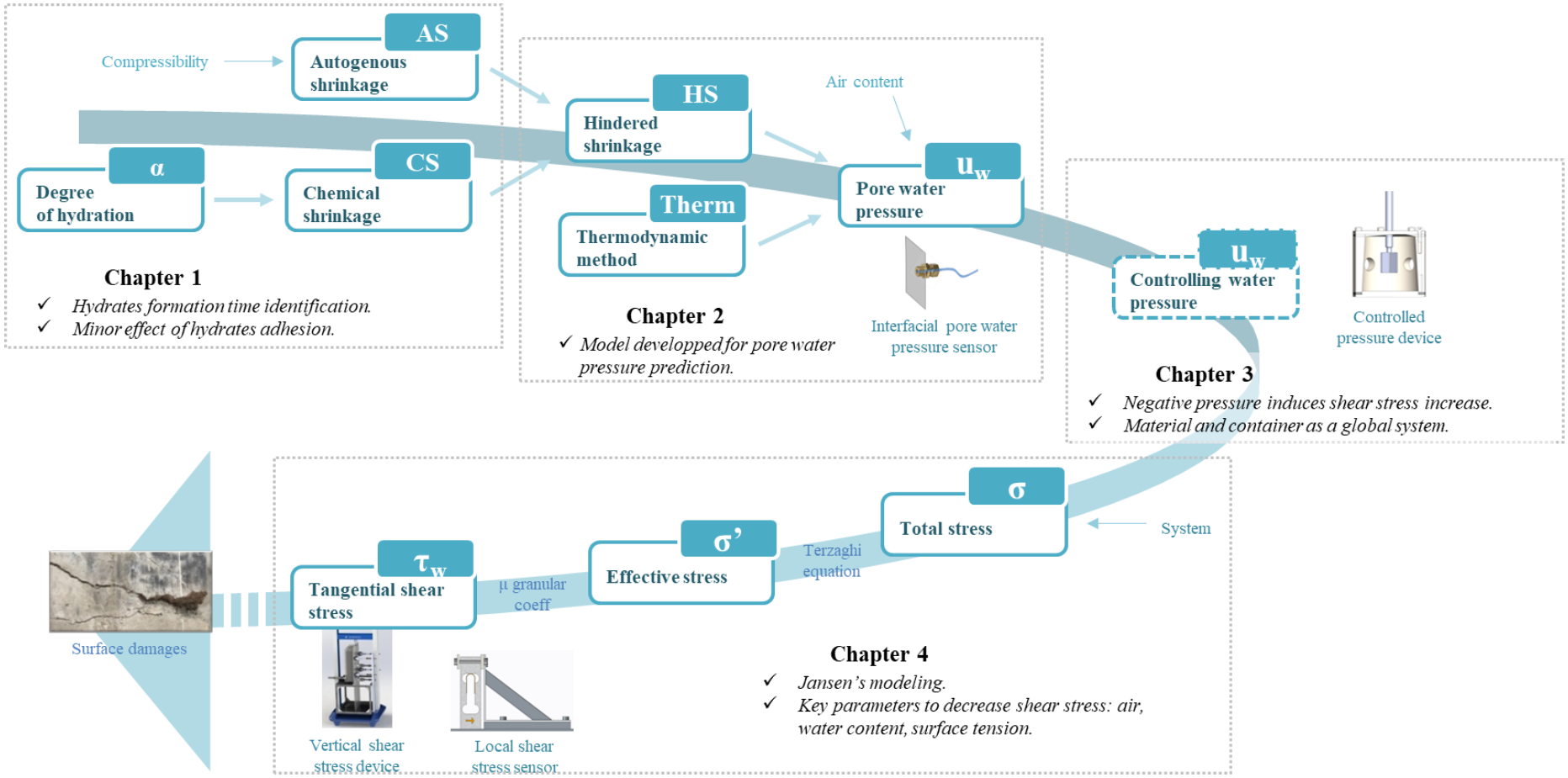

Figure 128. Summary of the research work

Appendice 1: Spectrometer Kea² 20MHz parameters

The spectrometers parameters are the following:
Frequency: 20MHz
Pulse length: 6µs
π pulse amplitude: -6dB
2 π pulse amplitude: -3dB

Quad Echo parameters
τ= 12; 15; 19; 24; 30; 37; 45; 54µs
Numbers of points: 256
Dwell: 1µs
Number of scans: 64
Repetition time: 1s

CPMG parameters
Number of scans: 1024
Repetition time: 1s
Points per echo: 16 (8used for the analysis)
Log speed min τ=30µs
Maxτ=3000 (for the first sample)
Number of echoes: 256

Figure 129. Photo of the spectrometer

Magnetic impulsion (M_0 deviation)

During NMR experiment, the sample is under a static and homogeneous magnetic field named B_0. B_0 induces an orientation of the spin parallel in most of the cases and antiparallel. The amount of the spin parallel to B_0 creates the apparition of a macroscopic nuclear magnetization named net nuclear magnetization vector M_0 which is parallel to B_0 [28]. During NMR relaxometry experiment, a radiofrequency impulsion (created by a magnetic field B_1 orthogonal to B_0) is send; the result of this is a deviation of M_0. A deviation of π angle leads to the measurement plan where the signal intensity is maximum [28]. In NMR experiments, the tipping of magnetization from the *z*-axis "equilibrium state" aligned with the external magnetic field is induced by the application of a short excitation pulse. An

additional oscillating magnetic field (B_1) is applied in direction perpendicular to the external field B_0. The frequency of the B_1 field is set to the Larmor frequency to achieve resonant interaction [27].

Figure 130 illustrates the M_0 orientation. M_z, parallel to z is named longitudinal magnetization and $M_{x,y}$ transversal magnetization.

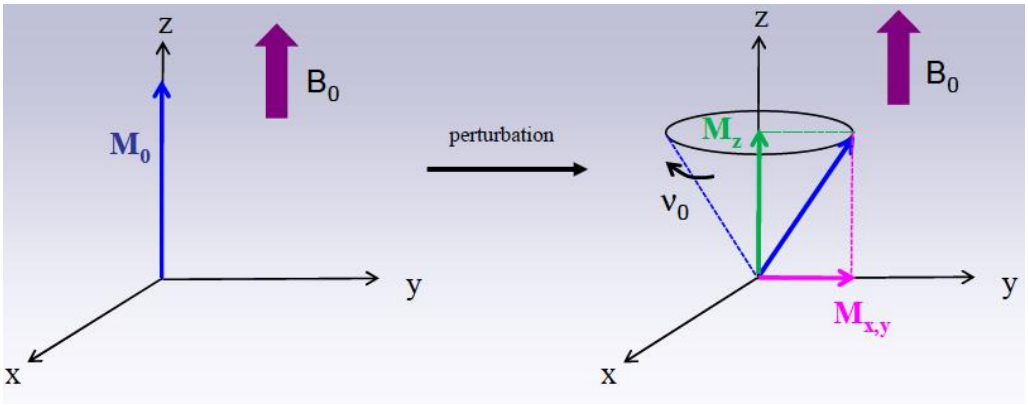

Figure 130. Larmor precession after perturbation [62]

Inversion-recovery

Usually to determine T1, an impulsion of π is send, the signal will be reinversed compared to the equilibrium state (*Figure 131*). The equation governing this magnetization recovery following a 90° pulse is:

(t)=[1−exp(−t/T1)] [27].

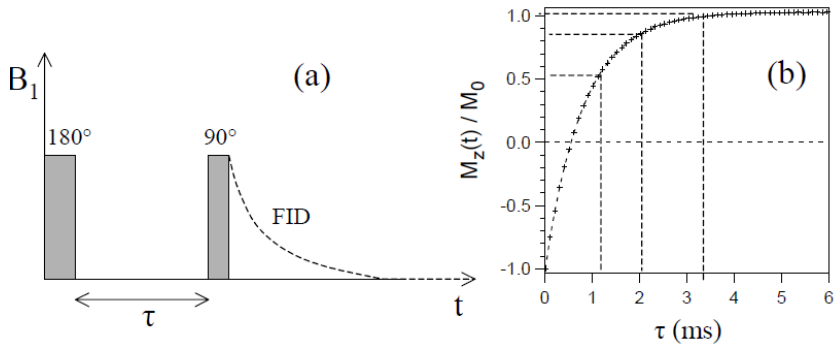

Figure 131. Inversion-recovery illustration [67]

T2 determination

Hahn sequency

In order to determine T2, multiple impulsions are sent. This induces a “re-focusation” like spin echo as shown in *Figure 132*.

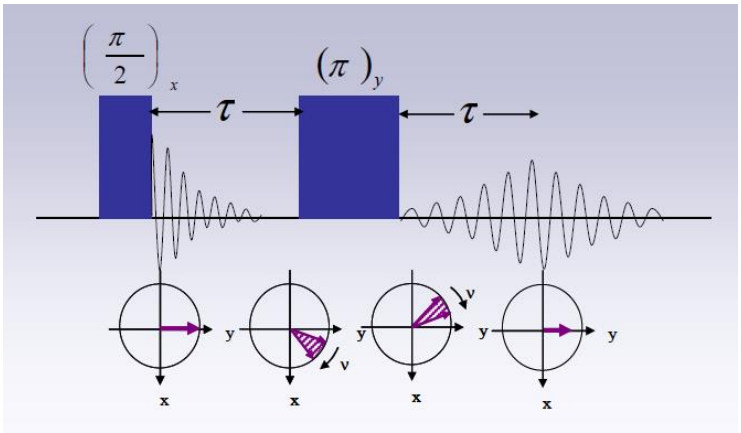

Figure 132. Spin echo illustration. T2 determination illustration (at the top) and magnetization return (at the bottom) [29]

Hahn was the first to suggest a method for overcoming the limitation of the external magnetic field inhomogeneity. He proposed the application of π pulse at time τ – known as the pulse gap, after the initial π/2. The magnetization refocuses at time 2τ along the y'-axis and a spin-echo is created. The amplitude of the echo, at time 2τ, is already attenuated due to true transverse relaxation. Hence, the maximum of the echo amplitude is a function of T2 relaxation time [27] as illustrated in *Figure 133*.

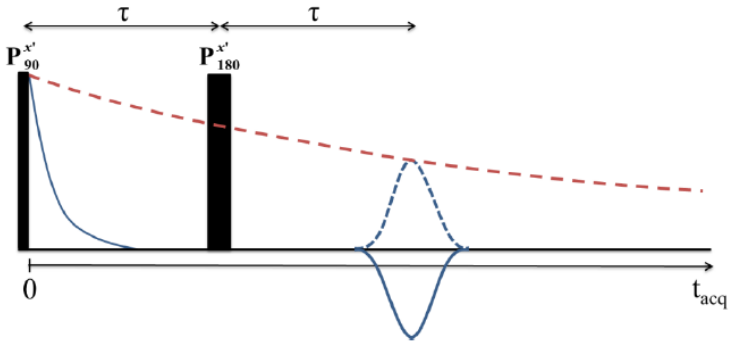

Figure 133. The Hahn spin-echo pulse sequence diagram. The red dash line shows the decay of transverse magnetization.

Usually, T2 time is usually smaller than T1. For pure water T2 is around 3 seconds, for pore water from some milliseconds to couple of milliseconds [30]. The impulsion send M_0 on y axis (transversal), nuclear magnetization changes during period of time (Δ time), but it does not remain constant. After delta time they refocuses and an echo is observable.

CPMG: Carr Purcell and Melboom Gill Pulse Sequence

This method is based on Hanh method but with multiple pulses: contrary to the method described in the last paragraph, multiple impulsions are sent at π angle compared to the π/2 first impulsion. Two impulsions are separated of 2Δ time in order to obtain a spin echo between 2 impulsions as shown in *Figure 134*.

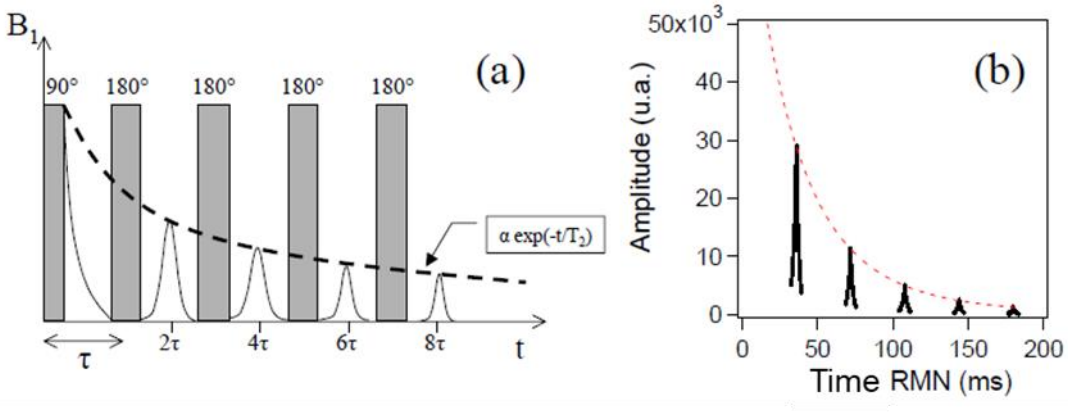

Figure 134. (a) CPMG : decreasing of transversal magnetization Mxy. (b) spin echo example [30]

Molecular mass calculated:

M(Ca)=40 g.mol^{-1}, M(Si)= 28 g.mol^{-1}, M(Al)=27 g.mol^{-1}

M(C_2S)= 228 g.mol^{-1}; M(CSH)= 223.2 g.mol^{-1} ; M(C_2S)=172 g.mol^{-1} ; M(C_3A) = 270 g.mol^{-1} ; M(CH)= 74 g.mol^{-1} ; M(ettringite) = 1310 g.mol^{-1}

Substance	M (g/mol)	ρ (g/cm^3)	ω (cm^3/mol)
C_3S	228.33	3.120	73.18
C_2S	172.25	3.326	51.79
C_3A	270.20	3.060	88.30
C_4AF	485.97	3.730	130.29
$C\bar{S}$	136.14	2.558	53.22
$C\bar{S}H_{0.5}$	145.15	2.733	53.11
$C\bar{S}H_2$	172.18	2.310	74.54
$C\bar{C}$	100.09	2.711	36.92
H	18.02	1.000	18.02
CH	74.10	2.242	33.05
$C_{1.7}SH_{3.2}$	213.09	2.253	94.60
$C_{1.7}SH_{1.2}$	177.05	2.856	62.00

Figure 135. Molecular weight of anhydres and hydrate of Portland cement by Brouwers[123]

Name	Molecular weight [g]	Density [g/cm^3]	H_2O/Ca ratio	Molecular weight [g]	Density [g/cm^3]	H_2O/Ca ratio
	11%RH*1			D-dry		
C-S-H*2	200.5	2.18*3	1.47	184.2	2.70*3	0.94
CH	74.1	2.24	1.00	74.1	2.24	1.00
Calcite*4	100.1	2.30	1.00	100.1	2.30	1.00
AFt	1251.5	1.73	5.33	894.8	2.38	2.00
AFm	622.5	1.99	3.00	543.3	2.40	2.00
Mc	586.5	1.99	3.00	514.4	2.40	2.00
Hc	573.5	1.99	3.12	501.4	2.40	2.13

*1 15%RH(this study) *2 11%RH : $C_{1.7}SH_{2.5}$, D-Dry : $C_{1.7}SH_{1.6}$
*3 Exclusive of Gel Porosity *4 CO_2/Ca ratio

Figure 136. Molecular weight of anhydres and hydrate of Portland cement by Dyson [124]

The density of each hydrate is difficult to evaluate as we can see in the different determination from the literature; density defers depending of the drying conditions…

Component	Density (g/cm^3)	Component	Density (g/cm^3)
C_3S	3.15	$C_{1.7}SH_{1.35}$*2	2.60
C_2S	3.26	CH	2.24
C_3A	3.04	$C_3A \cdot 3C\bar{S} \cdot H_{32}$	1.73
C_4AF	3.77	$3C_3A \cdot C\bar{S} \cdot H_{12}$	1.99
$C\bar{S}H_2$	2.32	$C_4AF \cdot 3C\bar{S} \cdot H_{32}$	1.77
$C_{1.7}SH_4$ *1	2.12	$3C_4AF \cdot C\bar{S} \cdot H_{12}$	2.08

*1 :including physically bound water, *2:excluding physically bound water

Figure 137. Density of anhydrites and hydrate of Portland cement by Maruyama [67]

References

[1] E. Lloret Fritschi, « Smart Dynamic Casting - A digital fabrication method for non-standard concrete structures », ETH Zurich, 2016.

[2] D. Kaplan, « Pompage des bétons », Etudes des recherches des laboratoires des Ponts et Chaussée, Laboratoire central des Ponts et Chaussées, Paris, 2000.

[3] M. Choi, N. Roussel, Y. Kim, et J. Kim, « Lubrication layer properties during concrete pumping », *Cem. Concr. Res.*, vol. 45, p. 69-78, mars 2013, doi: 10.1016/j.cemconres.2012.11.001.

[4] K. T. Fosså, « Slipforming of vertical concrete structures », *Nor. Univ. Sci. Technol. Trondheim Nor.*, nº 1292, p. 301, 2001.

[5] N. Roussel, G. Ovarlez, S. Garrault, et C. Brumaud, « The origins of thixotropy of fresh cement pastes », *Cem. Concr. Res.*, vol. 42, nº 1, p. 148-157, janv. 2012, doi: 10.1016/j.cemconres.2011.09.004.

[6] P. Mounanga, A. Khelidj, A. Loukili, et N. Rafaï, « Autogenous deformations of cement pastes », *Cem. Concr. Res.*, vol. 36, nº 1, p. 123-136, janv. 2006, doi: 10.1016/j.cemconres.2004.10.020.

[7] P. Mounanga, A. Khelidj, A. Loukili, et V. Baroghel-Bouny, « Predicting Ca(OH)2 content and chemical shrinkage of hydrating cement pastes using analytical approach », *Cem. Concr. Res.*, vol. 34, nº 2, p. 255-265, févr. 2004, doi: 10.1016/j.cemconres.2003.07.006.

[8] G. Ovarlez et N. Roussel, « A Physical Model for the Prediction of Lateral Stress Exerted by Self-Compacting Concrete on Formwork », *Mater. Struct.*, vol. 39, nº 2, p. 269-279, août 2007, doi: 10.1617/s11527-005-9052-1.

[9] P. H. Billberg *et al.*, « Field validation of models for predicting lateral form pressure exerted by SCC », *Cem. Concr. Compos.*, vol. 54, p. 70-79, nov. 2014, doi: 10.1016/j.cemconcomp.2014.02.003.

[10] A. Perrot, A. Pierre, S. Vitaloni, et V. Picandet, « Prediction of lateral form pressure exerted by concrete at low casting rates », *Mater. Struct.*, vol. 48, nº 7, p. 2315-2322, juill. 2015, doi: 10.1617/s11527-014-0313-8.

[11] J. E. Wallevik, « Rheological properties of cement paste: Thixotropic behavior and structural breakdown », *Cem. Concr. Res.*, vol. 39, nº 1, p. 14-29, janv. 2009, doi: 10.1016/j.cemconres.2008.10.001.

[12] N. R. Andriamanantsilavo et S. Amziane, « Maturation of fresh cement paste within 1- to 10-m-large formworks », *Cem. Concr. Res.*, vol. 34, nº 11, p. 2141-2152, nov. 2004, doi: 10.1016/j.cemconres.2004.03.027.

[13] S. Amziane, « Setting time determination of cementitious materials based on measurements of the hydraulic pressure variations », *Cem. Concr. Res.*, vol. 36, nº 2, p. 295-304, févr. 2006, doi: 10.1016/j.cemconres.2005.06.013.

[14] A. Radocea, « A Study on the Mechanism of Plastic Shrinkage of Cement-Based Materials », Goteborg, Sweden, 1992.

[15] P.-C. AÏtcin et R. J. Flatt, « Science and technology of concrete admixtures ». Elsevier Ltd., 2016.

[16] P. Barriac, « Rôle des sulfates dans l'hydratation des Portland », 1995.

[17] J.-M. Estoup, « L'eau dans le béton, la juste dose... » Sycodés Information n°63, 2000.

[18] F. Mekkaoui, « Amélioration de la vitesse d'hydratation et de durcissement d'un ciment pouzzolanique par l'utilisation d'accélérateur de prise », p. 141, 2011.

[19] S. Garcia Boivin, « Retrait au jeune âge du béton – Développement d'une méthode expérimentale et contribution à l'analyse physique du retrait endogène ». PhD dissertation, Etudes et Recherches des LPC, OA 37, LCPC Publ, 2001.

[20] G. Chanvillard, « Le matériau béton : connaissances generales ». Entpe Aléas.

[21] « Livre blanc Conductimétrie ». LafargeHolcim internal document, 2008.

[22] « http://culturesciencesphysique.ens-lyon.fr/ressource/Diffraction-rayons-X-techniques-determination-structure.xml ». .
[23] « p://www.hitachi-hightech.com/global/products/science/tech/ana/thermal/descriptions/dta.html ». .
[24] H. Jaffel, « Caractérisation multi-échelles de matériaux poreux en évolution : cas du plâtre », p. 183.
[25] P. Faure et P. Coussot, « Drying of a model soil », *Phys. Rev. E*, vol. 82, nº 3, p. 036303, sept. 2010, doi: 10.1103/PhysRevE.82.036303.
[26] S. Bahafid, S. Ghabezloo, M. Duc, P. Faure, et J. Sulem, « Effect of the hydration temperature on the microstructure of Class G cement: C-S-H composition and density », *Cem. Concr. Res.*, vol. 95, p. 270-281, mai 2017, doi: 10.1016/j.cemconres.2017.02.008.
[27] M. Fourmentin *et al.*, « Porous structure and mechanical strength of cement-lime pastes during setting », *Cem. Concr. Res.*, vol. 77, p. 1-8, nov. 2015, doi: 10.1016/j.cemconres.2015.06.009.
[28] P. F. Faure et S. Rodts, « Proton NMR relaxation as a probe for setting cement pastes », *Magn. Reson. Imaging*, vol. 26, nº 8, p. 1183-1196, oct. 2008, doi: 10.1016/j.mri.2008.01.026.
[29] A. M. Gajewicz, « Characterisation of cement microstructure and pore – water interaction by 1H Nuclear Magnetic Resonance Relaxometry », p. 180.
[30] « https://www.empa.ch/documents/55996/231904/Poster-Application+of+thermogravimetric.pdf/cd759220-84e7-48e1-910e-c131280be061 ». .
[31] A. C. A. Muller, « Characterization of porosity & C-S-H in cement pastes by 1H NMR », p. 208.
[32] A. Perrot, D. Rangeard, et A. Pierre, « Structural built-up of cement-based materials used for 3D-printing extrusion techniques », *Mater. Struct.*, vol. 49, nº 4, p. 1213-1220, avr. 2016, doi: 10.1617/s11527-015-0571-0.
[33] D. Lootens, P. Jousset, L. Martinie, N. Roussel, et R. J. Flatt, « Yield stress during setting of cement pastes from penetration tests », *Cem. Concr. Res.*, vol. 39, nº 5, p. 401-408, mai 2009, doi: 10.1016/j.cemconres.2009.01.012.
[34] T. A. Hammer, « The use of pore water pressure to follow the evolution from fresh to hardened concrete », p. 10, 2006.
[35] T. Craipeau, T. Lecompte, F. Toussaint, et A. Perrot, « Evolution of Concrete/Formwork Interface in Slipforming Process », in *First RILEM International Conference on Concrete and Digital Fabrication – Digital Concrete 2018*, vol. 19, T. Wangler et R. J. Flatt, Éd. Cham: Springer International Publishing, 2019, p. 12-23.
[36] V. Slowik, T. Hübner, M. Schmidt, et B. Villmann, « Simulation of capillary shrinkage cracking in cement-like materials », *Cem. Concr. Compos.*, vol. 31, nº 7, p. 461-469, août 2009, doi: 10.1016/j.cemconcomp.2009.05.004.
[37] F. Caupin et E. Herbert, « Cavitation in water: a review », *Comptes Rendus Phys.*, vol. 7, nº 9-10, p. 1000-1017, nov. 2006, doi: 10.1016/j.crhy.2006.10.015.
[38] Ø. Bjøntegaard, T. A. Hammer, et E. J. Sellevold, « On the measurement of free deformation of early age cement paste and concrete », *Cem. Concr. Compos.*, vol. 26, nº 5, p. 427-435, juill. 2004, doi: 10.1016/S0958-9465(03)00065-9.
[39] A. Alexandridis et N. J. Gardner, « Mechanical behaviour of fresh concrete », *Cem. Concr. Res.*, vol. 11, nº 3, p. 323-339, mai 1981, doi: 10.1016/0008-8846(81)90105-8.
[40] N. Roussel, A. Lemaître, R. J. Flatt, et P. Coussot, « Steady state flow of cement suspensions: A micromechanical state of the art », *Cem. Concr. Res.*, vol. 40, nº 1, p. 77-84, janv. 2010, doi: 10.1016/j.cemconres.2009.08.026.
[41] R. J. Flatt et P. Bowen, « Yield Stress of Multimodal Powder Suspensions: An Extension of the Yodel (Yield Stress model) », *J. Am. Ceram. Soc.*, vol. 90, nº 4, p. 1038-1044, avr. 2007, doi: 10.1111/j.1551-2916.2007.01595.x.
[42] J. Yammine, M. Chaouche, M. Guerinet, M. Moranville, et N. Roussel, « From ordinary rhelogy concrete to self compacting concrete: A transition between frictional and hydrodynamic

interactions », *Cem. Concr. Res.*, vol. 38, nº 7, p. 890-896, juill. 2008, doi: 10.1016/j.cemconres.2008.03.011.
[43] H. Le Chatelier, « Sur les changements de volume qui accompagnent le durcissement des ciments ». Bull. Société de l'Encouragement pour l'Industrie Nationale, 1900.
[44] S. Mantellato, M. Palacios, et R. J. Flatt, « Relating early hydration, specific surface and flow loss of cement pastes », *Mater. Struct.*, vol. 52, nº 1, p. 5, févr. 2019, doi: 10.1617/s11527-018-1304-y.
[45] F. H. Wittmann, « On the action of capillary pressure in fresh concrete », *Cem. Concr. Res.*, vol. 6, nº 1, p. 49-56, janv. 1976, doi: 10.1016/0008-8846(76)90050-8.
[46] S. Ghourchian, M. Wyrzykowski, et P. Lura, « A poromechanics model for plastic shrinkage of fresh cementitious materials », *Cem. Concr. Res.*, vol. 109, p. 120-132, juill. 2018, doi: 10.1016/j.cemconres.2018.04.013.
[47] P. Acker, *Comportement mécanique du béton: apports de l'approche physico-chimique*. Rapport de recherche LPC, 1988.
[48] V. Baroghel-Bouny, P. Mounanga, A. Khelidj, A. Loukili, et N. Rafai, « Autogenous deformations of cement pastes: Part II. W/C effects, micro-macro correlations, and threshold values », p. 15.
[49] N. Massoussi, E. Keita, et N. Roussel, « The heterogeneous nature of bleeding in cement pastes », *Cem. Concr. Res.*, vol. 95, p. 108-116, mai 2017, doi: 10.1016/j.cemconres.2017.02.012.
[50] L. Josserand, O. Coussy, et F. de Larrard, « Bleeding of concrete as an ageing consolidation process », *Cem. Concr. Res.*, vol. 36, nº 9, p. 1603-1608, sept. 2006, doi: 10.1016/j.cemconres.2004.10.006.
[51] M. Bouasker, P. Mounanga, et A. Khelidj, « Déformation endogène des pâtes de ciment au très jeune âge : Analyse critique et développement métrologique », Bordeaux, 2007.
[52] V. Slowik, M. Schmidt, et R. Fritzsch, « Capillary pressure in fresh cement-based materials and identification of the air entry value », *Cem. Concr. Compos.*, vol. 30, nº 7, p. 557-565, août 2008, doi: 10.1016/j.cemconcomp.2008.03.002.
[53] S. D. N. Lourenço, D. Gallipoli, D. G. Toll, C. E. Augarde, F. D. Evans, et G. M. Medero, « Calibrations of a high-suction tensiometer », *Géotechnique*, vol. 58, nº 8, p. 659-668, oct. 2008, doi: 10.1680/geot.2008.58.8.659.
[54] D. G. Toll, S. D. N. Lourenço, et J. Mendes, « Advances in suction measurements using high suction tensiometers », p. 40.
[55] O. M. Jensen et P. F. Hansen, « Water-entrained cement-based materials I. Principles and theoretical background$ », *Cem. Concr. Res.*, p. 8, 2001.
[56] A. Tarantino, « Unsaturated soils: compacted versus reconstituted states », 5th International Conference on Unsaturated Soil - Barcelona, Spain, p. 113-136, 2010.
[57] P. K. Mehta et J. M. Monteiro, « Concrete: Structure, Properties and Materials ». Prentice Hall, Inc, 2nd Edition, 1993.
[58] M. Geiker, « Measurement of chemical shrinkage and a systematic evaluation of hydration curves by means of the dispersion model », PhD thesis, Technical University of Denmark, 1983.
[59] T. C. Powers, « Capillary continuity or discontinuity in cement pastes », p. 38-48, 1959.
[60] G. J. Verbeck et R. H. Helmuth, « Structures and physical properties of hardened cement paste », Tokyo, p. 1-11, 1968.
[61] T. C. Powers et T. L. Brownyard, « Studies of the Physical Properties of Hardened Portland Cement Paste Part 9. General Summary of Findings on the Properties of Hardened portland Cement Paste », p. 971-992, 1947.
[62] E. Steiner, « Relaxométrie du proton pour l'étude de fluides à l'intérieur de milieux poreux ». Université de Lorraine, 2011.
[63] « https://www.solids-solutions.com/fr/rd/porosite-et-surface-specifique/analyse-de-la-porosite-avec-porosimetrie-par-intrusion-de-mercure/ ». .

[64] D. L. Parkhurst et C. A. J. Appelo, « Description of Input and Examples for PHREEQC Version 3—A Computer Program for Speciation, Batch-Reaction, One-Dimensional Transport, and Inverse Geochemical Calculations », Techniques and Methods, 2013.
[65] K. L. Scrivener, « The development of microstructure during the hydration of Portland cement », p. 231.
[66] A. Radocea, « A model of plastic shrinkage », *Mag. Concr. Res.*, vol. 46, nº 167, p. 125-132, juin 1994, doi: 10.1680/macr.1994.46.167.125.
[67] I. Maruyama, « Numerical Modelling of Portland Cement Hydration Based on Particle Kinetic Model and Multi-comporent Concept ». 12th International Congress on the Chemistry of Cement, 2007.
[68] J. P. Ndobo Epoy, *Livre blanc de calorimétrie*. internal LafargeHolcim document, 2007.
[69] Ph. Blanc, X. Bourbon, A. Lassin, et E. C. Gaucher, « Chemical model for cement-based materials: Thermodynamic data assessment for phases other than C–S–H », *Cem. Concr. Res.*, vol. 40, nº 9, p. 1360-1374, sept. 2010, doi: 10.1016/j.cemconres.2010.04.003.
[70] H. Justnes, A. Van Gemert, F. Verboven, et E. J. Sellevold, « Total and external chemical shrinkage of low W/C ratio cement pastes », p. 121– 126, 1996.
[71] Erika E. Holt, « Early age autogenous shrinkage ». 2001.
[72] L. Barcelo, « Influence des caractéristiques des ciments sur la structuration et le comportement dimensionnel des matériaux cimentaires », p. 245.
[73] M. Bouasker, « Étude numérique et expérimentale du retrait endogène au très jeune âge des pâtes de ciment avec et sans inclusions », PhD thesis, Université de Nantes, 2007.
[74] G. Sant, P. Lura, et J. Weiss, « Measurement of Volume Change in Cementitious Materials at Early Ages: Review of Testing Protocols and Interpretation of Results », *Transp. Res. Rec. J. Transp. Res. Board*, vol. 1979, nº 1, p. 21-29, janv. 2006, doi: 10.1177/0361198106197900104.
[75] L. Stefan, « Étude expérimentale et modélisation de l'évolution des propriétés mécaniques au jeune âge dans les matériaux cimentaires », p. 303.
[76] D. Rangeard, A. Perrot, V. Picandet, Y. Mélinge, et P. Estellé, « Determination of the consolidation coefficient of low compressibility materials: application to fresh cement-based materials », *Mater. Struct.*, vol. 48, nº 5, p. 1475-1483, mai 2015, doi: 10.1617/s11527-014-0247-1.
[77] A. Perrot et D. Rangeard, « Effects of mix design parameters on consolidation behaviour of fresh cement-based materials », *Mater. Struct.*, vol. 50, nº 2, p. 117, avr. 2017, doi: 10.1617/s11527-016-0988-0.
[78] K. Terzaghi et R. B. Peck, « Soil Mechanics in Engineering Practice », p. 26.
[79] A. Loukili, D. Chopin, A. Khelidj, et J.-Y. Le Touzo, « A new approach to determine autogenous shrinkage of mortar at an early age considering temperature history », *Cem. Concr. Res.*, vol. 30, nº 6, p. 915-922, juin 2000, doi: 10.1016/S0008-8846(00)00241-6.
[80] T. Zhang, P. Gao, R. Luo, Y. Guo, J. Wei, et Q. Yu, « Measurement of chemical shrinkage of cement paste: Comparison study of ASTM C 1608 and an improved method », *Constr. Build. Mater.*, vol. 48, p. 662-669, nov. 2013, doi: 10.1016/j.conbuildmat.2013.07.086.
[81] W. Yodsudjai et K. Wang, « Chemical shrinkage behavior of pastes made with different types of cements », *Constr. Build. Mater.*, vol. 40, p. 854-862, mars 2013, doi: 10.1016/j.conbuildmat.2012.11.053.
[82] M. Berthelot, « Sur quelques phénomènes de dilatation forcée des liquides », p. 232-237, 1850.
[83] T. Lecompte, A. Perrot, V. Picandet, H. Bellegou, et S. Amziane, « Cement-based mixes: Shearing properties and pore pressure », *Cem. Concr. Res.*, vol. 42, nº 1, p. 139-147, janv. 2012, doi: 10.1016/j.cemconres.2011.09.007.
[84] G. H. Tattersall et P. F. G. Banfill, *The rheology of fresh concrete*, Pitman advanced publishing program. 1983.
[85] J. F. Steffe, « Food process engineering », p. 428.

[86] A. Perrot, D. Rangeard, V. N. Nerella, et V. Mechtcherine, « Extrusion of cement-based materials - an overview », *RILEM Tech. Lett.*, vol. 3, p. 91-97, févr. 2019, doi: 10.21809/rilemtechlett.2018.75.
[87] A. Perrot, Y. Mélinge, D. Rangeard, F. Micaelli, P. Estellé, et C. Lanos, « Use of ram extruder as a combined rheo-tribometer to study the behaviour of high yield stress fluids at low strain rate », *Rheol. Acta*, vol. 51, nº 8, p. 743-754, août 2012, doi: 10.1007/s00397-012-0638-6.
[88] F. Mahaut, X. Chateau, P. Coussot, et G. Ovarlez, « Yield stress and elastic modulus of suspensions of noncolloidal particles in yield stress fluids », *J. Rheol.*, vol. 52, nº 1, p. 287-313, janv. 2008, doi: 10.1122/1.2798234.
[89] N. Roussel, « Rheological requirements for printable concretes », *Cem. Concr. Res.*, vol. 112, p. 76-85, oct. 2018, doi: 10.1016/j.cemconres.2018.04.005.
[90] A. Perrot, D. Rangeard, et E. Courteille, « 3D printing of earth-based materials: Processing aspects », *Constr. Build. Mater.*, vol. 172, p. 670-676, mai 2018, doi: 10.1016/j.conbuildmat.2018.04.017.
[91] N. Roussel, H. Bessaies-Bey, S. Kawashima, D. Marchon, K. Vasilic, et R. Wolfs, « Recent advances on yield stress and elasticity of fresh cement-based materials », *Cem. Concr. Res.*, vol. 124, p. 105798, oct. 2019, doi: 10.1016/j.cemconres.2019.105798.
[92] S. Timoshenko et S. Woinowsky Krieger, « Theory of plates and shells ». the McGraw-Hill Book Company, Inc, 1959.
[93] R. W. Clough et J. Penzien, « Dynamics of structures ». Computers & Structures, Inc, 2003.
[94] J. Hot, « Influence des polymères de type superplastifiants et agents entraineurs d'air sur la viscosité macroscopique des matériaux cimentaires ». 2014.
[95] B. Feneuil, N. Roussel, et O. Pitois, « Yield stress of aerated cement paste », *Cem. Concr. Res.*, vol. 127, p. 105922, janv. 2020, doi: 10.1016/j.cemconres.2019.105922.
[96] B. Feneuil, O. Pitois, et N. Roussel, « Effect of surfactants on the yield stress of cement paste », *Cem. Concr. Res.*, vol. 100, p. 32-39, oct. 2017, doi: 10.1016/j.cemconres.2017.04.015.
[97] M. Kogan, L. Ducloué, J. Goyon, X. Chateau, O. Pitois, et G. Ovarlez, « Mixtures of foam and paste: suspensions of bubbles in yield stress fluids », *Rheol. Acta*, vol. 52, nº 3, p. 237-253, mars 2013, doi: 10.1007/s00397-013-0677-7.
[98] J. M. Dixon, M. Taniguchi, et J. S. Lindsey, « PhotochemCAD 2: A Refined Program with Accompanying Spectral Databases for Photochemical Calculations{ », p. 2.
[99] H. Du, R.-C. A. Fuh, J. Li, L. A. Corkan, et J. S. Lindsey, « PhotochemCAD: A Computer-Aided Design and Research Tool in Photochemistry », *Photochem. Photobiol.*, vol. 68, nº 2, p. 141-142, août 1998, doi: 10.1111/j.1751-1097.1998.tb02480.x.
[100] D. Rangeard, A. Perrot, et M. Rodomond, « Effect of Limestone Powder Addition Quality on SCC Rheology », in *Rheology and Processing of Construction Materials*, Springer, 2019, p. 500-507.
[101] L. Ducloué, O. Pitois, J. Goyon, X. Chateau, et G. Ovarlez, « Rheological behaviour of suspensions of bubbles in yield stress fluids », *ArXiv14056144 Cond-Mat Physicsphysics*, mai 2014.
[102] F. Boyer, É. Guazzelli, et O. Pouliquen, « Unifying Suspension and Granular Rheology », *Phys. Rev. Lett.*, vol. 107, nº 18, p. 188301, oct. 2011, doi: 10.1103/PhysRevLett.107.188301.
[103] R. J. M. Wolfs, F. P. Bos, et T. A. M. Salet, « Triaxial compression testing on early age concrete for numerical analysis of 3D concrete printing », *Cem. Concr. Compos.*, vol. 104, p. 103344, nov. 2019, doi: 10.1016/j.cemconcomp.2019.103344.
[104] J. J. Assaad, J. Harb, et Y. Maalouf, « Measurement of yield stress of cement pastes using the direct shear test », *J. Non-Newton. Fluid Mech.*, vol. 214, p. 18-27, déc. 2014, doi: 10.1016/j.jnnfm.2014.10.009.

[105] H. Khelifi, A. Perrot, T. Lecompte, D. Rangeard, et G. Ausias, « Prediction of extrusion load and liquid phase filtration during ram extrusion of high solid volume fraction pastes », *Powder Technol.*, vol. 249, p. 258-268, 2013, doi: http://dx.doi.org/10.1016/j.powtec.2013.08.023.
[106] C. S. Campbell, « Granular material flows – An overview », *Powder Technol.*, vol. 162, nº 3, p. 208-229, mars 2006, doi: 10.1016/j.powtec.2005.12.008.
[107] T. A. Hammer, *Deformations, strain capacity and cracking of concrete in plastic and early hardening phases*. Trondheim: Norwegian Univ. of Science and Technology, Fac. of Engineering Science and Technology, Dep. of Structural Engineering, 2007.
[108] Y. Mélinge, V. H. Hoang, D. Rangeard, A. Perrot, et C. Lanos, « Study of tribological behaviour of fresh mortar against a rigid plane wall », p. 419-429, 2013.
[109] T. T. Ngo, E. H. Kadri, R. Bennacer, et F. Cussigh, « Use of tribometer to estimate interface friction and concrete boundary layer composition during the fluid concrete pumping », *Constr. Build. Mater.*, p. 9, 2010.
[110] C. Djelal, Y. Vanhove, et A. Magnin, « Tribological behaviour of self compacting concrete », *Cem. Concr. Res.*, vol. 34, nº 5, p. 821-828, mai 2004, doi: 10.1016/j.cemconres.2003.09.013.
[111] G. Ovarlez et N. Roussel, « A physical model for the prediction of lateral stress exerted by self-compacting concrete on formwork », p. 9.
[112] I. M. Hutchings, « Leonardo da Vinci′s studies of friction », *Wear*, vol. 360-361, p. 51-66, août 2016, doi: 10.1016/j.wear.2016.04.019.
[113] J. Best et R. Lane, « Testing for optimum pumpability of concrete », p. p9-17, 1960.
[114] V. Mechtcherine, V. N. Nerella, et K. Kasten, « Testing pumpability of concrete using Sliding Pipe Rheometer », *Constr. Build. Mater.*, vol. 53, p. 312-323, févr. 2014, doi: 10.1016/j.conbuildmat.2013.11.037.
[115] M. Morinaga, « Pumpability of concrete and pumping pressure in pipelines », Leeds, p. 1-39, 1973.
[116] F. Chapdelaine, « Étude fondamentale et pratique sur le pompage du béton », p. 154.
[117] T.-T. Ngo, F. Cussigh, E.-H. Kadri, R. Bennacer, et R. Duval, « Influence de la formulation des bétons fluides sur leur pompabilité », p. 9, 2007.
[118] M. Horgnies, *Tribologie des bétons à ultra-haute performance - Propriétés de surface et revêtement de protection*. 2012.
[119] M. Martin, « Etude de la texture de la surface coffrée des parements verticaux en béton », p. 232.
[120] S. Amziane, « Contribution à l'étude des matériaux cimentaires à l'état frais », p. 110.
[121] A. Perrot, « Matériaux Cimentaires : De la Caractérisation à la Mise en OEuvre », p. 127.
[122] L. K. Mettler, F. K. Wittel, R. J. Flatt, et H. J. Herrmann, « Evolution of Strength and Failure of SCC during Early Hydration », *ArXiv160902293 Cond-Mat*, sept. 2016.
[123] H. J. H. Brouwers, « The work of Powers and Brownyard revisited: Part 1 », *Cem. Concr. Res.*, vol. 34, nº 9, p. 1697-1716, sept. 2004, doi: 10.1016/j.cemconres.2004.05.031.
[124] H. Dyson, « Early Hydration in Binary and Ternary Blended Cements », Thèse, UK.